

INFORMATION TO USERS

While the most advanced technology has been used to photograph and reproduce this manuscript, the quality of the reproduction is heavily dependent upon the quality of the material submitted. For example:

- Manuscript pages may have indistinct print. In such cases, the best available copy has been filmed.
- Manuscripts may not always be complete. In such cases, a note will indicate that it is not possible to obtain missing pages.
- Copyrighted material may have been removed from the manuscript. In such cases, a note will indicate the deletion.

Oversize materials (e.g., maps, drawings, and charts) are photographed by sectioning the original, beginning at the upper left-hand corner and continuing from left to right in equal sections with small overlaps. Each oversize page is also filmed as one exposure and is available, for an additional charge, as a standard 35mm slide or as a 17"x 23" black and white photographic print.

Most photographs reproduce acceptably on positive microfilm or microfiche but lack the clarity on xerographic copies made from the microfilm. For an additional charge, 35mm slides of 6"x 9" black and white photographic prints are available for any photographs or illustrations that cannot be reproduced satisfactorily by xerography.

8704790

Steijn, Kirk William

COUPLING AND PROPAGATION OF SURFACE PLASMONS IN THE FAR
INFRARED

The University of Arizona

Ph.D. 1986

University
Microfilms
International 300 N. Zeeb Road, Ann Arbor, MI 48106

PLEASE NOTE:

In all cases this material has been filmed in the best possible way from the available copy. Problems encountered with this document have been identified here with a check mark .

1. Glossy photographs or pages _____
2. Colored illustrations, paper or print _____
3. Photographs with dark background _____
4. Illustrations are poor copy _____
5. Pages with black marks, not original copy _____
6. Print shows through as there is text on both sides of page _____
7. Indistinct, broken or small print on several pages
8. Print exceeds margin requirements _____
9. Tightly bound copy with print lost in spine _____
10. Computer printout pages with indistinct print _____
11. Page(s) _____ lacking when material received, and not available from school or author.
12. Page(s) _____ seem to be missing in numbering only as text follows.
13. Two pages numbered _____. Text follows.
14. Curling and wrinkled pages _____
15. Dissertation contains pages with print at a slant, filmed as received _____
16. Other _____

University
Microfilms
International

**COUPLING AND PROPAGATION OF SURFACE PLASMONS
IN THE FAR INFRARED**

by

Kirk William Steijn

**A Dissertation Submitted to the Faculty of the
COMMITTEE ON OPTICAL SCIENCES (GRADUATE)**

**In Partial Fulfillment of the Requirements
For the Degree of**

DOCTOR OF PHILOSOPHY

In the Graduate College

THE UNIVERSITY OF ARIZONA

1 9 8 6

THE UNIVERSITY OF ARIZONA
GRADUATE COLLEGE

As members of the Final Examination Committee, we certify that we have read
the dissertation prepared by Kirk William Steijn

entitled Coupling and Propagation of Surface Plasmons

in the Far Infrared

and recommend that it be accepted as fulfilling the dissertation requirement
for the Degree of Doctor of Philosophy.

J. J. Burke

9/12/86
Date

H. Steijn

9/12/86
Date

H. O. Scaplen H. O. Scaplen

9/12/86
Date

Date

Date

Final approval and acceptance of this dissertation is contingent upon the
candidate's submission of the final copy of the dissertation to the Graduate
College.

I hereby certify that I have read this dissertation prepared under my
direction and recommend that it be accepted as fulfilling the dissertation
requirement.

M. Steijn
Dissertation Director

Oct 31, 1986
Date

STATEMENT BY AUTHOR

This dissertation has been submitted in partial fulfillment of requirements for an advanced degree at The University of Arizona and is deposited in the University Library to be made available to borrowers under rules of the Library.

Brief quotations from this dissertation are allowable without special permission, provided that accurate acknowledgement of source is made. Requests for permission for extended quotation from or reproduction of this manuscript in whole or in part may be granted by the head of the major department or by the Dean of the Graduate College when in his or her judgment the proposed use of the material is in the interests of scholarship. In all other instances, however, permission must be obtained from the author.

SIGNED: Kirk W. Steyer

Dedicated to my parents,

Roelof Pieter Steijn

and

Evelyn Beasley Steijn

ACKNOWLEDGEMENTS

The candidate would like to thank the many people who made this work possible. First let me thank my advisor, Prof. George Stegeman. Aside from the responsibilities inherent in that role, his timely words of encouragement instilled fresh energy into my efforts, often at critical times. His achievements are an inspiration to us all. A great debt is owed as well to Dr. Robert J. Seymour of GTE Laboratories, my local advisor at GTE Laboratories. His experiments laid the groundwork for my project, and he provided many important ideas, comments and suggestions. I especially appreciate his careful review of the penultimate draft of this dissertation. Furthermore, I wish to thank Bob and GTE Laboratories for providing the laboratory, the equipment, and the funding for the project.

At GTE, many people made major contributions to the work. I wish to thank Marvin Tabasky, who was just great all the time. No favor was too big, and in the end he helped provide the means of fabricating usable waveguides. Thanks also to Paul Poppert for making his resources available to me as well. Without Marvin, Paul and their resources, the results would not have come within two orders of magnitude from what they are. Victor Cataldo skillfully grew the silicon overlayers, the cornerstone of the experiments. Thanks also to Florence White, who performed much of the wafer processing, and always with a very big smile, and to Maggie Ames, who made many an emergency Dektak measurement. Special thanks to my good friend Mike Newkirk for software, and for invaluable assistance (laser cover jock). Also, he was always there when I needed coffee. I must also thank Margaret Stern, who gave me free access to her Dektak.

My friends and colleagues at GTE have my sincere thanks for assistance, input, and fascinating lunchtime technical discussions. Special thanks to John Hryniewicz, who "booted" me up when I first arrived. Thanks also to Dr. Y.J. (Ray) Chen and Steve Brown. I must also acknowledge that Dr. Wayne Sharfin has the world's nastiest cockroach stories.

At the University of Arizona, I wish to thank my friends and colleagues. My good friend Dr. Ray Zaroni provided curve-fitting routines, and advice, some of which was really good. I am indebted to Prof. Jim Burke for carefully reviewing the dissertation. Thanks also to Maggie Whitney and Mary McGoldrick, for being kind and patient. I owe thanks to Brenda Striegel for timely information (i.e. deadlines), and Lisa and Peter Dubois for a place to stay.

Most of all, I wish to thank my family. To my parents (to whom this dissertation is dedicated), who started this work back in the late fifties, and to my mother- and father-in-law, who provided a desk, good food, and Susan. And finally, I wish to thank my beloved wife Susan, who originated my interest in far-infrared surface plasmons.

TABLE OF CONTENTS

	Page
LIST OF ILLUSTRATIONS	viii
LIST OF TABLES	x
ABSTRACT	xi
1. INTRODUCTION	1
2. THEORY	8
Maxwell's Equations	8
Guided Waves	10
Surface Plasmon Equations	11
Properties of Metals (The Drude Model)	14
$\omega \rightarrow 0$: The Far Infrared	19
Overcoated Surface Plasmon Mode	20
3. EXPERIMENTAL SETUP	27
4. SAMPLE FABRICATION	36
5. ATTENUATION MEASUREMENTS	45
Experimental Method	46
Results & Discussion	47
6. COUPLING STUDY	53
Coupled Mode Theory	55
In-coupling	56
Out-coupling	60
Grating Theory	62
Upper Corrugation	64
Lower Corrugation	74
Experimental Method	78
In-coupling Measurements	78
Out-coupling Measurements	82
Results	87
Discussion	91

TABLE OF CONTENTS--Continued

	page
Measurement of β_R in Gratings	95
Experimental Method	95
Results	97
Discussion	99
7. CONCLUSION	104
REFERENCES	110

LIST OF ILLUSTRATIONS

Figure	Page
2.1. The Geometry for the Surface Plasmon	13
2.2. The Frequency Dispersion of a Surface Plasmon	18
2.3. The Geometry of the Overcoated Surface Plasmon Mode	22
2.4. The Penetration Depth of the Surface Plasmon Fields into the Upper Medium as a Function of Overlayer Thickness	24
2.5. The Perturbation of β_R by the Overcoating	25
2.6. The Attenuation of the Mode as a Function of Coating Thickness	26
3.1. Experimental Setup	30
4.1. Top View of Sample	39
4.2. Electron Micrographs of the Grating Cross-Section	40
4.3. Sample Cross-Section	43
5.1. Throughput Measurements Plotted on a Semi-Log Scale against Waveguide Length	48
5.2. Measured Absorption Coefficient of the Overcoated Surface Plasmon Mode Plotted against the Overcoat Thickness	49
6.1. Guided-Wave Field Amplitude in Coupling Region	59
6.2. The 0-Order and -1-Order Reflection from and Input Grating as a Function of Incident Angle	83
6.3. A Diagram of the Measurement of Γ at the Output Detector, With an Example of Digitized Data at Bottom	86
6.4. Data and Theory (Solid Line) for Measurements of L_c^{-1} versus Overlayer Thickness	88
6.5. Attenuation in Grating	89
6.6. The Measured Transmission of the Gratings	90

LIST OF ILLUSTRATIONS—Continued

Figure	Page
6.7. A Repeat of Figure 6.5, With the Addition of Two Theoretical Curves	96
6.8. Results of Measurements of β_R , versus Overlayer Thickness	98
6.9. Results of Fitting the Measurements of β_R by Varying the Refractive Index of the Overlayer	100

LIST OF TABLES

Table	Page
4.1. Statistics for Silicon Overlayer Thickness	44

ABSTRACT

This work describes a study of the propagation properties of a modified surface plasmon mode, and of the coupling properties of that mode using a grating coupler. The surface plasmon, a polariton involving coupling of electromagnetic waves to the plasma oscillations of a metal, is modified by the application of a dielectric overlayer to the interface between the metal and air. In the far infrared region of the electromagnetic spectrum, the overlayer causes dramatic changes in several properties of the mode, which can be verified by measuring the propagation length of the mode. Measurements at a wavelength of $118.8 \mu\text{m}$ of the propagation length as a function of the thickness of a polycrystalline silicon overlayer on silver showed that the mode has the expected properties. They also indicated that the Drude model of the dielectric function of the silver is valid at $118.8 \mu\text{m}$, even when using established Drude parameters, which are based on measurements in the visible and near infrared region of the electromagnetic spectrum. The coupling study measured the fundamental coupling parameters, also at a wavelength of $118.8 \mu\text{m}$, for coupling via a grating between free-space waves and the surface plasmon, and measured the effect of the overlayer on these parameters. Efficient coupling was achieved, but a theoretical treatment of the coupling system proved to be beyond the scope of first-order grating-coupler theory. This was true despite the fact that the grating amplitude was a small fraction of the wavelength, a common criterion for the application of such a theory. Several possible reasons for the breakdown of the theory were considered, but definite answers require additional experiments. The most prominent possibilities are the shape factor, and the depth of the grating

compared to the penetration depth of the fields into the metal. Though not all the data is completely explained, the studies herein demonstrate that the overlayer eliminates many of the deficiencies which limit the generation and control of far-infrared surface plasmons.

CHAPTER 1

INTRODUCTION

In the near-millimeter spectral region, little work has been done in the investigation of waveguide modes and their properties. Processing and manipulation of electromagnetic radiation in this region is desirable because of atmospheric windows (Johnston and Burch, 1967), yet it remains largely unexploited because of the scarcity of dielectrics with sufficiently low absorption coefficients. Surface plasmon polaritons guided by metal surfaces offer a possible approach to far-infrared communications because of their very long propagation distances (McMullen, 1975; Koteles and McNeill, 1981). However, metals themselves are extremely lossy, and the propagation distances are long only because nearly all of the mode's energy is contained in the air above the metal. This fact is due to the high dielectric constant of the metal, which also causes the surface plasmon to be highly delocalized from, and poorly bound to the metal surface. These last two effects are detrimental to attempts to manipulate the radiation, and in concert they severely compromise the advantages of the long propagation length. In this dissertation, we investigate the properties of surface plasmons, at a wavelength of $118.8 \mu\text{m}$, that have been modified by the application of a dielectric overlayer to the metal surface. The presence of the overlayer results in a substantial improvement in the characteristics of mode.

This dissertation is organized as follows: The relevant electromagnetic theory for the surface plasmon is presented in Chapter 2. Included is a treatment of the

optical properties of metals known as the Drude model, required because the metal is the primary determinant of the surface plasmon properties (the sole determinant in the case of a bare metal surface). The theory that describes the overcoated mode is given as well. Chapter 3 is a detailed discussion of the equipment used for the experiments. Chapter 4 concerns the details of the fabrication of the samples, which were silicon wafers deposited with optically thick silver films and overcoated with silicon. Gratings were etched into the substrate to serve as couplers. The subject of the next two chapters is the experiments that were performed: Chapter 5 discusses measurements of the propagation distance of the overcoated mode. The behavior of the propagation distance with increasing coating thickness is a key prediction of the overcoated mode equations. A detailed study of the coupling process is discussed in Chapter 6, in which the fundamental properties of the grating couplers were measured, again as a function of the overlayer thickness. The coupling theory which is applicable is given in the theory section of that chapter. Finally, the last chapter concludes the dissertation, with a review of results and a discussion of future work.

The "delocalization" of the surface plasmon is described by the exponential decay of the fields away from the interface. The distance is properly expressed as the point where the field amplitudes have dropped to e^{-1} of their value at the surface, and is often expressed in wavelengths. For a far-infrared surface plasmon at the surface of a noble metal, the characteristic penetration depth into the air is several hundred wavelengths. This situation is analogous to an optical waveguide operating very near cutoff, and is associated with a weakly bound wave.

The cause of poor binding of the mode to the surface requires a more detailed explanation of the properties of the surface plasmon, which is provided in

Chapter 2. However, the effects of poor binding are that the mode will scatter into an unbound (radiative) electromagnetic wave even on a surface that appears macroscopically smooth. Since this may be viewed as a loss mechanism, the actual propagation distance of the mode is limited by this phenomenon. A more troublesome manifestation of the same property occurs when the surface plasmon is generated via coupling with a free-propagating beam. Transverse coupling methods (attenuated total reflection or "ATR") rely on matching the parallel propagation vector of the incident beam with the wavevector (β) of the guided wave. This requires increasing the k-vector of the incident beam to match that of the guided wave. However, the surface plasmon in the far-infrared has a β which is less than one part in 10^5 larger than k_0 , owing again to the high dielectric constant of the metal. This difference is too small to assure sole excitation of the surface plasmon. As a consequence, a bulk wave which travels parallel to the surface is co-generated with the surface plasma wave. Because of the frequency, k-vector, and spatial overlap of the two beams, it is extremely difficult to experimentally remove this bulk "surface skimming" mode, and results attributed to the surface plasmon may in fact be characteristics of the bulk wave (Koteles and MacNeill, 1981). Finally, the poor field confinement prevents efficient coupling to the surface plasmon. The most successful coupling method to date was achieved with a grating, with a quoted efficiency of 5% (Seymour, Krupczak Jr. and Stegeman, 1984).

The properties of the far-infrared surface plasmon change considerably if a thick-film dielectric overlayer is applied to the metal surface. It is well known that the lowest order TM mode of a dielectric waveguide with one metal boundary reduces to a surface plasmon as the dielectric thickness approaches zero (Otto and

Sohler, 1971; Polky and Mitchell, 1974; Schlesinger and Sievers, 1980). The overcoated mode utilized in our experiments is the same mode, in the film thickness region ($t \ll \lambda/2n_f$) where no other waveguide modes are supported. The changes in the properties are a consequence of the shift in β induced by the dielectric film.

Most of the initial experiments on the overcoated mode in the far infrared were concerned with thin film overlayers such as an oxide layer (Bryan, Begley, Bhasin, Alexander, Bell and Gerson, 1976; Bhasin, Bryan, Alexander and Bell, 1976; Zhizhin, Moskaleva, Shomina and Yakovlev, 1976). The theory developed for these cases focused on the frequency dispersion of the surface plasmon, and thickness-dependent parameters were evaluated in the small-thickness limit (Ward, Bell, Alexander, Kovener and Tyler, 1974; Ward, Bhasin, Bell, Alexander and Tyler, 1975; Bell, Alexander, Ward and Tyler, 1975). In measurements involving thick films, disagreement with theory was interpreted as arising from surface roughness (Schlesinger, Webb and Sievers, 1981). The comparison with theory was improved with an exact solution of the overcoated mode (Stegeman and Seymour, 1982). With this solution, which rigorously satisfies the electromagnetic boundary conditions at both film interfaces, it was recognized that the induced perturbation could provide a more useful surface plasmon mode (Seymour and Stegeman, 1983).

The exact formulation predicts that the presence of a high-dielectric overcoating of only a few percent of the wavelength can perturb β sufficiently to reduce the penetration depth into the air by two orders of magnitude. The short penetration distance into the air should vastly improve the efficiency of ATR coupling methods, as the field would be well-localized to, and greatly enhanced at, the metal surface. This field enhancement suggests using a grating coupler

(Seymour, Koteles and Stegeman, 1982), and efficient coupling has been demonstrated with such a technique using the overcoated mode (Seymour, Krupczak Jr. and Stegeman, 1984). Furthermore because of the perturbation of β away from the light-line, the mode will not easily scatter into a bulk wave. The surface-skimming mode can also be eliminated as a result of this perturbation.

The cost of these improvements is a substantial reduction in the propagation distance of the mode, due to the increased percentage of energy carried by the lossy metal. Therefore, in order to reap the benefits of the overcoated mode, it is necessary to determine if there can be a satisfactory trade-off between the propagation distance and field localization. The first experiment discussed in this dissertation (Chapter 5) was designed to provide definitive measurements to answer this question, and to illuminate the features of the overcoated mode. In the process, the Drude model of the metal dielectric constant was examined with regard to its applicability at the low frequencies of these measurements. The mode was found to behave according to the field equations that describe it, and good agreement was obtained using the Drude model.

The study of the grating couplers (Chapter 6) was performed in order to augment the measurements of Chapter 5 and to more fully investigate the effects seen in the earlier work (Seymour, Krupczak, Jr. and Stegeman, 1984; Seymour, Koteles and Stegeman, 1982). The frequency regime and the properties of metals at these frequencies places the coupling measurements in a region that is unexplored from the viewpoint of "optical" waveguide techniques. As such, the first-order grating theories which assume small-amplitude corrugations are subjected to a new limit, in which the corrugation is small compared to the wavelength, but large

compared to the skin-depth of the metal. The experimental results clearly indicate that the first-order theories are inadequate in this regime.

The present experiments realized a substantial improvement over previous overcoated-mode experiments by the use of silicon as the overcoating material. The list of low-loss dielectrics in the far infrared is extremely short; there are presently only four polymers and five other compounds (mostly intrinsic semiconductors) with bulk absorption coefficients below 5 cm^{-1} (Chantry, Fleming, Smith, Cudby and Willis, 1971; Loewenstein, Smith and Morgan, 1973; Passchier, Honijk, Mandel, and Afsar, 1977). Of these, by far the lowest is silicon at $\approx 0.5 \text{ cm}^{-1}$, and since it has the second highest refractive index (Passchier, Honijk, Mandel, and Afsar, 1977) it stands out as the best material for use as an overcoating. A high index causes strong perturbations in β at relatively small thicknesses. In previous studies of the overcoated mode (Seymour, Krupczak, Jr. and Stegeman, 1984), polyethylene was used as the overlayer, with a refractive index of approximately 1.5. A silicon overlayer of a given thickness has roughly the same perturbative effect as a polymer film of greater than twice the thickness, and has far lower absorption. Our measurements were made on samples with coating thicknesses of between $2 \mu\text{m}$ and $5 \mu\text{m}$.

The chemical-vapor deposition of the silicon onto the samples at elevated temperatures provided high quality intrinsic silicon films, but required that a cap layer of silicon nitride be deposited on the metal surface prior to the CVD process to prevent the diffusion of the of the silver into the silicon. Because of its extreme thinness (130 \AA), this layer was ignored in the analysis of the results. The absorption coefficient may be much higher, but the amount of energy in the film is negligible.

The chapters that follow contain the necessary information for the comprehension, and reproduction, of the results that were obtained. In the experiments discussed in this dissertation, the overcoated surface plasmon mode was subjected to a set of controlled conditions, providing definitive illustration of the propagation and coupling properties of the mode. Although additional work is needed in order to determine its technological utility, for future communications applications, it is unlikely that surface plasmons could be utilized in the far infrared without a dielectric overcoating.

CHAPTER 2

THEORY

This chapter presents the necessary electromagnetic theory to quantitatively understand the mode being studied. First, Maxwell's equations are given, along with the assumptions that are appropriate for this application, and the surface plasmon mode equations are developed. Next the Drude model, which describes the optical properties of metals, is presented and incorporated into the surface plasmon equations. After examining the behavior of the bare-metal surface plasmon in the low-frequency limit, the overcoated mode is presented.

Maxwell's Equations

The fundamental equations which describe electromagnetic fields are Maxwell's equations, which relate the electric field E , the displacement field D , the magnetic field H , and the magnetic induction B . In this dissertation, MKS units will be used throughout. The equations are as follows (Lorrain and Corson, 1970)

$$\nabla \cdot \vec{D} = \rho_f \quad (2.1)$$

$$\nabla \cdot \vec{B} = 0 \quad (2.2)$$

$$\nabla \times \vec{E} + \frac{\partial \vec{B}}{\partial t} = 0 \quad (2.3)$$

$$\nabla \times \vec{H} - \frac{\partial \vec{D}}{\partial t} = \vec{J}_f \quad (2.4)$$

where ρ_f and \vec{J}_f are free charge and current, respectively. In general, all the terms (except t and ρ_f) are vector quantities. There are two corollary relationships,

$$\vec{D} = \epsilon_0 \vec{E} + \vec{P} \quad (2.5)$$

and

$$\vec{B} = \mu_0 (\vec{H} + \vec{M}) \quad (2.6)$$

where \vec{P} is the electric polarization, \vec{M} is the magnetization, ϵ_0 is the permittivity of free space, and μ_0 is the permeability of free space. We are dealing with non-magnetic materials, for which $\vec{M}=0$, and with situations in which there are no free charges present, so that ρ_f and \vec{J}_f are both zero. Moreover, we will be concerned only with fields that vary with time harmonically with a single frequency ω , so that the time derivative of a field \vec{V} is $i\omega\vec{V}$. The quantity \vec{P} contains the optical properties of media (when $\vec{M}=0$), and it is usually proportional to the electric field (linear optics) with a constant of proportionality of $\epsilon_0\chi$, so that

$$\vec{D} = \epsilon_0 \epsilon \vec{E} \quad (2.7)$$

where $\epsilon (=1+\chi)$ is called the "relative permittivity" or the (relative) "dielectric constant" of the medium. We will use the latter term, even though it is not strictly a constant. The frequency and spatial dependence of this term determines how electromagnetic fields interact with matter.

The previous equations can be combined to yield a wave equation which predicts a propagating electromagnetic wave. Taking the curl of Eq (2.3) and substituting Eq.(2.6), Eq.(2.4), and Eq. (2.5) with $\vec{M}=0$, we have the result that for a linear, homogeneous, isotropic medium,

$$\nabla^2 \vec{E} - \epsilon_0 \mu_0 \frac{\partial^2 \vec{E}}{\partial t^2} = \nabla(\nabla \cdot \vec{E}) + \mu_0 \frac{\partial \vec{J}_f}{\partial t} + \mu_0 \frac{\partial^2 \vec{P}}{\partial t^2} \quad (2.8)$$

With no sources present, this reduces to the homogeneous wave equation

$$\nabla^2 \vec{E} - \epsilon_0 \mu_0 \frac{\partial^2 \vec{E}}{\partial t^2} - \mu_0 \frac{\partial^2 \vec{P}}{\partial t^2} = 0 . \quad (2.9)$$

which is further reduced, using Eqs.(2.5) and (2.7), to the usual form

$$\nabla^2 \vec{E} + \epsilon \epsilon_0 \mu_0 \omega^2 \vec{E} = 0 . \quad (2.10)$$

Guided Waves

An important class of solutions to Eq.(2.10) represents guided waves, wherein energy can be confined over long distances to transverse regions on the order of λ^2 in area, with correspondingly high electric fields. The confinement allows the energy to be transported in a controlled low-loss manner, a characteristic useful for communications, and signal processing in general. The high fields of the guided wave increase the interaction between the electromagnetic wave and the matter that it is passing through. This is exploited in non-linear experiments, where high fields are essential, and where the long interaction length that the mode provides is an added benefit. Surface studies are another application of guided waves, where the surface-altered dielectric properties of the material may be revealed by the guided-wave mode.

An important property of a guided wave is that the fields are bounded in one or more directions perpendicular to the propagation direction. (There may also be a loss or attenuation term which limits the propagation distance.) The region to which the wave is confined is the "waveguide," and the region in which the field amplitude

decays away is called (depending on the particular geometry) the substrate, the cladding, or simply the bounding media. The mathematical form which guarantees confinement is an exponential decay of the fundamental field amplitudes (electric and magnetic) as a function of distance into the bounding media. The fundamental property of a guided wave is that the wavevector parallel to the direction of propagation (denoted by β) is larger than the wavevector of a plane wave propagating in any of the bounding media. This condition guarantees that the electric field will decay exponentially in the bounding media: in the bounding media the wave is "evanescent." Examples of optical waveguides are fibers and thin film waveguides.

Surface Plasmon Equations

For a "surface-guided" wave the region to which the mode is confined is an interface. In this case, all of the energy of the wave is contained in the bounding media, where the fields are evanescent. This is not at all incompatible with the concept of an electromagnetic wave, since the mode propagates along the interface with a well-defined β and with a single field in each medium. We can show the features of this mode by proposing a solution which fits the criteria and investigating the necessary conditions for it to exist. The geometry for this discussion is shown in Figure 2.1. The interface is in the xy -plane, and the mode is travelling from left to right. The media are assumed to be optically isotropic and we neglect spatial dispersion. The media are also assumed to be non-magnetic, so that μ_a and μ_b , the relative magnetic impermeabilities, are set equal to one. For convenience we will propose as the fundamental field a magnetic field polarized in the y -direction:

$$n_b \ (z < 0) : \quad \vec{H} = \hat{j} C_{TM} \exp[i(\omega t - \beta x) + \alpha z] \quad (2.11a)$$

satisfying the homogeneous wave equation if

$$\alpha^2 = \beta^2 - \epsilon_b \frac{\omega^2}{c^2} ; \quad (2.11b)$$

$$n_a \ (z > 0) : \quad \vec{H} = \hat{j} C_{TM} \exp[i(\omega t - \beta x) - \gamma z] \quad (2.12a)$$

satisfying the homogeneous wave equation if

$$\gamma^2 = \beta^2 - \epsilon_a \frac{\omega^2}{c^2} . \quad (2.12b)$$

Continuity of the tangential magnetic field at the interface is assured by the form assumed for the solutions. From Eqs. (2.4) and (2.7) (with $\vec{J}=0$),

$$n_b : \quad E_x = C_{TM} \frac{i\alpha}{\omega \epsilon_0 \epsilon_b} \exp[i(\omega t - \beta x) + \alpha z] , \quad (2.13a)$$

$$n_a : \quad E_x = -C_{TM} \frac{i\gamma}{\omega \epsilon_0 \epsilon_a} \exp[i(\omega t - \beta x) - \gamma z] , \quad (2.13b)$$

and continuity of E_x requires that

$$\frac{\alpha}{\epsilon_b} = -\frac{\gamma}{\epsilon_a} . \quad (2.14)$$

At frequencies for which ϵ_a or ϵ_b is negative, Eq.(2.14) can be satisfied. Let us choose ϵ_a to be negative; the terminology is to call n_a the "active medium." The assumption of optical isotropy allows any solution of the wave equation to be decomposed into two sets, transverse-electric (TE) and transverse-magnetic (TM). The wave we have proposed is a TM-mode since the magnetic field is completely polarized perpendicular to the propagation direction. It can easily be shown that for a TE-mode to exist requires that $\alpha^2 = -\gamma^2$, in violation of the initial assumption that both of the decay parameters α and γ have positive real components. Therefore the

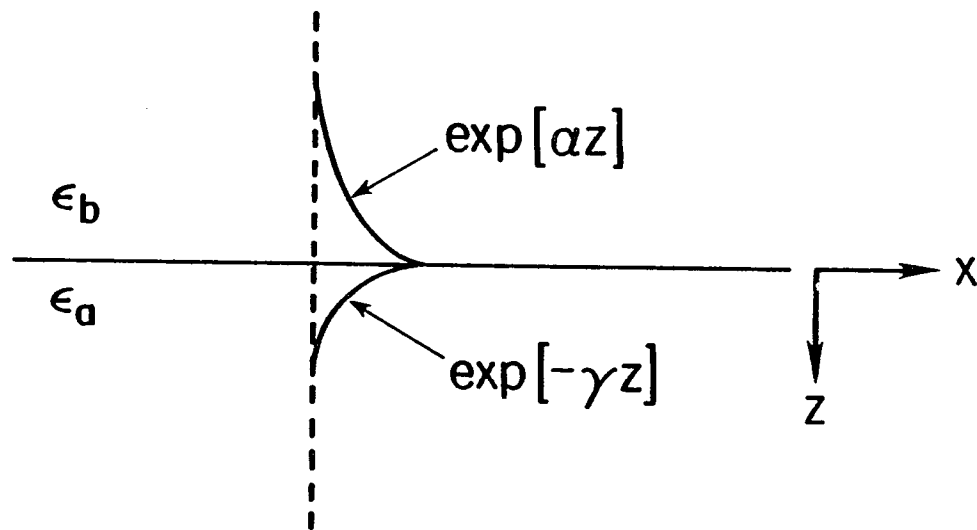


Figure 2.1. The geometry for the surface plasmon. The lower medium is the "active" medium, with a negative dielectric constant. The arrows point to a representation of the electric field strength of the surface-guided wave.

surface-guided wave is always a TM wave (unless the media have unequal magnetic permeabilities).

Squaring Eq.(2.14) and substituting the relations for α^2 and γ^2 from Eqs. (2.11b) and (2.12b), one obtains the dispersion relation

$$\beta = k_0 \sqrt{\frac{\epsilon_a \epsilon_b}{\epsilon_a + \epsilon_b}} \quad \text{where } k_0 = \frac{\omega}{c} \quad (2.15)$$

for the propagation wavevector β . The phase velocity of the mode is given by

$$v = \frac{\omega}{\beta}. \quad (2.16)$$

The requirement that β be primarily real gives

$$|\text{Re}\{\epsilon_a\}| > \epsilon_b$$

The very important property caused by the condition $\beta > k_0$ is that the surface plasmon cannot directly couple into bulk waves in air, nor vice versa. The phase velocity of the surface plasmon is slower than the bulk wave of the same frequency. In order to allow coupling to occur, the wavevector of the bulk wave must be increased to allow phase-matching between the two modes. This subject will be treated in detail in Chapter 6, where an experimental study of the coupling properties is discussed.

Properties of Metals (The Drude Model)

We have seen that the surface-guided wave can exist when one of the bounding media has a dielectric constant with a negative real part. This can occur in polar solids in the frequency range between the transverse optical phonon frequency ω_{TO} and the longitudinal optical phonon frequency ω_{LO} , the region of

anomalous dispersion. It also occurs in metals (in which $\omega_{TO} \rightarrow 0$ and ω_{LO} corresponds to the plasma oscillation frequency) in the corresponding frequency range. The surface-guided wave at a metal-dielectric interface is called a surface plasmon, which is the mode of interest for this dissertation.

The optical properties of metals are determined almost solely by the conduction electrons. In a good metal, approximately one electron per atom is contributed to the conduction band where it becomes almost completely delocalized from its parent atom. These electrons form what is usually called an electron gas, which acts to shield the atoms with their remaining electrons from applied electromagnetic fields. These "conduction" electrons are displaced by an applied electromagnetic field. We write the incident field as

$$E = \frac{1}{2} E_{inc} \exp[i(\omega t - kx)] + c.c. \quad (2.18)$$

The electron displacement q is assumed to be parallel to the electric field, with an amplitude Q ;

$$q = \frac{1}{2} Q \exp[i(\omega t - kx)] + c.c., \quad (2.19)$$

and is governed by the force balance equation

$$m^* \left[\frac{\partial^2 q}{\partial t^2} + \left(\frac{1}{\tau} \right) \frac{\partial q}{\partial t} \right] = eE_{inc} \quad (2.20)$$

where m^* is the electron effective mass and τ is called the Drude relaxation time. (τ represents the mean free lifetime of the conduction electrons.) Solving Eq.(2.20) gives

$$Q = \left[-\frac{e}{m^* \omega \left(\omega - \frac{i}{\tau} \right)} \right] E_{inc} \quad (2.21)$$

and the induced macroscopic polarization $P = NeQ$, is

$$P = \left[-\frac{Ne^2}{m^* \omega \left(\omega - \frac{i}{\tau} \right)} \right] E_{inc} \quad (2.22)$$

where N is the number of conduction electrons per unit volume. This last equation identifies the quantity $\epsilon_0 \chi$ preceding Eq.(2.7). Therefore, utilizing Eqs. (2.5) and (2.7), the dielectric constant of the metal is given by

$$\epsilon_m = 1 - \frac{\omega_p^2}{\omega \left(\omega - \frac{i}{\tau} \right)} \quad (2.23)$$

with

$$\omega_p^2 = \frac{Ne^2}{m^* \epsilon_0} . \quad (2.24)$$

The parameter ω_p is called the plasma resonance frequency and corresponds to ω_{LO} in a polar solid since the real part of the dielectric constant approximately vanishes when $\omega = \omega_p$. We identify the metal refractive index, n_m , as

$$n_m^2 = \epsilon_m . \quad (2.25)$$

This theory (the Drude or "nearly-free electron" model; Drude, 1900) tells us that the dielectric constant of a metal will be negative at frequencies below ω_p , which is in the visible or the near-uv spectral region for the noble metals. From Eq.(2.17), surface plasmons can exist at all frequencies below $\omega_p/\sqrt{1+n}$. The strong dependence of ϵ_m on frequency (Eq.(2.24)) implies that the surface plasmon wavevector β is also frequency dependent. We can separate Eq.(2.23) into real and

imaginary components,

$$\epsilon_m = \epsilon'_m + i\epsilon''_m \quad (2.26)$$

where

$$\epsilon'_m = 1 - \frac{\omega_p^2}{\omega^2 + \frac{1}{\tau^2}} \quad (2.27)$$

and

$$\epsilon''_m = -\frac{\omega_p^2/\tau}{\omega\left(\omega^2 + \frac{1}{\tau^2}\right)}. \quad (2.28)$$

In the low frequency (far-infrared) region, where $(\omega_p/\omega)^2 \gg 1$ (simplifying Eq.(2.27)), and in the limit $\beta_R \gg \beta_I$,

$$\beta = \beta_R + i\beta_I = n_b k \left[1 + \frac{n_b^2 \omega^2}{2\omega_p^2} \right] - i \frac{n_b^3 k \omega}{2\omega_p \tau} \quad (2.29)$$

The variation of β_R with frequency is shown in Figure 2.2. An imaginary component of β results in a finite propagation length for the surface plasmon. In fact Figure 2.2 shows only one slice of the total local dispersion relation, one for which ω is taken as real and k as a complex quantity (Boardman, 1982; Ritchie, Hamm, Williams and Arakawa, 1977; Kuwarama, Yokota, Fukui and Tada, 1982).

Let us examine the behavior of the tranverse decay coefficients α and γ with decreasing frequency. For $\omega_p \gg \omega$, (from Eqs. (2.11b), (2.12b), (2.14), and (2.27)),

$$\alpha \cong \epsilon_b \frac{\omega^2}{\omega_p c} \sqrt{1 + (\omega\tau)^{-2}} \quad (2.30)$$

and

$$\gamma \cong \frac{\omega_p}{c} \frac{1}{\sqrt{1 + (\omega\tau)^{-2}}}. \quad (2.31)$$

For $\omega \geq \tau$, the field penetration in the metal remains approximately constant, whereas the penetration distance into the dielectric increases with decreasing

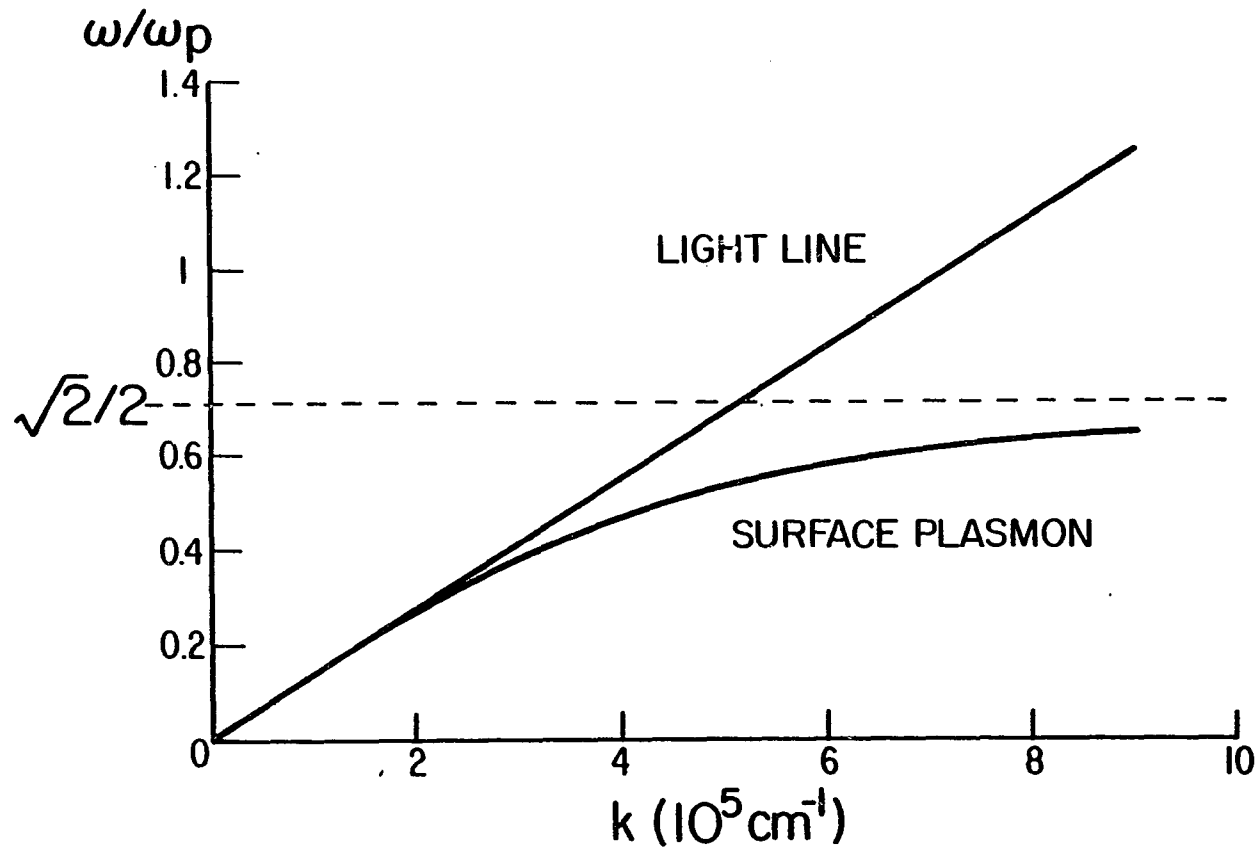


Figure 2.2. The frequency dispersion of a surface plasmon. At large k , the frequency approaches an asymptotic limit. Shown is the classic case of a metal-air interface, for which the limit is $\omega_p/\sqrt{2}$. At low frequencies the dispersion relation approaches that of a plane wave in the upper medium. Another solution (not shown) exists above the light line. That mode is not bound to the surface (Brewster mode).

frequency. For $\omega < \tau$, the field penetration in the metal decreases with frequency (typically 300-500 angstroms in the far infrared), and the penetration into the dielectric still increases with frequency. In both situations, this is indicative of progressively weaker coupling between the electromagnetic field and the electron gas. As the mode becomes more weakly bound to the interface, the wavevector β approaches that of a freely propagating plane wave in medium n_b , and the field there becomes more plane wave in character. The propagation distance increases because the fraction of the energy carried by the metal, the dissipative medium, decreases as the frequency decreases.

$\omega \rightarrow 0$: The Far Infrared

At far-infrared frequencies the surface plasmon becomes so photon-like that it has very poor guided-wave properties. The exponential tail into the air extends many hundreds of wavelengths, and the fraction of the energy in the metal becomes vanishingly small. This results in extremely long propagation lengths, but they cannot be exploited because the weak binding allows radiative scattering of the wave to become the dominant loss mechanism. From an experimental point of view, the delocalization occurring in the far-infrared causes the surface plasmon to be extremely difficult to control. The near match of wave-vector between a bulk wave in the upper medium and the surface plasmon means that it is very difficult to selectively excite a surface plasma wave. The slightest angular spread in the excitation field results in a portion of it propagating along the interface in the form of a radiation field. This "surface-skimming" wave effectively shares the same wavevector and spatial distribution as the surface plasmon, making it virtually impossible to eliminate.

Overcoated Surface Plasmon Mode

The properties of the surface plasmon are altered by the presence of a dielectric overlayer. These changes are most dramatic in the far infrared where β is so close to the light line. The changes in the properties are a consequence of the shift in β induced by the dielectric film. The analysis of the mode is a two-boundary problem, where the index of the dielectric film is higher than that of the upper medium (Stegeman and Seymour, 1982). Although the upper medium is assumed to be air in the text, for generality the equations will retain an arbitrary index for the upper medium. Referring to the geometry shown in Figure 2.3, the fundamental field is again a y-polarized magnetic field:

$$\text{air:} \quad \vec{H} = \hat{j}C_{TM} \exp [i(\omega t - \beta x) + \alpha_1(z+h)] \quad (z < -h) \quad (2.32a)$$

$$\alpha_1^2 = \beta^2 - n_1^2 k_0^2 \quad (2.32b)$$

$$\text{film:} \quad \vec{H} = \hat{j}C_{TM} \exp[i(\omega t - \beta x)][A^+ \exp(i\alpha_2 z) + A^- \exp(-i\alpha_2 z)] \quad (2.33a)$$

$$\alpha_2^2 = n_2^2 k_0^2 - \beta^2 \quad (-h > z > 0) \quad (2.33b)$$

$$\text{metal:} \quad \vec{H} = \hat{j}C_{TM} A_3 \exp[i(\omega t - \beta x) - \alpha_3 z] \quad (z > 0) \quad (2.34a)$$

$$\alpha_3^2 = \beta^2 - n_3^2 k_0^2 \quad (2.34b)$$

From the continuity of H_y and E_x at the air-film interface,

$$A^+ = \frac{1}{2} \left[1 - i \frac{\alpha_1 n_2^2}{\alpha_2 n_1^2} \right] \exp(i\alpha_2 h) \quad (2.35)$$

$$A^- = \frac{1}{2} \left[1 + i \frac{\alpha_1 n_2^2}{\alpha_2 n_1^2} \right] \exp(-i\alpha_2 h) \quad (2.36)$$

and from the continuity of H_y at the film-metal interface,

$$A_3 = \cos_c(\alpha_2 h) + \frac{\alpha_1 n_2^2}{\alpha_2 n_1^2} \sin_c(\alpha_2 h) \quad (2.37)$$

from which the dispersion relation is derived:

$$\tan_c(\alpha_2 h) = \left[\frac{\alpha_2 n_2^2 (\alpha_1 n_3^2 + \alpha_3 n_1^2)}{\alpha_2^2 n_1^2 n_3^2 - \alpha_1 \alpha_3 n_2^4} \right]. \quad (2.38)$$

The subscript "c" refers to trigonometric functions with complex arguments.

The value of C_{TM} which normalizes the power to one watt per unit width in the y-direction is

$$C_{TM} = \sqrt{\frac{4k c \epsilon_0}{K}} \quad (2.39)$$

where

$$K = \frac{\beta + \beta^*}{2\alpha_{1r} n_1^2} + \frac{1}{2\alpha_{3r}} \left[\frac{\beta}{n_3^2} + \frac{\beta^*}{n_3^{*2}} \right] + \left[\frac{\beta}{n_2^2} + \frac{\beta^*}{n_2^{*2}} \right]$$

$$\times \left[\frac{A_+ A_+^*}{\alpha_{2i}} \sinh(2\alpha_{2i} h) + \frac{\sin(\alpha_{2r} h)}{\alpha_{2r}} [A_+ A_-^* \exp(-i\alpha_{2r} h) + A_+^* A_- \exp(i\alpha_{2r} h)] \right]$$

where

$$\begin{aligned} \alpha_{j,r} &= \alpha_j + \alpha_j^* \\ \alpha_{j,i} &= \alpha_j - \alpha_j^* \end{aligned} \quad (2.40)$$

All of the preceding equations are valid when the refractive indices are complex.

The dispersion relation may be solved numerically to produce a solution for β , the complex wavevector. The penetration depths, propagation length, and coupling angle are then calculated from β . The effect of the overlayer is to perturb β_R to a larger value. This shift is generally small (0.1-10% of k_0), but even very small shifts in β produce large relative changes in α_1 , because α_1^2 is the difference between β^2 and $n_1 k_0^2$. The increase in α_1 results in a much shorter field penetration into the

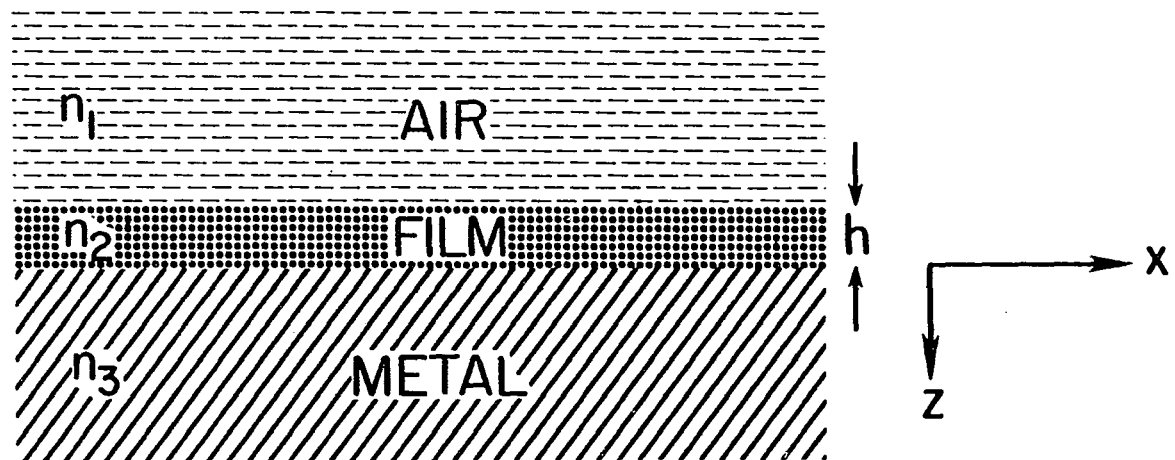


Figure 2.3. The geometry of the overcoated surface plasmon mode. The dielectric film, for which $n_1 < n_2$, occupies the region $-h < z < 0$. The overcoated surface plasmon fields decay exponentially from the interfaces in the regions $z < -h$ and $z > 0$.

air. Figure 2.4 shows how dramatic the change in α_1 is. The plot shows the penetration distance ($1/\alpha_1$) into air as a function of film thickness for a silicon overlayer ($n=3.418$). The addition of less than $1 \mu\text{m}$ of silicon reduces the penetration distance to well under 1 mm. This is an amplitude-coefficient; the energy penetrates only half as far. Figures 2.5 and 2.6 show the behavior of β_R and β_I as a function of overlayer thickness, also for silicon. The perturbation of β_R to larger values is the effect that eliminates the surface-skimming wave.

β_I is usually represented by the propagation constant α (not to be confused with the α_j which are the evanescent field decay parameters). It represents the $1/e$ propagation distance of the Poynting vector (signifying the energy propagation length). Recall that without the overcoating, the propagation distance is very large, on the order of meters; the tradeoff of an improved localization and boundedness is the reduction in the distance that the surface plasmon will propagate. We will see in the course of this dissertation that the properties of the overcoated mode more than compensate for the increase in the attenuation coefficient.

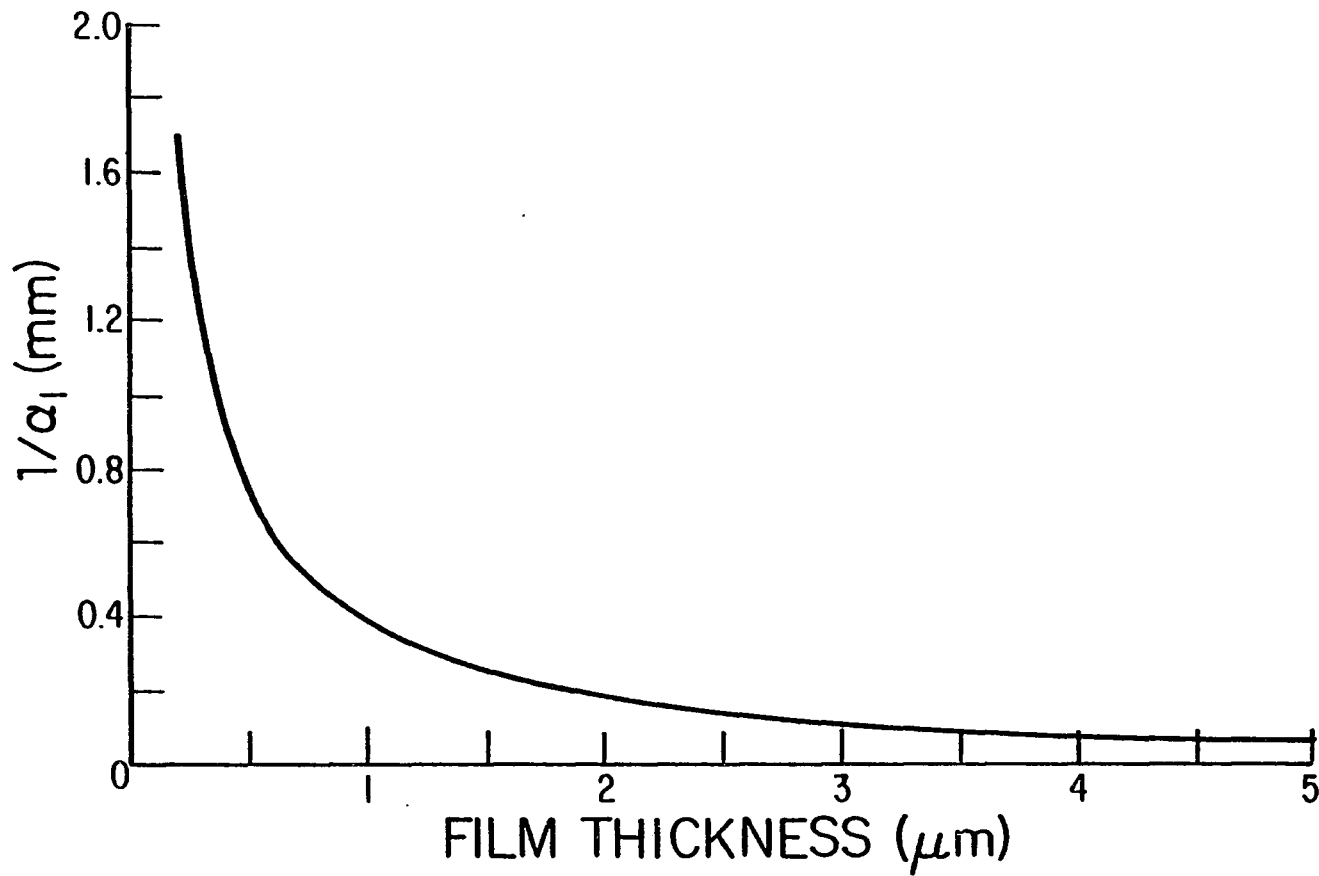


Figure 2.4. The penetration depth of the surface plasmon fields into the upper medium as a function of overlayer thickness. This plot is for a silicon ($n=3.418$) film on silver (see text) at a wavelength of $118.8 \mu\text{m}$. At $t=0$, the penetration depth is approximately 16 mm.

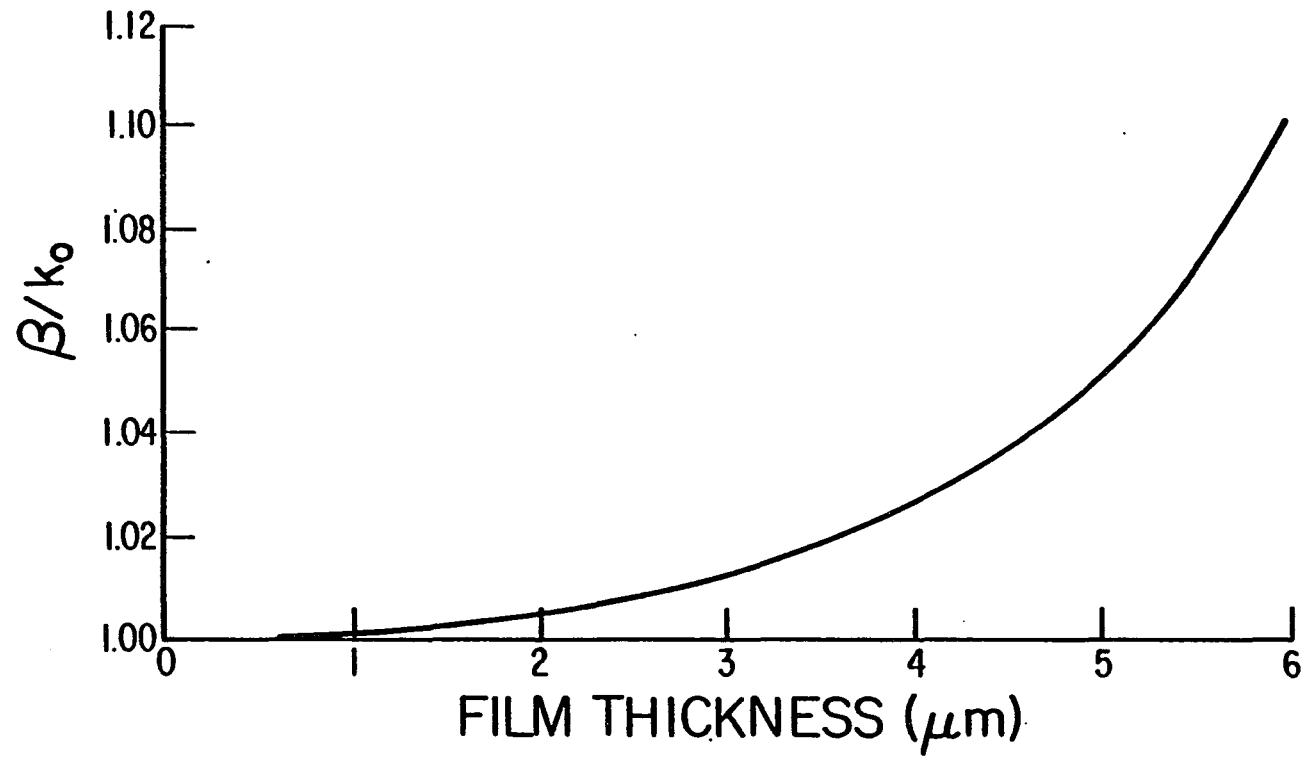


Figure 2.5. The perturbation of β_R by the overcoating. This plot is for a silicon ($n=3.418$) film on silver (see text) at a wavelength of $118.8 \mu\text{m}$.

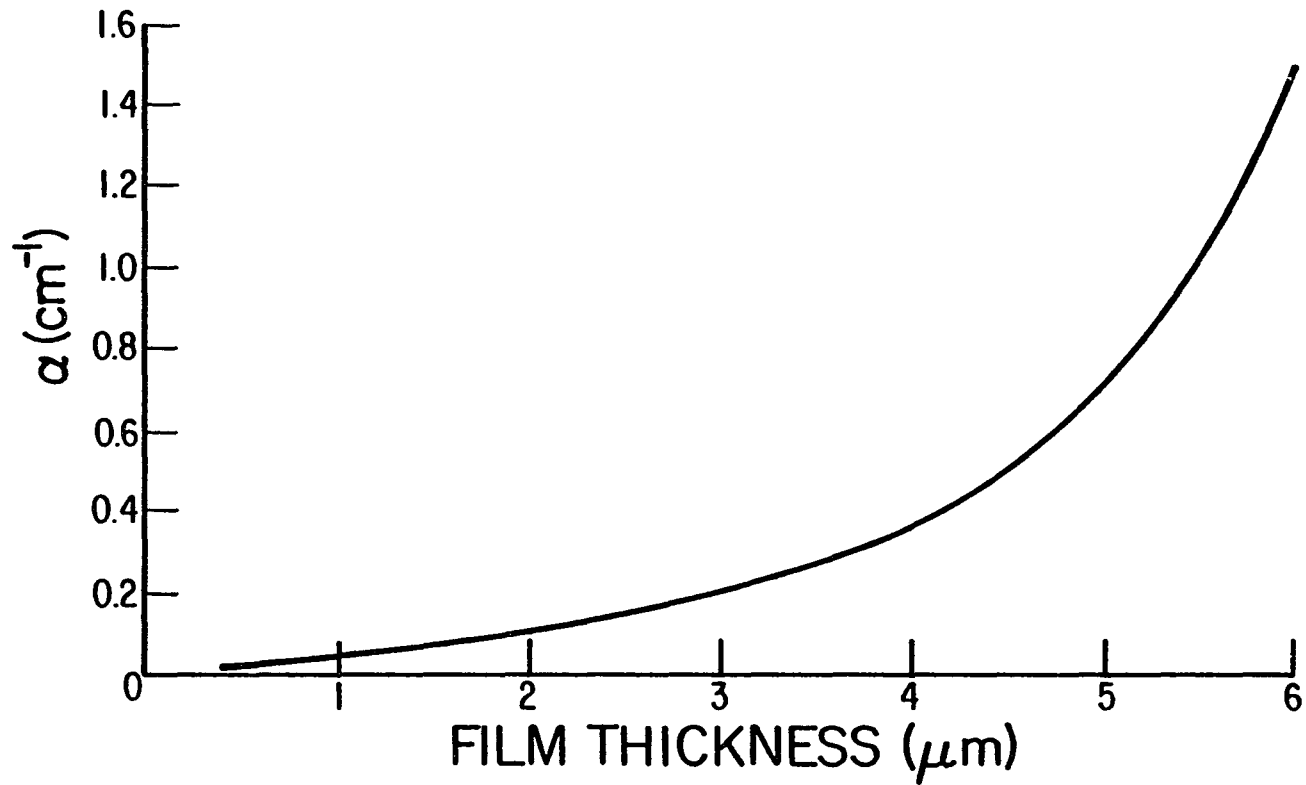


Figure 2.6. The attenuation of the mode as a function of coating thickness. This represents an energy parameter ($\alpha=2\beta_I$). This plot is for a silicon ($n=3.418$) film on silver (based on the Drude model) at a wavelength of $118.8 \mu\text{m}$. The propagation length without an overlayer is several meters.

CHAPTER 3

EXPERIMENTAL SETUP

The apparatus used in the experimental work consisted of three major parts: The laser and associated electronics, the mechanical assembly for controlling the sample, and the optics, detectors and electronics for controlling and detecting the radiation. The laser provided a stable source of radiation at a single wavelength (118.8 μm) for the experiment. This radiation was aligned, collimated and directed onto a grating which formed the input coupler of a surface plasmon waveguide. After propagation through the waveguide, the beam was decoupled and detected by a pyroelectric detector. The signal was sent to a lock-in amplifier whose output was recorded on a strip-chart recorder.

The source was an Apollo model 120 far-infrared (FIR) laser with cavity-stabilization electronics. This laser consisted of a 1.5 m plane-parallel Fabry-Perot cavity filled with low-pressure methanol vapor, pumped by a CO_2 flowing-gas laser. The 9P_{36} line of the CO_2 laser excited a rotational transition (ν_8 band, 15(0,2,7)) in the methanol vapor (Butler, 1983). The system was designed for, and was used at the 118.8 μm line (2530 GHz), one of the strongest far infrared transitions, and was run in "continuous-wave" operation. The output was linearly polarized, in a direction perpendicular to the polarization of the pump beam.

The stabilization system used two PZT drivers (one per cavity) which modulated the length of the cavities. A 16 Hz sinusoidal voltage was applied to the PZT on the CO_2 laser cavity, and a 40 Hz signal was applied to the PZT on the

methanol laser cavity. The modulation of the cavities' lengths modulated the output power of the lasers by tuning around the peak of the cavities' resonance condition. The FIR laser power was modulated once by the modulation of the pump beam, and a second time by the PZT connected to the cavity. A beamsplitter was used to direct a portion of the doubly-modulated FIR signal to a pyroelectric detector, and the output was fed back to the stabilization electronics. The stabilization circuitry determined the appropriate d.c. voltage to apply to both drivers to keep the disturbance signals 90° out of phase with the feedback, holding the desired line and maintaining maximum output power from each cavity. A motor-driven linkage provided manual adjustment of the cavity length to compensate for the finite range of the PZT.

The methanol cavity had plane-parallel mirrors with a 2 mm hole in one mirror to admit the CO_2 pump beam, and a 1 cm diameter partial-reflector in the other mirror as an output coupler for the $118.8 \mu\text{m}$ radiation. The beam that the laser provided was not a TEM_{00} mode. The laser lased only on points along a ring in the plane of the output coupler, a shape it assumed because it duplicated that of the pump beam, and because of the hole in one of the end mirrors. In general one or more spots on the ring would lase, with a residual of power in the rest of the ring. The longitudinal line that was used for the experiments was a single well-defined "hot spot," located near the edge of the output coupler, that contained nearly all of the total output power. In the near-field the intensity profile was slightly elliptical in shape, with the major axis 45° to the vertical. The residual power in the ring was blocked at the output coupler. The resulting laser beam had the following characteristics: the near-field pattern was a single spot, slightly vertically elongated,

with diameter of $2 \pm 1/2$ mm. The beam radiated from a position approximately 3 mm from the center of the 1.0 cm output coupler, and contained a power of 3-4 mW. The power was measured with a Scientech model 362 power meter, which uses a thermopile detector. It has been shown to be effective at sub-millimeter wavelengths, using the appropriate calibration factors (Foote, Hodges and Dyson, 1981).

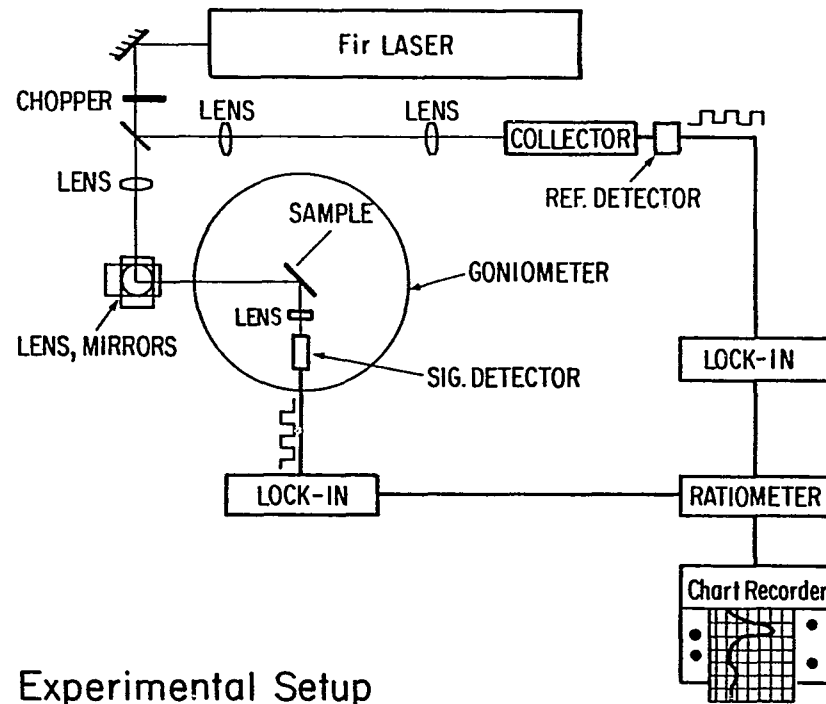
The remainder of the layout on the optical table served to direct the beam onto the sample, in a form suitable for coupling into the grating. In particular this meant that the beam had to have the correct polarization, diameter, phase front and alignment when it reached the input coupler. Figure 3.1 is a diagram of the layout, which sat on a 4'x10' optical table.

It was necessary to split off a portion of the laser beam to serve as a reference for removing laser power fluctuations; the "test" signal was divided by the reference signal with a ratiometer. For greater experimental precision it was desirable that the ratio of test to reference power stay constant on a day-to-day time scale. Since submillimeter radiation is strongly absorbed by water vapor, the ratio would change with room humidity if the two optical paths were different in length. The signal at the sample and at the reference detector obey the following relations:

$$I_{\text{ref}} \propto \exp[-\alpha_h L_1] \quad (3.1)$$

$$I_{\text{signal}} \propto \exp[-\alpha_h L_2] \quad (3.2)$$

where α_h is an absorption coefficient due to water vapor, and L_1 and L_2 are the lengths of the reference and signal arms respectively. Therefore



Experimental Setup

Figure 3.1. The apparatus for the experiments. The beam was split into two arms, then recombined at the ratiometer, to divide out long-term fluctuations in the laser power. Lenses imaged the laser's output coupler onto an input grating of the sample. The lens/mirror combination to the left of the goniometer represents a vertical section of the optical path, out of the plane of the figure.

$$\frac{I_{\text{signal}}}{I_{\text{ref}}} \propto \exp[\alpha_h(L_1-L_2)] \quad (3.3)$$

and the ratio is independent of the room humidity only if $L_2 = L_1$. If $L_2 = L_1$, then the constancy of the ratio can be used to detect changes in the laser mode or the alignment of the set-up.

The beam in the arm containing the waveguide required some optics between the laser output coupler and the waveguide in order to have the appropriate beam diameter and phase front for coupling. This was done with two simple lenses of TPX (poly 4-methyl-1-pentene), a polymer which transmits in the far infrared and in the visible. Both were identical plano-convex, 50 cm f.l. F/10, mounted with the plano sides facing each other to minimize spherical aberration. The lenses were positioned so as to image the plane of the output coupler onto the grating. This minimized the effects of diffraction at the output coupler, and presented a smooth phase front to the grating. A "4F" configuration was used, in which the object-to-image distance is four focal lengths and the inter-element separation is 2F. In addition to imaging the portion of the beam that was diffracted by the output coupler, this configuration ensures that the non-diffracted beam is collimated when it reaches the grating. At the grating, the beam dimensions were approximately 7.0 mm vertically by 7.5 mm horizontally, consistent with the diffraction-limited performance of the lenses. The angular divergence of the beam was approximately 1° (half-angle). Note that using two mirrors to raise the beam height and redirect the beam by 90° also caused a 90° transverse rotation of the beam. For our set-up this provided the correct (horizontal) polarization as well. After reflection by the sample, the beam was gathered by a collecting lens (TPX, 9.5 cm f.l., F/5) and detected with a 5 mm diameter pyroelectric detector.

In the reference arm, the emphasis was on collecting all of the energy; because the "test" signal would be divided by the reference this would strongly affect the final signal-to-noise ratio. The available detector was 2 millimeters in diameter, and with a 1 centimeter beam, it is impossible to produce a 2 mm spot size with simple lenses. For this reason the final element was a light-collecting cone with a 2 cm input diameter and a 2 mm output diameter. The light-collecting cone is a common millimeter- or micro-wave device which takes the place of a lens in those spectral regions. It is not a refractive device but is actually a hollow metal waveguide which is tapered to collect or concentrate the radiation. The transmission of this device compared favorably with an F/4 TPX simple lens with a 2 cm aperture (which could not be used because the focal spot is larger than 2 mm).

The first element in the reference arm was another 50 cm f.l. plano-convex TPX lens, located 50 cm from the output coupler. The next lens, 95.5 cm from the first, was a 25 cm f.l. F/5 plano-convex TPX. This faster element ensured that all the energy would get into the light-collecting cone. Another reason for using the light-collecting cone is that a non-refractive element is more suitable for collecting widely different transverse modes because it has no spherical aberration Φ its collection efficiency is relatively insensitive to the shape of the mode. Located at the two-millimeter output of the collecting cone was a 2 mm-diameter pyroelectric detector.

The radiation was detected with lithium-tantalate pyroelectric detectors, one of 5 mm diameter and several of 2 mm and 1 mm diameter, with a mechanical chopper operating at 36.6 Hz. The chopping frequency was limited by the possibility of beating with the 16 Hz or the 40 Hz modulation frequencies of the

cavity-stabilization electronics. These pyroelectric detectors are usually not advertised (or fabricated) for use in the far-infrared. The typical gold-black used as an absorber is known to be effective at these wavelengths, but no manufacturer-supplied window material is transparent in this region. The solution was to purchase them without windows. The larger detector, used in the "test" arm, was mounted in a small metal box with a TPX window. The reference detector was placed in close proximity to the light collecting cone, and a thin polypropylene film (6.25 μm -thick x-ray sample support) was used to seal the front of the collecting cone. The purpose of the window is to prevent air turbulence from reaching the pyroelectric film because that would cause a strong spurious signal. Since the 5 mm detector was imbedded in a styrofoam cell inside the metal box, it was well insulated from air motion. The reference detector was more vulnerable since it was constructed in a TO-5 can, so a foam jacket was placed around the detector/pre-amp box and the collecting cone. This was sufficient to insulate the detectors from the air turbulence caused by the room ventilation system.

The detectors were integrally mounted to FET-input operational amplifiers which were configured for high-gain voltage amplification ($R_f \cong 10^{12} \Omega$). The pre-amps were connected to lock-in amplifiers, the reference detector to a Princeton Applied Research PAR 121 lock-in and the signal detector to an Ithaco Dynatrac 393 lock-in with a built-in ratiometer. Measurements were made with a 125 ms time constant on the Ithaco and a 100 ms time constant on the PAR (they could not be set to the same τ). This time constant was chosen as the best compromise between low noise (large τ) and fast response (small τ).

The output of the PAR lock-in went to the Ithaco ratiometer unit as the denominator (reference signal). This output was 0-10 V dc. The numerator for the ratiometer was provided by the Ithaco lock-in and was also a 0-10 V dc signal. The numerator was typically 600 mV and the denominator was typically 185 mV. The output of the ratiometer was a 0-1 V dc signal, which was measured with a single-pen strip-chart recorder. The output voltage could be adjusted with a 10 dB potentiometer that was part of the ratiometer option. For some measurements this output was digitized with a 16-bit 0-10 V digitizer and stored on permanent magnetic media using an IBM PC interfaced to a CAMAC data acquisition system.

A Helium-Neon laser was aligned to be co-linear with the FIR beam for the purpose of maintaining a visible reference to the beam path. It was used to align the FIR beam to the input coupler, and to determine the exact position of the FIR beam with respect to the grating during coupling experiments.

The waveguide was mounted on a precision goniometer, which provided a platform that rotated the detector at twice the angle of the sample mount. This precisely tracked the zero-order diffracted beam (the specular reflection) from the grating on the sample as the input angle was changed. It was often necessary to collect the radiation from the -1-diffracted order as well. To allow this, the collecting lens and detector could be re-aligned to the -1 order beam and rotated with the diffracted beam. The alignment in this case is not exact, and this situation is discussed further in the experimental procedures section of Chapter 6.

The mechanical apparatus on which the sample was mounted was designed to allow vertical and horizontal translation of the sample without losing its alignment to the goniometer's axis of rotation. This allowed different gratings on the sample to be

moved into the beam. The apparatus was an xyz-translation stage, on top of which a vacuum chuck was mounted. One of the horizontal translation directions was in the direction of the normal to the sample surface. To align the sample, first the goniometer was moved until its axis of rotation (a vertical line) intersected the center of the beam waist. Then the sample was mounted and translated along the normal to its surface until it also intersected the rotation axis of the goniometer. This served to align the sample surface to the axis of rotation, and together to the center of the beam. The other horizontal translation direction was parallel to the surface, which along with the vertical translation allowed the sample's surface to be moved around without losing its alignment to the rotation axis.

The detector arm was also mounted on a stage which allowed horizontal translation of the detector assembly in a direction roughly parallel to the surface of the sample. This allowed the detector to be moved easily from the input grating (to monitor the 0-order reflection) to the output beam (to monitor the energy decoupled by the output grating). The detector arm was modified for coupling measurements in such a way as to allow the re-radiated energy to be measured as a function of position on the output grating. This experiment is discussed in more detail in the experimental procedures section of Chapter 6.

CHAPTER 4

SAMPLE FABRICATION

The samples on which the experiments were performed were each fabricated on a 7.5 cm diameter single crystal silicon wafer, manufactured by Wacker. The crystallographic orientation was 100, chosen for its chemical etching properties. The waveguide was fabricated on the polished side of the wafer, and consisted essentially of an optically thick layer of silver with an overcoating of silicon. The upper medium for the surface plasmon was air. Figure 4.1 shows the layout of the 1 cm x 1 cm gratings on the sample, forming 5 distinct waveguides for a surface plasmon travelling left-to-right or right-to-left across the wafer. The length of the waveguide is defined as the separation between the gratings, since in the grating regions the mode being investigated may be affected by the corrugation of the surface. Each sample had three different path lengths (1, 2 and 3 centimeters). The duplication of the path lengths was imposed partly by the geometry of the substrate, but also served to allow for the possibility of damage in the fabrication process. Each of the samples that were studied had a single overcoating thickness applied to them, with the mean thickness approximately equally spaced from 2.1 μm to 5.1 μm (see Table 4.1).

The first step in the wafer processing was to chemically etch the gratings into the substrate. We used a photolithographic process to create the etch pattern. The starting point for this was a commercially-made custom mask which was opaque except for the bar pattern seen in Figure 4.1. The silicon wafer was first coated

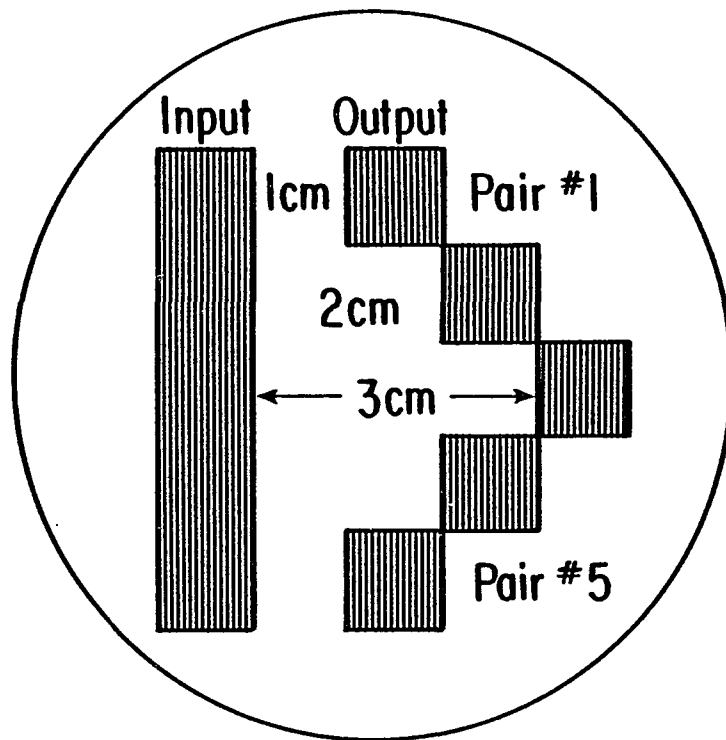
with silicon dioxide (thermally grown to $1\ \mu\text{m}$ in an oxidation furnace), and then coated with Shipley AZ1470 photoresist. The photoresist was exposed through the mask, so that only the area under the bar pattern was exposed to light. Then the resist was developed, removing the exposed photoresist. The remaining photoresist was baked for 1/2 hour at 120°C , to improve its adhesion to the surface. The oxide layer under the bar pattern, now uncovered, was stripped off with a buffered HF solution (7:1 ammonium fluoride to HF). The rest of the photoresist was then stripped with a sulfuric acid-hydrogen peroxide solution, leaving oxide (an etch barrier) covering the entire wafer except for the bar pattern. Then the wafer was etched in a 1:1 solution of potassium hydroxide and H_2O at a temperature of 100°C . The solution was covered with a 2-3-inch layer of 2-propanol as a buffer. The solution was agitated by bubbling nitrogen gas through it, and propanol evaporation was contained by flowing cold water in a jacket around the top of the etching container. Note that the propanol temperature was below 100°C ; it remained cooler than the solution below it. This solution etched the gratings to a depth of 6 microns ($7\ \mu\text{m}$ if the oxide layer is included) in about 3 minutes. The crystallographic orientation of the substrate causes the etching (which occurs along the 100 plane) to create a trapezoidal grating shape with the sides sloped at a precise angle of 54° . A number of wafers were etched to approximately 6 microns. After etching the gratings, the silicon-dioxide layer was completely stripped with buffered HF, and a new coating of $1.0\ \mu\text{m}$ of phosphor glass was applied using low-pressure chemical vapor deposition. This was heated and re-flowed to smooth the grating edges, to ensure that the silver coating would be continuous at the edges. The 7-8% phosphorus dopant allows the glass to flow at a moderately high temperature.

Figure 4.2 is an electron micrograph showing the cross-section of the grating. The sharp boundary of the silicon substrate is clearly visible, as is the trapezoidal grating profile. The phosphor glass is discernable on top of the silicon.

Seven wafers were then selected with grating depths of $6.0 \pm 0.2 \mu\text{m}$, peak-to-peak. On each sample, the grating depth varied only 1-3% over the entire wafer (10 gratings per wafer). The relatively deep gratings were chosen as a compromise: A shallow grating would demonstrate a stronger change in coupling efficiency with coating thickness than a deep grating, but a deep grating would give a higher overall efficiency. The former case is better for studying the coupling properties of the grating (see Chapter 6), and the latter case facilitates attenuation measurements by coupling more power into the surface plasmon. These seven wafers eventually became the actual samples that were used.

Next the silver coating was evaporated onto the sample. The evaporation process is a standard method of applying a metal coating. Under a high vacuum, a current is delivered to a tungsten "boat" which holds a quantity of the coating material. The metal is heated to its melting point, and it begins to evaporate. The vacuum allows the escaping atoms to travel in a straight line and stick to the cold surrounding surfaces. A sample placed in the chamber facing the boat becomes coated with an even layer of the evaporated material.

The evaporation was done one wafer at a time, with the wafer centered in the chamber, approximately 25 cm directly above the boat. The distance between the wafer and the boat was maximized to minimize the solid angle subtended by the wafer from the boat. Though more time-consuming than doing several at once, this method gave a more even coating thickness across the entire wafer. The 99.999%



Top view of Sample

Figure 4.1. The layout of the grating pattern on the 7.5 cm diameter substrate. There are ten 1cm x 1cm gratings (periodicity not to scale) forming five separate waveguides with three different path lengths. The roles of the input and the output gratings were reversible merely by rotating the sample 180° in the plane of the figure.



Figure 4.2. Electron micrographs of the grating cross-section (air above, substrate below). The thin layer discernable on the substrate is the reflowed phosphorus glass. The evaporated silver film is not visible. The grating period is $154.2 \mu\text{m}$, and the height is $6 \mu\text{m}$ peak-to-peak.

silver was evaporated at pressures ranging from 0.9×10^{-6} mbar to 1.25×10^{-6} mbar. A relatively high evaporation rate of $50\text{--}60 \text{ \AA}$ per second was chosen in order to make a smoother film. The thickness of the seven coatings ranged from $0.22\text{--}0.26 \text{ }\mu\text{m}$, with as much as a 20% variation in thickness over any single wafer. Since the penetration depth of the surface plasmon into the silver is roughly 500 \AA , it can be regarded as optically thick.

After the silver was deposited, a thin film of silicon nitride was reactively sputtered on top of the silver, using a DC magnetron to bombard a silicon source with nitrogen gas molecules. This layer served as a cap to prevent the silver from diffusing into the silicon overlayer which was to be deposited next. Silver has a high diffusion rate into silicon, and at the elevated temperatures of the chemical-vapor deposition process used to deposit the overlayer, the actual diffusion is rapid and would have produced a coating which was an alloy of silicon and silver. We determined that the alloying of the two materials was very effectively prevented by a layer of silicon nitride only 130 \AA thick.

The final fabrication step was the c-v deposition of the silicon overlayer onto six of the seven samples. In this step the samples were placed on a heating element called the susceptor (a graphite element with an RF coil embedded in it) and heated to 600°C in nitrogen at a pressure of one atmosphere. Then silane gas was passed over the sample and the silicon precipitated out onto the wafer. The deposition rate was 2500 \AA per minute. The rate was determined by measuring standards with an optical pyrometer after a calibration run. It was at this final stage that the seven samples became differentiable, as the silicon overlayer thickness was different on each one (with no overlayer on one sample). Figure 4.3 shows a cross-section of the

finished waveguide, with all the various coatings from the substrate to the overlayer.

The overlayer thickness was measured with a stylus-profilometer: Using a razor blade, a very small area ($\cong 1 \text{ mm} \times 0.2 \text{ mm}$) of the coating was scratched off. In most cases both the silicon coating and the silver film came off together. The fairly weak bond between the silver and the phosphor glass beneath it allowed the coating to release in microscopic chunks with relatively little pressure from the corner of the razor blade. This, along with the inherent hardness of the phosphor glass layer, ensured that the glass was not damaged by the razor blade. The profiles of the coating showed a relatively smooth phosphor-glass surface at the bottom of the trough created by the razor. The depth of the silicon film was then determined by subtracting from the profilometer measurement the previously-measured thickness of the silver film. The silver film thickness was not measured as thoroughly as the silicon film since the measurement technique was destructive. However, the silver deposition technique was well characterized, so the variation of the silver thickness over the wafer was predictable, as discussed above. The thickness of the silver film was deliberately kept to a minimum so that the expected 20% variation would result in only a small uncertainty in the silicon coating thickness. The uncertainty in the silver film thickness was $\pm 0.03 \mu\text{m}$.

The uncertainty in the silicon thickness was due primarily to the variation in the silicon film thickness over the surface of the wafer. This variation was probably caused by unevenness in the backside of the substrate. (Uneven contact with the susceptor in the CVD process would cause an uneven deposition rate of the silicon because the rate is strongly temperature dependent.) The variation in the coating thickness (Δt) placed a limit on the increment of coating thickness from

Sample Cross-Section

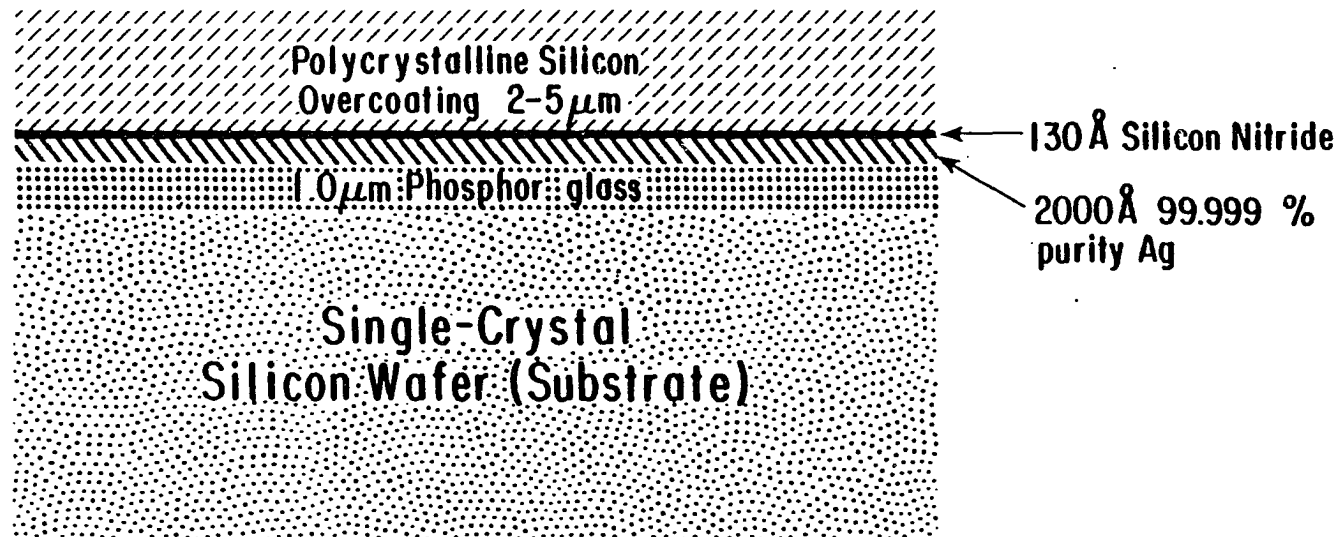


Figure 4.3. A cross-section of a sample, showing all of the layers of the finished waveguide. The silver film is optically thick to the surface plasmon. The thicknesses are not to scale.

wafer to wafer. Preliminary trials indicated that the variation would have behaved as a fixed percentage of the mean coating thickness, so the thickness increments would have had to become larger as the thickness was increased. Table 4.1 (below) is a summary of the statistics for the film thickness of the samples. The thickness was measured every centimeter over the area bounded by the outer edge of the gratings. These measurements were used differently for the two sets of experiments. For the propagation length measurements, the thickness used was the average thickness in the area between the gratings. For the coupling study, the appropriate thickness was the average of 4 measurements on the corners of the grating being studied.

Table 4.1. Statistics for Silicon Overlayer Thickness

Sample No.	11	16	10	17	19	21
Average Thickness (μm)	2.09	3.15	3.65	4.28	4.77	5.13
Standard Deviation (μm)	0.103	0.102	0.145	0.124	0.132	0.190

CHAPTER 5

ATTENUATION MEASUREMENTS

The measurement of the propagation length of the overcoated mode is important in three regards: First, it measures a fundamental property of the mode (the imaginary component of the wavevector, β_i), and can do so without the alteration of mode properties that a grating, or probes near the surface, might cause. Measurements yielding a curve such as Figure 2.6 would support the field equations given by Eqs.(2.32-2.24). Secondly, since the propagation length is almost completely determined by the dielectric constant of the metal, it tests both the applicability of the Drude model to this frequency and the values of the Drude parameters used to predict the dielectric constant. In this experiment, the attenuation measurement was based on Drude parameters measured in the visible and the near-infrared. Finally, the experiment helps to determine if there can be a satisfactory tradeoff between long propagation length (a characteristic of thin overlayers), and the improved localization of the mode (a characteristic of thick overlayers). The determination of this tradeoff is critical for any potential technological applications.

The surface plasmon has the same fundamental characteristics in the presence of an overcoating (for $t \ll \lambda$) as without: the field decays exponentially into the silver and into the air above the sample, remaining essentially constant across the silicon film. However, the presence of the film perturbs the real part of the surface plasmon wavevector (β_r), on the order of a few percent, to larger values (i.e. away from the light line). Though the change in β_r is small, the effect is to dramatically

collapse the field in the air down to the metal surface. The field amplitude at the surface is concurrently enhanced, increasing the fraction of the mode's energy contained in the lossy metal. Since this effect can result from an overlayer only a few microns thick, the percentage of energy in the film is extremely small; moreover, the silicon film is a relatively low-loss material ($n_i = 0.0005$) (Loewenstein, Smith and Morgan, 1973; Passchier, Honijk, Mandel and Afsar, 1977), but since the metal is extremely lossy ($n_i \cong 500$ based on Drude model), the change in β_r caused by the film is accompanied by an increase in the attenuation of the wave. It is the measurement this attenuation, as a function of overlayer thickness, which is the purpose of this experiment.

Experimental Method

The technique used for this experiment relies on the reproducibility of the gratings in coupling and decoupling the radiation. Referring to Figure 4.1, the laser beam is to be coupled to the surface plasmon via each of the five input gratings on the sample. The coupling process, discussed in detail in the next chapter, is eliminated from the measurement if it is identical at each grating. For each of the five input gratings on a given sample, the relevant parameters (angle of incidence and position of beam on grating) were adjusted so as to maximize the coupling efficiency. Assuming identical coupling efficiencies for each waveguide on a given sample, the throughput obeys the following relationship

$$\log(I_{out}) = -\alpha \cdot L + \log(I_{in} \cdot \eta_{in} \cdot \eta_{out}) , \quad (5.1)$$

with I representing intensity, η representing coupling efficiencies, and the attenuation constant $\alpha = 2\beta_i$. As a function of L , this equation describes a straight line with a slope of $-\alpha$, and therefore the measurement of α depends only upon the difference in

path length ΔL of one waveguide compared to another. To determine the attenuation constant, the throughput of each path on the sample was measured and plotted (on a semi-log scale) against the path length. (An example is shown in Figure 5.1, giving the data for the $3.6\mu\text{m}$ -thick overcoating. Due to damage, only the upper three paths on this sample were usable.) The slope of the line was determined by a least-squares fit. A second set of data on each sample was obtained by reversing the direction of propagation (by rotating the waveguide 180°); this compensated for thickness variations in the direction of propagation.

The dotted lines in Figure 5.1 show how the error bars were determined: the maximum and minimum slope gives the upper and lower bounds on α . Note that forward and reversed measurements constitute separate data sets. In determining the errors, it was important to distinguish between the two sets of data taken on each sample. Since they were taken at different times, changes in the ratiometer (see Chapter 3) would change the throughput by a constant amount. Therefore, the maximum and minimum slopes were determined by points within a single set. However, such variations in the "d.c." bias do not affect the fit of a single straight line to the set of all the data points, so the determination of the mean value of α was made from the entire set for each sample.

Results & Discussion

Figure 5.2 is a plot of all the measured absorption coefficients versus the average film thickness for the six samples studied. The error bars indicate the uncertainty in the absorption coefficient for a particular film, and the theoretical prediction, based on Eqs.(2.32-2.34) and the Drude theory, is shown as a solid line.

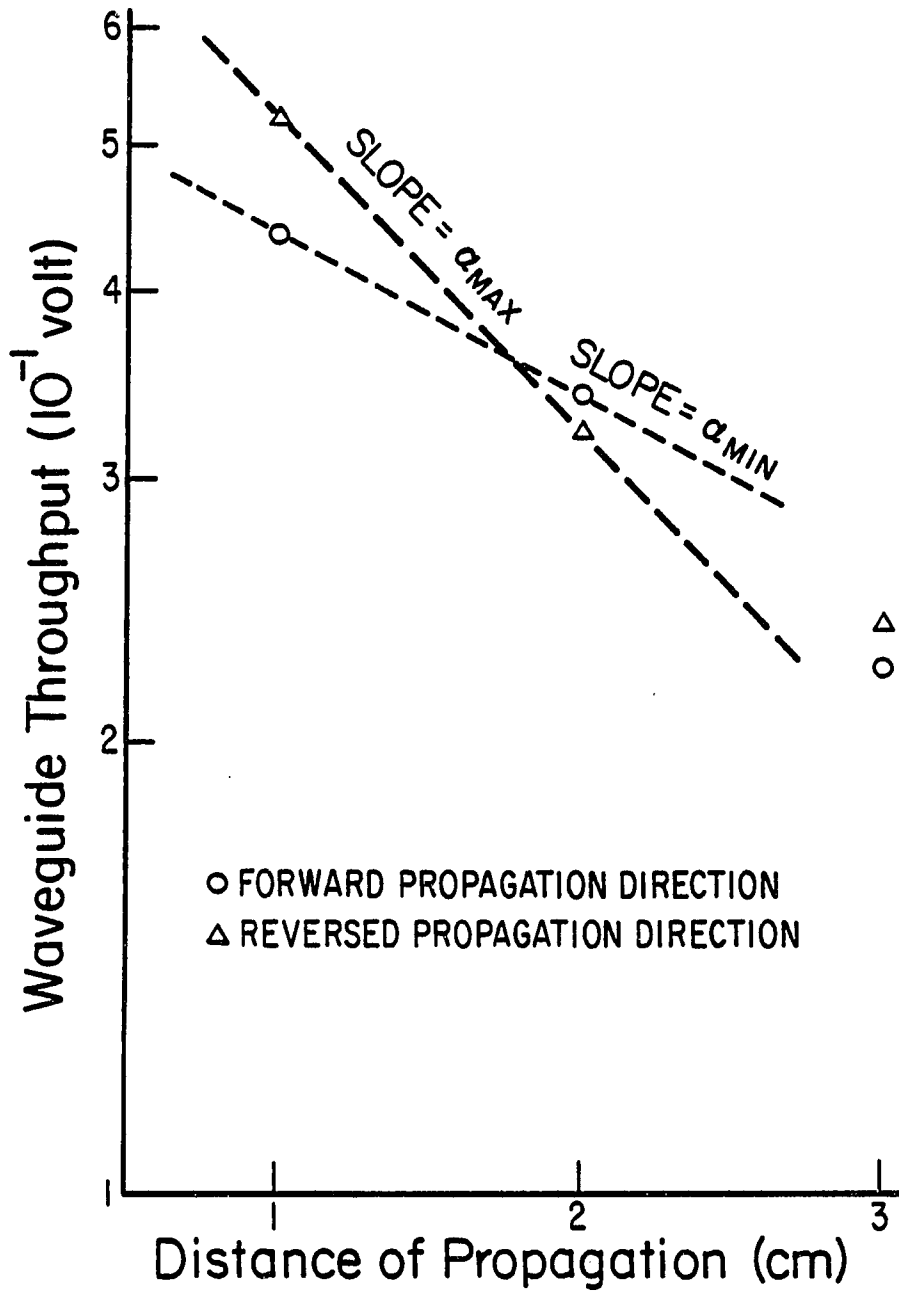


Fig 5.1. Throughput measurements plotted on a semi-log scale against waveguide length. The signal in volts is proportional to the power transmitted by the waveguide. The limits on the experimental error are shown by the dotted lines. This data is for a film thickness of $3.6 \mu\text{m}$ (Sample 10).

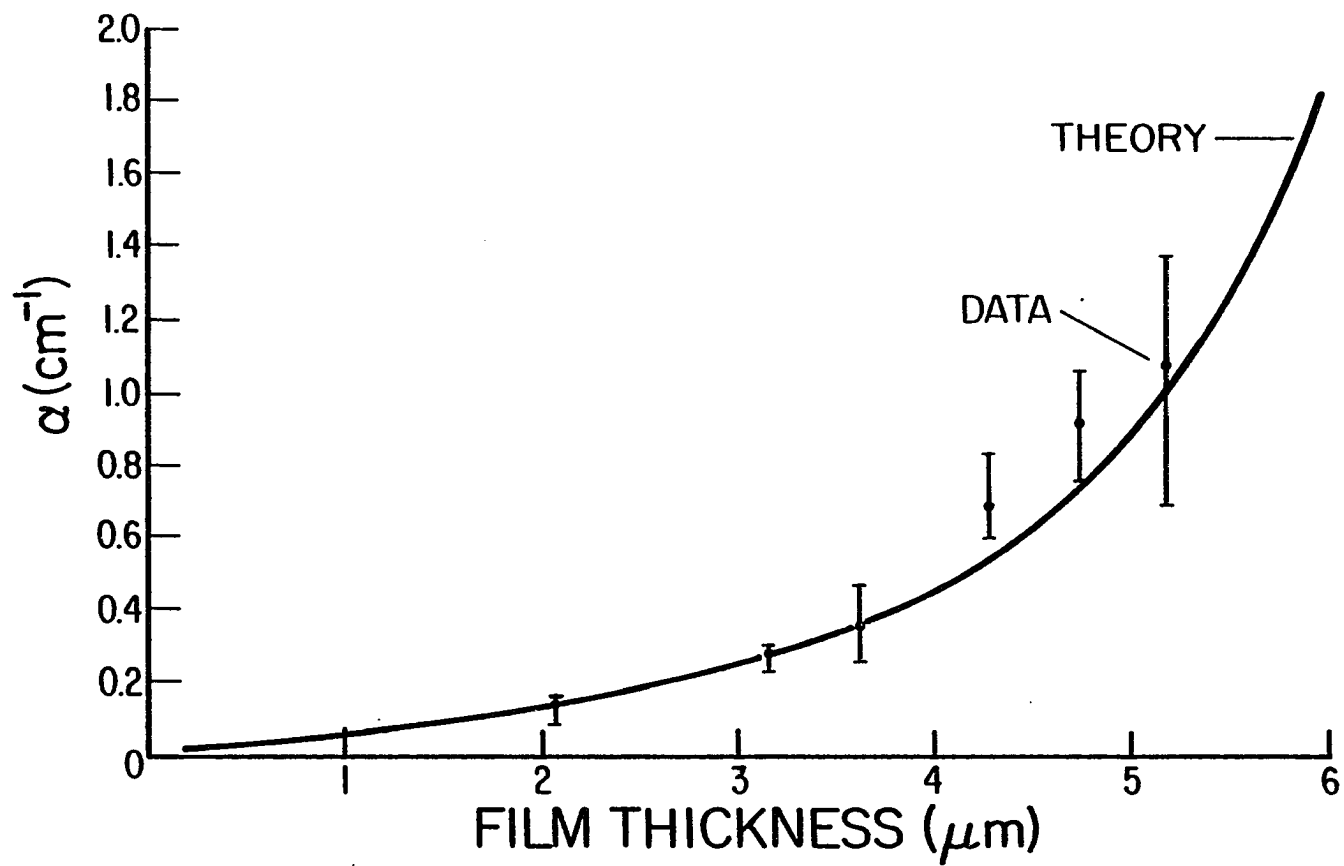


Fig 5.2. Measured absorption coefficient of the overcoated surface plasmon mode plotted against the overcoat thickness. Theoretical curve is based on the Drude model for the metal dielectric function.

The theoretical curve is determined primarily by the dielectric constants of the metal and silicon. Since the properties of silicon are well known, the predicted absorption coefficient hinges on the choice of the plasma resonance frequency ω_p and the free-carrier lifetime τ , for silver. These parameters have been measured in the wavelength range from the ultraviolet up to approximately 30 μm , but not at as long a wavelength as we are using (Ordal, Long, Bell, Bell, Alexander and Ward, 1983). Presently the accepted values for the Drude parameters for silver are $\omega_p = 1.38 \pm 0.03 \times 10^{16} \text{ s}^{-1}$ and $\tau = 3.1 \pm 1.2 \times 10^{-14} \text{ s}$ (Johnson and Christy, 1972). (A more recent value is $\omega_p = 1.37 \times 10^{16} \text{ s}^{-1}$ and $\tau = 3.7 \times 10^{-14} \text{ s}$, reported without associated uncertainties (Ordal, Bell, Alexander, Long and Querry, 1985).) The free-carrier lifetime was chosen as the adjustable parameter rather than the plasma frequency because the theoretical curve did not change appreciably across the range of uncertainty in ω_p . By comparison, the effect of changes in τ was relatively dramatic. By reducing τ to $2.3 \times 10^{-14} \text{ s}$ we produced a good qualitative fit to the experimental data, with an estimated error in τ of $\pm 0.6 \times 10^{-14} \text{ s}$.

These results are in excellent agreement with accepted values of ω_p and τ , albeit at the limits of the uncertainty in τ , confirming that the Drude model is applicable without significant modification even at these long wavelengths. The Drude theory predicts that attenuation increases as τ decreases, hence the lower value of τ used to fit our data.

The increased attenuation is consistent with defects in the film, which cause scattering. The scattering losses in the film cannot be separated from absorptive losses, so that in general the error in the measured absorption introduced by film defects is always toward higher absorption. Despite the high quality of the silicon

films on the samples, this is the most likely reason that the absorption was higher than expected. The quality of the silicon eliminates another candidate for the increased absorption, which is the absorption coefficient of the silicon itself. In fact, α is relatively insensitive to that parameter, because the film is so thin. In order to fit the data with $\tau = 3.1 \times 10^{-14}$ s, it is necessary to assume an overlayer absorption coefficient approximately 30x greater than the known value for silicon. This is unreasonable given the quality of the process, materials and equipment that was used for the deposition of the coating.

The thin layer of silicon nitride is not expected to affect the measured attenuation. In general it would have had the same effect as raising the loss coefficient of the silicon, but since it was less than 1% of the thickness of the silicon, that effect was negligible. The same argument applies to the 10-50 Å metal-oxide layer which undoubtedly existed at the surface of the silver.

It should be emphasized that the Drude parameters have not been measured uniquely in this experiment. The value of ω_p could have been adjusted while holding τ constant, and an equally good fit would have been obtainable. However that would have required an adjustment to $\omega_p = 1.1 \times 10^{16} \text{ s}^{-1}$. Because this value is well below the accepted limits for ω_p , the solution was rejected. To make a unique measurement of the Drude parameters requires at least the additional measurement of the low-frequency conductivity of the silver film, which is determined by the relationship (Ordal et.al., 1985)

$$\sigma_0(\text{cm}^{-1}) = \frac{\omega_p^2 \tau}{8\pi^2 c} \quad (5.2)$$

this can be expressed in terms of the d.c. resistivity in $\Omega \cdot \text{cm}$ by

$$\rho_0(\Omega \cdot \text{cm}) = \frac{9 \times 10^{11}}{2\pi c \sigma_0(\text{cm}^{-1})} \quad (5.3)$$

It was not possible to measure the low-frequency conductivity of the silver films on the samples because of the presence of the dielectric overlayer.

The error bars in Figure 5.2, which increase in size with film thickness, are due to the variations in the film thickness described in Chapter 4, and in fact they roughly follow the standard deviations given in Table 4.1. The specific attribute which primarily causes the error is the variation in the thickness from one path to another. The variation along the propagation direction is compensated by making the measurement in two directions. The variation perpendicular to the propagation direction has the effect of changing α , when it is assumed constant. A secondary effect is the change in coupling efficiency that the thickness variations cause. This is not as important as the change in α , because the throughput of the waveguide will change proportionally to the change in coupling efficiency, while it will change exponentially with changes in α .

The various effects that have been discussed that may introduce systematic errors do not obscure the fact that the accepted numerical values for material parameters very closely predict the attenuations lengths that were measured. The measured values of α , which fit well to the value for τ that we used, were only about 25% higher than the expected values. This confirms that the Drude model and the equations describing the overcoated mode form a solid theoretical foundation upon which other properties can be predicted.

CHAPTER 6

COUPLING STUDY

A central issue in the technological usefulness of the far-infrared surface plasmon is the efficiency with which it can be generated. The first experimental studies of the overcoated surface plasmon mode (Seymour, Krupczak Jr. and Stegeman, 1984) demonstrated that high efficiency coupling to the overcoated mode could be achieved with grating couplers. Those experiments also revealed that the grating modifies the modal fields and/or the dispersion relations for the surface plasmon. In this chapter, a series of measurements are discussed which experimentally determined the fundamental coupling parameters of the gratings as a function of the overlayer thickness. The experiment was designed in such a way that all parameters in the coupling process were either measured or eliminated, so that in contrast to the previous grating study (Seymour, Krupczak Jr. and Stegeman, 1984), no assumptions needed to be made about the incident beam or the absorption (β_1) in the grating region.

The efficiency of a grating in coupling the incident beam to the surface plasmon is a function of many factors, of which the most complex are the grating shape and depth. Though it is beyond the scope of this dissertation to treat them exactly, the shape and depth dependence were eliminated from the experiment by the fact that all the gratings were identical; this, along with the fixed incident beam shape, insured that the only variable in the coupling process was the overlayer thickness. The measured parameters, i.e. the characteristic coupling length (L_c) and

the absorption of the surface plasmon in the grating region (β_1), are the only quantities needed to calculate the maximum coupling efficiency of the grating for a given incident beam. The present calculations are based on a generalized coupled-mode theory (Ulrich, 1973) in which a value for the parameter L_c is assumed, and hence does not specify the physical process which causes the coupling. The theory utilizes additional inputs such as the size of the interaction region and the incident beam shape in the determination of the coupling efficiency.

An precise treatment of the variables that affect the coupling process, leading to an exact prediction of the coupling constant and absorption, is not feasible for this dissertation. We can, however, apply an approximate (perturbative) grating theory, which in fact is generally considered accurate in the limit in which the grating corrugation is small compared to the wavelength. In this type of theory, the normal modes for an uncorrugated waveguide are assumed valid in a corrugated region, and the corrugation is treated either as a perturbation of the dielectric constants in which the fields exist (Yariv, 1973; Marcuse, 1974) or as a perturbation in the boundary conditions at the corrugation (Normandin, So, Rowell and Stegeman, 1981). The former technique is known as "Perturbation Theory." The latter is known as the "Total Fields" method, and is the technique that will be used for this theory section. From this theory the coupling constant and the absorption can be calculated (though as a result of the approximations, the absorption in the grating region is determined directly from the unperturbed modal field equations (2.32-2.40)). Coupled-mode theory is then used to calculate the growth of the new normal mode fields generated by scattering from the corrugation. The advantage of the total field analysis is that it explicitly requires approximations that are part of, but not explicit in, other

perturbative theories. One of these approximations is severely violated in the present application; therefore, in the event of poor agreement between the theory and the data, the "total fields" theory will clearly identify a potential source for the failure.

Coupled-Mode Theory

It is well known (Kapany and Burke, 1972) that a prism of suitably high index can be used to launch guided waves in thin films. This coupling technique uses the fact that energy crosses an interface even under the conditions of total internal reflection, in the form of an evanescent field. This field can penetrate into a waveguide if the prism is placed over the guide with a small gap separating the two. The field may couple to the allowed propagation modes of the guide when the spatial periodicity of the field along the prism base is matched to that of the guided wave. From a kinematic point of view, the prism increases the k -vector over the vacuum value by virtue of its index of refraction, so that the conservation of momentum may be satisfied in the interaction between the driving field (in the prism) and the propagation modes of the guide.

A grating can also increase the k -vector of an incident wave, by way of the periodic modulation of the medium which re-radiates the incident light. If one creates such a modulation on the waveguide, the incident beam may couple to a guided-wave mode via a diffracted order because the k -vector of the incident beam is augmented by some multiple of grating periodicity. We utilize the same geometry as in Figure 2.1, with the grating grooves parallel to the y -axis and an incident beam from the upper medium ($z < 0$). The appropriate equation for this interaction is the well-known grating equation

$$k_x^d = k_x^i + p\kappa \quad (6.1)$$

$$\kappa = \frac{2\pi}{T} \quad (6.2)$$

where k_x^d is the x-component of the diffracted order, p is any positive or negative integer allowed by the Fourier components of the grating profile and T is the grating period. A resonance may occur when k_x^d is equal to some β of the guide just as in the prism coupler. Equation (6.1) describes the diffracted vector components in the plane of the grating; the k-vector perpendicular to the grating obeys the relation

$$k_z^d = -\sqrt{n_g^2 k_0^2 - k_x^d{}^2} \quad (6.3)$$

where n_g is the index of the guide, and we are assuming henceforth a reflecting substrate. Eq.(6.3) is not directly involved in the coupling process. (It does, however, enter into the Fresnel relations, which determine the strength of the diffracted orders.) Note that for $k_x^d > k_0$, the diffracted field is evanescent in the medium of the incident wave. This is true whenever the grating is coupling to a propagation mode of the guide, just as it is for the field in the gap between a prism coupler and the guide.

The incident k-vector is variable by way of the incident angle

$$k_x^i = k_0 \sin\theta_i \quad (\theta_i = \text{angle of incidence}) \quad (6.4)$$

so that even with a fixed grating periodicity, the coupling to a guided mode can be tuned.

In-coupling

The coupled-mode formalism assumes three parameters, the coupling length L_c , the "resistive" absorption in the grating β_1 , and the wavevector mismatch Δk

between the k -vector of the driving field and the propagation vector of the guide. The first term is determined by properties specific to the grating, such as the shape and depth of the grooves. The second term is largely a material property, but it can be increased by the presence of the corrugation. For this section, knowledge of their values will be assumed. It is the purpose of this section to show that they can be determined experimentally. The determination of Δk is a function of the incident angle, the periodicity of the grating and the propagation wavevector of the guided wave, as given by Eqs.(6.1-6.4). Assuming a reflecting substrate, the appropriate differential equation for V_1 , the guided-wave field amplitude, is (R. Ulrich, 1973):

$$\frac{\partial V_1(x)}{\partial x} + \left[\frac{1}{L_c} + \beta_I \right] V_1(x) = \sqrt{\frac{2}{L_c}} \cdot V_3(x) \cdot \exp[i(k_x^d - \beta)x] , \quad (6.5)$$

where β_I is the absorption coefficient, L_c is the characteristic coupling length, and V_3 is the amplitude of the incident field. Note that in the absence of a driving field ($V_3=0$), the solution to Eq.(6.5) is the exponential decay of the guided wave field with a rate

$$\Gamma = \frac{1}{L_c} + \beta_I . \quad (6.6)$$

If β_I is regarded as a loss coefficient, then the symmetry of β_I and L_c^{-1} means that L_c^{-1} must be regarded as a loss term, as well. In fact it represents radiative loss, which can occur via the grating-induced subtraction of κ from the wavevector of the guided wave. This effect stems mathematically in Eq.(6.1) from the fact that the equation is symmetrical with respect to κ since the integer n may be positive or negative. In physical terms, the phase-matching condition which allows coupling is the same as that for de-coupling. The parameter L_c is the 1/e distance describing

the decay of the surface plasmon fields, in the absence of absorption. The decoupling process automatically satisfies the condition ($k_x^d - \beta = 0$), thus defining the direction of the re-radiation.

The preceding discussion assumes no boundaries to the grating. The coupling of a finite beam in an infinite grating will not result in the net transfer of energy to the guided wave, since beyond the incident beam the energy will eventually radiate out (neglecting the absorption due to the surface plasmon loss term β_1). Therefore the coupling of the modes must be terminated after some energy has been transferred to the guided wave. This is accomplished by terminating the interaction region. Assuming that the interaction ends abruptly at $x = x'$, the differential expression Eq.(6.5) may be integrated from $-\infty$ to x' to give the value of V_1 as a function of x' in the grating. Figure 6.1 shows $V_1(x')$ for different values of L_c , assuming $\beta_1 = 0$, with L_c expressed as a multiple of the width of the gaussian incident beam. The coupling reaches a peak and declines because the exponential radiative decay dominates the growth of the guided wave after the guided wave field exceeds a certain value. This limits the efficiency of the one-dimensional lossless distributed coupler to approximately 80.1% (Ulrich, 1970).

Although the curves in Figure 6.1 are for a gaussian input beam, the profile need not be gaussian, and the appropriate calculations for our experiments were performed using actual beam profiles. The complete calculation was done in two dimensions, as an uncoupled sum of one-dimensional profiles. Profiles of the beam at the input coupler were measured using a "point" detector (0.25 mm diameter), digitizing a high density of points along the x-axis. A total of 15 such profiles were made in the y-direction, resulting in a 180x15-point 2-dimensional beam profile.

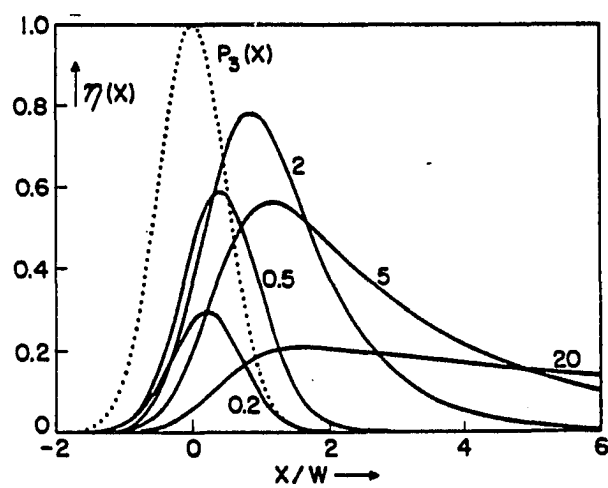


Figure 6.1. Guided-wave field amplitude in coupling region. $P_3(x)$ represents an incident gaussian beam, of width $2W$, centered on an arbitrary zero in an unbounded coupling region. The amplitude decays past the input beam because of re-radiation. The parameter of the curves is the ratio L_c/W . The optimum coupling efficiency is attained with a coupling length approximately $3/4$ of the beam diameter, and by terminating the interaction region at a position approximately $1/2$ a beam diameter past the center of the beam. (From Ulrich, 1973.)

The total power in the beam was determined from the profile, by a rectangular approximation in the x-direction and a Simpson's Rule approximation in the y-direction. The integration of Eq.(6.5), the guided wave field, was calculated similarly.

Out-coupling

It was noted earlier that in the absence of the incident field, the guided wave decays exponentially with a decay constant Γ due to radiative and non-radiative loss. The numerical solution performed on a computer is still applicable here; however the integral of Eq.(6.5) can in this case be cast in a closed-form solution:

$$V_1(x) = V_0 \exp[-\Gamma x] \quad (6.7)$$

where Γ is given by Eq.(6.6). This equation logically applies to the output coupler, in which the only incident wave is the guided wave, and it describes radiative decay into a bulk wave (as well as absorption). To see how the decoupled beam grows from the guided wave, we use the following differential equation:

$$\frac{\partial V_{\text{rad}}(x)}{\partial x} = \frac{1}{L_c} V_1(x) \quad (6.8)$$

and substituting (6.7) we have

$$\frac{\partial V_{\text{rad}}(x)}{\partial x} = \left[\frac{V_0}{L_c} \right] \exp(-\Gamma x) . \quad (6.9)$$

This equation is easily integrable across the interaction region to give the total radiated power, but it is perhaps more interesting in this form from an experimental point of view. (We do not need to be concerned here with phase-matching, as the radiated wave will automatically propagate in the direction for which $\Delta k=0$.) This

equation describes the radiative field amplitude as a function of position on the output grating, which can be measured (in intensity) by a point detector scanning along the output grating. This is a valuable measurement because of the exponential decay with rate Γ ; the log of this expression is a straight line with a slope proportional to Γ . Thus by eliminating one coupling process (in-coupling), we can experimentally determine the sum of L_c^{-1} and β_I .

Previously we found that the choice of a value for β_I and for L_c^{-1} defined a curve in Figure 6.1. Taking loss into account, the calculation may be modified to predict a (experimentally observable) dip in the 0-order reflection from the grating due to coupling to the guided wave. However, the minimum in the dip, corresponding to the maximum value of the curves in Figure 6.1, does not uniquely define L_c and β_I . The additional information needed to uniquely define the parameters is contained in the measurement of Γ . Therefore the combination of both in-coupling and out-coupling measurements is essential to determine both L_c and β_I .

For a comparison between experiment and theory we must predict L_c , and to do this is manageable only in a perturbative approximation. The perturbative solution assumes that the presence of the grating does not alter the guided wave fields as normal modes of the guide. The interface itself is predefined to follow the shape of the grooves (as it actually does). As in the coupled-mode theory, we ignore the y -direction (assuming infinite extent), but in contrast to the primarily one-dimensional nature of that formalism, here we must retain the z -dependence of the fields.

Grating Theory

The "total field analysis" technique has been discussed in a series of four papers (Normandin, So, Rowell, and Stegeman, 1979; So, Normandin and Stegeman, 1979; Sipe and Stegeman, 1979; Stegeman, Sarid, Burke and Hall, 1981). The method seeks to solve the polarization-induced generation of optical waves by determining, to first order, the complete electric fields inside and outside of the polarization region. This is in contrast to normal mode analysis, in which the polarization source is expanded in terms of the normal modes of the system. As mentioned before, perturbative grating theories are normally assumed to be valid in the limit $\delta_0\beta \ll 1$, where δ_0 is the amplitude of the corrugation. The total field analysis explicitly introduces that approximation, but also explicitly requires the corresponding approximation for the transverse wavevectors α_1 , α_2 , and α_3 ; e.g. that $\delta_0\alpha_3 \ll 1$, where the field penetration depth into the metal is $1/\alpha_3$. For thin film or integrated optics at optical frequencies, this condition is always satisfied since the field penetration depth is approximately equal to the inverse of the wavevector. For a metal in the far infrared this condition is not satisfied. Also, the perturbative approach does not account for the actual grating profile; because it is a first-order theory, only the fundamental in a harmonic decomposition of the grating profile is used. The higher harmonic grating orders may in reality provide additional contributions to the fields being calculated in this analysis, but those contributions are of second or higher order. These approximations will have a large bearing on the comparison between experiment and theory.

A general overview of the technique is as follows: The guided wave field is taken to be normally incident on the corrugation region, with a corrugation occurring

at either or both of the interfaces of Figure 2.3, extending from $x=0$ to $x=L$. (In the case of these experiments, both interfaces are corrugated, with the same amplitude.) The incident fields satisfy all the electromagnetic boundary conditions at the unperturbed (uncorrugated) interfaces, and so fulfill the requirements for the 0th-order solution to the total field in the grating region. This means that the form of the normal-mode field(s) in the grating are identical to the normal-mode fields in the uncorrugated region, Eqs. (2.32-2.40). (This can be proven rigorously by matching boundary conditions across the transverse grating interface, i.e. the yz -plane at $x=0$ and $x=L$, where there are in fact no material discontinuities.) To develop the first-order solution to the fields in the grating region, the normal-mode fields are evaluated in the local coordinate system of the corrugated surface, and it is found that the tangential field components (E_x and H_y) are not continuous across the boundary. This occurs in the case of E_x because the tangent to the corrugated surface is in general not parallel to the x -axis, and therefore the fields along the tangent contain a small portion of the z -dependence of the normal mode. The discontinuity in H_y results from an analogous admixture of field components along the z' -axis that causes a discontinuity in D_z . Because the complete solution must obey the boundary conditions (i.e. continuous tangential E and H fields), additional fields, which include the scattered fields, are needed. The scattered field amplitudes are calculated to first order; i.e. they are formed so as to cancel the first-order discontinuity of the incident fields. These fields are characterized by a wavevector $\beta' = \beta \pm \kappa$, and the solutions can be restricted to $+\kappa$ or $-\kappa$ by the assumption that for either case, the other scattered wavevector will be far from phase-matched with any normal mode. In the case of the surface plasmon, there are are no other waveguide

modes (save for backscattering, eliminated by the choice of grating periodicity). The only phase-matching that can occur in this case is to a radiative mode, which simplifies the analysis; the normal component of the Poynting vector of the scattered field gives the rate at which energy is radiated away from the grating, which is simply related to the parameter L_c . The absorptive loss term β_1 which must be included in the coupled-mode analysis is a property of the 0th-order solution in the grating region, and is therefore determined by Eqs. (2.32-2.34).

In the present case, the grating region is comprised of two corrugated interfaces since the coating follows the corrugated surface of the substrate. In this situation, we calculate scattered fields due to each corrugation separately, using the method outlined above, and sum the amplitudes prior to relating the result to a total coupling coefficient L_c . The analysis will be presented as follows: First, we perform the analysis for a corrugation at the n_2 - n_1 (air-film) interface. Nearly all the steps will be shown explicitly, including the determination of a coupling constant due solely to scattering from this corrugation. Then corresponding analysis for the corrugation at the metal-film interface will be performed. Since the procedure is identical, only important results will be explicitly shown, and the final coupling constant L_c will be given explicitly.

Upper Corrugation

In the upper medium (n_1), the incident field is given by

$$\text{air:} \quad \vec{H} = \hat{y} C_{TM} \exp [i(\omega t - \beta x) + \alpha_1(z+h)] , \quad (z < -h) \quad (2.32a)$$

and with

$$E_x = \frac{i}{\omega \epsilon_0 n^2} \frac{\partial H_y}{\partial z} \quad (6.10)$$

and

$$E_z = -\frac{i}{\omega\epsilon_0 n^2} \frac{\partial H_y}{\partial x}, \quad (6.11)$$

$$E_x = \frac{i\alpha_1}{\omega\epsilon_0 n_1^2} C_{TM} \exp[i(\omega t - \beta x) + \alpha_1(z+h)], \quad (6.12)$$

$$E_z = -\frac{\beta}{\omega\epsilon_0 n_1^2} C_{TM} \exp[i(\omega t - \beta x) + \alpha_1(z+h)] \quad (6.13)$$

with C_{TM} given by Eqs.(2.39) and (2.40).

The transformation of vector components in the x-y-z coordinate system (associated with a flat interface) into a local coordinate system which is associated with the corrugated interface is given by the following relationships (Stegeman, Sarid, Burke and Hall, 1981):

$$R_{x'} = R_x \cos\psi + R_z \sin\psi \quad (6.14a)$$

$$R_{y'} = R_y \quad (6.14b)$$

$$R_{z'} = -R_x \sin\psi + R_z \cos\psi \quad (6.14c)$$

where ψ is the local tilt of the x'-y'-z' axes relative to the x-y-z coordinate system.

In this case, with the corrugation of the interface represented as

$$z = -h + \delta_0 \cos(qx), \quad (6.15)$$

the local tilt is given by

$$\tan\psi = \frac{\partial u_z}{\partial x} = -\delta_0 \kappa \sin(\kappa x). \quad (6.16)$$

In the present analysis, the product $\delta_0 \kappa$ is assumed to be small, so that $\cos\psi \cong 1$, $\sin\psi \cong -\delta_0 \kappa \sin(\kappa x)$, and the transformed tangential fields are:

$$E_{x'} = E_x - (\delta_0 \kappa) \sin(\kappa x) E_z, \quad (6.17a)$$

$$H_{y'} = H_y. \quad (6.17b)$$

Substituting Eqs. (6.12) and (6.13),

$$E_{x',\text{air}} \Big|_{\text{u}} = \left[\frac{i\alpha_1 + \beta\delta_0\kappa\sin(\kappa x)}{\omega\epsilon_0 n_1^2} \right] C_{\text{TM}} \exp[i(\omega t - \beta x) + \alpha_1 z] \Big|_{z=-h + \delta_0 \cos(\kappa x)}$$

$$H_{y',\text{air}} \Big|_{\text{u}} = C_{\text{TM}} \exp[i(\omega t - \beta x) + \alpha_1 z] \Big|_{z=-h + \delta_0 \cos(\kappa x)} \quad (6.18)$$

In the film (n_2),

$$H_{y,\text{film}} = C_{\text{TM}} \exp[i(\omega t - \beta x)] \left[A_+ e^{i\alpha_2 z} + A_- e^{-i\alpha_2 z} \right], \quad (2.33a)$$

$$E_{x,\text{film}} = -\frac{\alpha_2}{\omega\epsilon_0 n_2^2} C_{\text{TM}} \exp[i(\omega t - \beta x)] \left[A_+ e^{i\alpha_2 z} - A_- e^{-i\alpha_2 z} \right],$$

$$E_z = -\frac{\beta}{\omega\epsilon_0 n_2^2} C_{\text{TM}} \exp[i(\omega t - \beta x)] \left[A_+ e^{i\alpha_2 z} + A_- e^{-i\alpha_2 z} \right], \quad (6.19)$$

so the transformed tangential fields are:

$$E_{x',\text{film}} \Big|_{\text{u}} = C_{\text{TM}} \exp[i(\omega t - \beta x)]$$

$$\times \left[\frac{\alpha_2}{\omega\epsilon_0 n_2^2} \left[A_- e^{-i\alpha_2 z} - A_+ e^{i\alpha_2 z} \right] + \frac{\beta\kappa\delta_0}{\omega\epsilon_0 n_2^2} \sin(\kappa x) \left[A_- e^{-i\alpha_2 z} + A_+ e^{i\alpha_2 z} \right] \right] \Big|_{z=-h + \delta_0 \cos(\kappa x)}$$

$$H_{y',\text{film}} \Big|_{\text{u}} = C_{\text{TM}} \exp[i(\omega t - \beta x)] \left[A_+ e^{i\alpha_2 z} + A_- e^{-i\alpha_2 z} \right] \Big|_{z=-h + \delta_0 \cos(\kappa x)} \quad (6.20)$$

with A_+ and A_- given in Eqs. (2.35) and (2.36).

Now the fields in the air will be evaluated along the corrugated interface, given by Eq. (6.15), and simplified.

$$\begin{aligned}
E_{x',\text{air}} \Big|_{\text{u}} &= \frac{C_{\text{TM}}}{\omega \epsilon_0} \exp[i(\omega t - \beta x)] \left[\frac{i\alpha_1}{n_1^2} \exp[\alpha_1 \delta_0 \cos(\kappa x)] + \frac{\beta \delta_0 \kappa}{n_1^2} \sin(\kappa x) \exp[\alpha_1 \delta_0 \cos(\kappa x)] \right] \\
H_{y',\text{air}} \Big|_{\text{u}} &= C_{\text{TM}} \exp[i(\omega t - \beta x)] \exp[\alpha_1 \delta_0 \cos(\kappa x)]
\end{aligned} \tag{6.21}$$

The terms $\exp[\alpha_1 \delta_0 \cos(\kappa x)]$ may be expanded in a Bessel's series, for which the first-order approximation is given by

$$\exp[\alpha_1 \delta_0 \cos(\kappa x)] \cong 1 + \alpha_1 \delta_0 \cos(\kappa x). \tag{6.22}$$

Substituting Eq.(6.22) into Eqs.(6.21), and dropping terms in δ_0^2 ,

$$\begin{aligned}
E_{x',\text{air}} \Big|_{\text{u}} &= \frac{C_{\text{TM}}}{\omega \epsilon_0} \exp[i(\omega t - \beta x)] \left[\frac{i\alpha_1}{n_1^2} + \frac{i\alpha_1^2 \delta_0}{n_1^2} \cos(\kappa x) \right] + \frac{\beta \delta_0 \kappa}{\omega \epsilon_1} \sin(\kappa x) , \\
H_{y',\text{air}} \Big|_{\text{u}} &= C_{\text{TM}} \exp[i(\omega t - \beta x)] [1 + \alpha_1 \delta_0 \cos(\kappa x)] .
\end{aligned} \tag{6.23}$$

At this point, the introduction of an aforementioned assumption will simplify the expressions. The harmonic terms in (6.23) may be rewritten in exponential form, and can be absorbed into the propagation term by the substitution $\beta' = \beta \pm \kappa$. It may be assumed that only one of these solutions will be phase-matched to a normal mode of the system for a given geometry. As a result, the nonphase-matched term will not couple energy away from the incident mode, and it can be neglected. Choosing the solution $\beta' = \beta - \kappa$, and dropping terms in $e^{-i\kappa x}$, the equations take the following form:

$$E_{x',\text{air}} \Big|_{\text{u}} = \frac{C_{\text{TM}}}{\omega \epsilon_0} \exp[i(\omega t - \beta x)] \left[\frac{i\alpha_1}{n_1^2} + \frac{i\alpha_1^2 \delta_0}{2n_1^2} e^{i\kappa x} - \frac{i\beta \delta_0 \kappa}{2n_1^2} e^{i\kappa x} \right] ,$$

and using Eq.(2.32b) to substitute for α_1^2 ,

$$\begin{aligned}
E_{x',\text{air}} \Big|_{\text{u}} &= iC_{\text{TM}} \frac{\alpha_1}{\omega\epsilon_0 n_1^2} \exp[i(\omega t - \beta x)] \\
&+ \frac{i\delta_0 C_{\text{TM}}}{2\omega\epsilon_0} \exp[i(\omega t - \beta' x)] \left[\frac{\beta\beta'}{n_1^2} - k_0^2 \right] . \\
H_{y',\text{air}} \Big|_{\text{u}} &= C_{\text{TM}} \exp[i(\omega t - \beta x)] + C_{\text{TM}} \frac{\alpha_1 \delta_0}{2} \exp[i(\omega t - \beta' x)] . \tag{6.24}
\end{aligned}$$

The first term in Eqs.(6.24) represents an unperturbed field; we will discover that similar terms on the film side of the interface will cancel them. Returning to the tangential fields on the film side of the interface,

$$\begin{aligned}
E_{x',\text{film}} \Big|_{\text{u}} &= \frac{C_{\text{TM}}}{\omega\epsilon_0} \exp[i(\omega t - \beta x)] \\
&\times [A_- e^{i\alpha_2 h} \exp[-i\alpha_2 \delta_0 \cos(\kappa x)] \left[\frac{\alpha_2}{n_2^2} + \frac{\beta\kappa\delta_0}{n_2^2} \sin(\kappa x) \right] \\
&- A_+ e^{-i\alpha_2 h} \exp[i\alpha_2 \delta_0 \cos(\kappa x)] \left[\frac{\alpha_2}{n_2^2} - \frac{\beta\kappa\delta_0}{n_2^2} \sin(\kappa x) \right]] . \\
H_{y',\text{film}} \Big|_{\text{u}} &= C_{\text{TM}} \exp[i(\omega t - \beta x)] [A_+ e^{-i\alpha_2 h} \exp[i\alpha_2 \delta_0 \cos(\kappa x)] \\
&+ A_- e^{i\alpha_2 h} \exp[-i\alpha_2 \delta_0 \cos(\kappa x)]] . \tag{6.25}
\end{aligned}$$

The approximation $\alpha_2 \delta_0 \ll 1$ allows the use of the first-order expansion of the exponents, and neglecting terms in δ_0^2 .

$$\begin{aligned}
E_{x',\text{film}} \Big|_{\mathbf{u}} &= \frac{C_{\text{TM}}}{\omega \epsilon_0} \exp[i(\omega t - \beta x)] \left[A_- e^{i\alpha_2 h} \frac{\alpha_2}{n_2^2} [1 - i\alpha_2 \delta_0 \cos(\kappa x)] \right. \\
&\quad \left. + A_- e^{i\alpha_2 h} \frac{\beta \kappa \delta_0}{n_2^2} \sin(\kappa x) \right. \\
&\quad \left. - A_+ e^{-i\alpha_2 h} \frac{\alpha_2}{n_2^2} [1 + i\alpha_2 \delta_0 \cos(\kappa x)] - A_+ e^{-i\alpha_2 h} \frac{\beta \kappa \delta_0}{n_2^2} \sin(\kappa x) \right], \\
H_{y',\text{film}} \Big|_{\mathbf{u}} &= C_{\text{TM}} \exp[i(\omega t - \beta x)] \left[A_+ e^{-i\alpha_2 h} [1 + i\alpha_2 \delta_0 \cos(\kappa x)] \right. \\
&\quad \left. + A_- e^{i\alpha_2 h} [1 - i\alpha_2 \delta_0 \cos(\kappa x)] \right]. \tag{6.26}
\end{aligned}$$

Introducing the substitution $\beta' = \beta - \kappa$, dropping terms in $e^{-i\kappa x}$, and substituting Eq.(2.33b) for α_1^2 ,

$$\begin{aligned}
E_{x',\text{film}} \Big|_{\mathbf{u}} &= \frac{\alpha_2 C_{\text{TM}}}{\omega \epsilon_0 n_2^2} \exp[i(\omega t - \beta x)] \left[A_- e^{i\alpha_2 h} - A_+ e^{-i\alpha_2 h} \right] \\
&\quad + \frac{i\delta_0 C_{\text{TM}}}{2\omega_0} \exp[i(\omega t - \beta' x)] \\
&\quad \times \left[A_- e^{i\alpha_2 h} \frac{\beta \beta'}{n_2^2} k_0^2 + A_+ e^{-i\alpha_2 h} (\beta \beta' - k_0^2) \right], \\
H_{y',\text{film}} \Big|_{\mathbf{u}} &= C_{\text{TM}} \exp[i(\omega t - \beta x)] \left[A_+ e^{-i\alpha_2 h} + A_- e^{i\alpha_2 h} \right] \\
&\quad + \frac{i\alpha_2 \delta_0}{2} C_{\text{TM}} \exp[i(\omega t - \beta' x)] \left[A_+ e^{-i\alpha_2 h} - A_- e^{i\alpha_2 h} \right]. \tag{6.27}
\end{aligned}$$

Once again, the first term in the equations represents an unperturbed field.

Subtracting the tangential components at u^- (air side of interface) from the components at u^+ (film side of interface) gives the first-order discontinuities in the incident fields along the upper corrugation:

$$\begin{aligned}
\Delta E_{x'} \Big|_u &= E_{x',\text{film}} \Big|_u - E_{x',\text{air}} \Big|_u \\
&= \frac{\alpha_2 C_{\text{TM}}}{\omega \epsilon_0 n_2^2} \exp[i(\omega t - \beta x)] \left[A_- e^{i\alpha_2 h} - A_+ e^{-i\alpha_2 h} \right] \\
&+ \frac{i\delta_0 C_{\text{TM}}}{2\omega \epsilon_0} \exp[i(\omega t - \beta' x)] \left[\frac{\beta \beta'}{n_2^2} k_0^2 \right] \left[A_- e^{i\alpha_2 h} + A_+ e^{-i\alpha_2 h} \right] \\
&- \frac{i\alpha_1 C_{\text{TM}}}{\omega \epsilon_0 n_1^2} \exp[i(\omega t - \beta x)] - \frac{i\delta_0 C_{\text{TM}}}{2\omega \epsilon_0} \exp[i(\omega t - \beta' x)] \left[\frac{\beta \beta'}{n_1^2} k_0^2 \right] . \\
\Delta H_{y'} \Big|_u &= H_{y',\text{film}} \Big|_u - H_{y',\text{air}} \Big|_u \\
&= C_{\text{TM}} \exp[i(\omega t - \beta x)] \left[A_+ e^{-i\alpha_2 h} + A_- e^{i\alpha_2 h} \right] \\
&+ \frac{i\alpha_2 \delta_0 C_{\text{TM}}}{2} \exp[i(\omega t - \beta' x)] \left[A_+ e^{-i\alpha_2 h} - A_- e^{i\alpha_2 h} \right] \\
&- C_{\text{TM}} \exp[i(\omega t - \beta x)] - \frac{\alpha_1 \delta_0 C_{\text{TM}}}{2} \exp[i(\omega t - \beta' x)] . \tag{6.28}
\end{aligned}$$

Substituting for A_+ , A_- ,

$$\begin{aligned}
\Delta E_{x'} \Big|_u &= C_{\text{TM}} \frac{\alpha_1}{\omega \epsilon_0 n_1^2} \exp[i(\omega t - \beta x)] + \frac{i\delta_0}{2\omega \epsilon_0} C_{\text{TM}} \exp[i(\omega t - \beta' x)] \left[\frac{\beta \beta'}{n_2^2} k_0^2 \right] \\
&- C_{\text{TM}} \frac{\alpha_1}{\omega \epsilon_0 n_1^2} \exp[i(\omega t - \beta x)] - \frac{i\delta_0}{2\omega \epsilon_0} C_{\text{TM}} \exp[i(\omega t - \beta' x)] \left[\frac{\beta \beta'}{n_1^2} k_0^2 \right] ,
\end{aligned}$$

$$\begin{aligned} \Delta H_{y'} \Big|_u &= C_{TM} \exp[i(\omega t - \beta x)] + \frac{\alpha_1 \delta_0 n_2^2}{2n_1^2} C_{TM} \exp[i(\omega t - \beta' x)] \\ &- C_{TM} \exp[i(\omega t - \beta x)] - \frac{\alpha_1 \delta_0 n_2^2}{2} C_{TM} \exp[i(\omega t - \beta' x)] . \end{aligned}$$

As expected, the unperturbed components are continuous across the corrugation, and the calculated first-order discontinuities in the incident fields at the upper corrugation are:

$$\Delta E_{x',u} = \Delta E_u \cdot \exp[i(\omega t - \beta' x)] ,$$

$$\Delta H_{y',u} = \Delta H_u \cdot \exp[i(\omega t - \beta' x)] ,$$

with

$$\Delta E_u = - \frac{i C_{TM} \delta_0 \beta \beta' (n_2^2 - n_1^2)}{2 \omega \epsilon_0 n_1^2 n_2^2} ,$$

and

$$\Delta H_u = \frac{C_{TM} \delta_0 \alpha_1 (n_2^2 - n_1^2)}{2 n_1^2} . \quad (6.29)$$

Solution Fields. Now we propose solution fields whose amplitude will be solved to cancel the discontinuities given by Eqs.(6.29):

air: $\vec{H} = \hat{y} H_1 \exp[i(\omega t - \beta' x) + i \gamma_1 (z+h)]$

$$E_x = - \frac{\gamma_1}{\omega \epsilon_0 n_1^2} H_1 \exp[i(\omega t - \beta' x) + i \gamma_1 (z+h)]$$

$$E_z = - \frac{\beta'}{\omega \epsilon_0 n_1^2} H_1 \exp[i(\omega t - \beta' x) + i \gamma_1 (z+h)] \quad (6.30)$$

film: $\vec{H} = \hat{y} \left[H_+ e^{i \gamma_2 z} + H_- e^{-i \gamma_2 z} \right] \cdot \exp[i(\omega t - \beta' x)]$

$$E_x = - \frac{\gamma_2}{\omega \epsilon_0 n_2^2} \left[H_+ e^{i \gamma_2 z} - H_- e^{-i \gamma_2 z} \right] \cdot \exp[i(\omega t - \beta' x)]$$

$$E_z = -\frac{\beta'}{\omega\epsilon_0 n_2^2} [H_+ e^{i\gamma_2 z} + H_- e^{-i\gamma_2 z}] \cdot \exp[i(\omega t - \beta' x)] \quad (6.31)$$

metal:

$$\begin{aligned} \vec{H} &= \hat{y} H_3 \exp[i(\omega t - \beta' x - \gamma_3 z)] \\ E_x &= -\frac{i\gamma_3}{\omega\epsilon_0 n_3^2} H_3 \exp[i(\omega t - \beta' x - \gamma_3 z)] \\ E_z &= -\frac{\beta'}{\omega\epsilon_0 n_3^2} H_3 \exp[i(\omega t - \beta' x - \gamma_3 z)] \end{aligned} \quad (6.32)$$

Since these fields must satisfy the homogeneous wave equation,

$$\gamma_1^2 = n_1^2 k^2 - \beta'^2 \quad (6.33a)$$

$$\gamma_2^2 = n_2^2 k^2 - \beta'^2 \quad (6.33b)$$

$$\gamma_3^2 = \beta'^2 - n_3^2 k^2 \quad (6.33c)$$

The magnitude of H_1 , H_+ , H_- , and H_3 are determined by a) the saltus condition at the air-film interface defined by ΔE_u and ΔH_u , and b) the normal boundary conditions requiring continuous tangential fields at the film-metal boundary. The solution fields could be evaluated in the x' - y' - z' coordinate system, but this would reveal discontinuities on the order of $(\delta_0 \beta)^2$ and $(\delta_0 \kappa)^2$, which are of second order and are neglected in this analysis. In order to cancel ΔH_u , the discontinuity in H_y at the n_1 - n_2 interface, we require

$$H_1 = H_+ \exp(-i\gamma_2 h) + H_- \exp(i\gamma_2 h) + \Delta H_u \quad (6.34)$$

and for the cancellation of the discontinuity ΔE_u ,

$$-\frac{\gamma_1}{n_1^2} H_1 = -\frac{\gamma_2}{n_2^2} [H_+ \exp(-i\gamma_2 h) - H_- \exp(i\gamma_2 h)] + \omega\epsilon_0 \Delta E_u \quad (6.35)$$

At the lower interface, these solution fields are subject to the uncorrugated-surface boundary conditions. (The effects of the corrugation at the lower interface will be calculated separately.) This allows H_1 to be solved:

$$H_{1,U} = \frac{C_1 \omega \epsilon_0 \left[\frac{n_2^2}{\gamma_2} \right] \Delta E_u + C_2 \Delta H_u}{C_2 - C_1 \left[\frac{\gamma_1 n_2^2}{\gamma_2 n_1^2} \right]} ,$$

where

$$C_1 = \exp(-i\gamma_2 h) - \exp(i\gamma_2 h) \cdot \frac{\left[1 + i \frac{\gamma_2 n_3^2}{\gamma_3 n_2^2} \right]}{\left[1 - i \frac{\gamma_2 n_3^2}{\gamma_3 n_2^2} \right]}$$

and

$$C_2 = \exp(-i\gamma_2 h) + \exp(i\gamma_2 h) \cdot \frac{\left[1 + i \frac{\gamma_2 n_3^2}{\gamma_3 n_2^2} \right]}{\left[1 - i \frac{\gamma_2 n_3^2}{\gamma_3 n_2^2} \right]} \quad (6.36)$$

and ΔE_u and ΔH_u are given by Eqs.(6.28).

The next step is to show how the amplitude of the solution fields leads to a coupling coefficient. The radiative solution fields carry energy away from the surface, with a power density defined by the normal component of the Poynting vector (\vec{S}). Since the solution fields were defined a priori to be the only mode to which the incident fields may couple, the power contained in this quantity ($\vec{S} \cdot \vec{n}$) must be drawn from the incident mode. Thus, emphasizing the restriction to radiative processes,

$$\Delta P_{gw} = -\vec{S} \cdot \vec{n} \Delta x .$$

From coupled-mode theory (Eq.(6.5)),

$$\frac{\partial P_{gw}}{\partial x} = -\frac{2}{L_{c,u}} P_{gw} ,$$

so that

$$\frac{1}{L_{c,u}} = \frac{\vec{S} \cdot \vec{n}}{2P_{gw}} . \quad (6.37)$$

The Poynting vector is given by

$$\begin{aligned} \vec{S} &= \frac{1}{4}[\vec{E} \times \vec{H}^* + \vec{E}^* \times \vec{H}] \\ &= -\hat{x}(E_z H_y^* + E_z^* H_y) + \hat{k}(E_x H_y^* + E_x^* H_y) . \end{aligned}$$

With

$$\vec{n} = -\hat{k},$$

$$\frac{1}{L_{c,u}} = -\frac{E_x H_y^* + E_x^* H_y}{2P_{gw}} .$$

Recalling that the value of C_{TM} was chosen so as to normalize the surface plasmon power to one watt per unit width in the y direction (Eq.(2.39)),

$$\frac{1}{L_{c,u}} = \frac{\gamma_1}{2n_1^2 k_0} \sqrt{\frac{\mu_0}{\epsilon_0}} H_1 H_1^* . \quad (6.38)$$

The coupling length of Eq.(6.38) represents the effect of the corrugation of the upper interface alone. The same technique is used for the corrugation of the film-metal interface, determining a scattered field amplitude which corresponds to a coupling length as in the derivation of Eq.(6.38). The coupling length due to both corrugations together is given by Eq.(6.38) with the field amplitude H_1 replaced by the sum of the amplitudes of the two scattered fields. The calculation for the film-metal corrugation is performed next, in abbreviated form.

Lower Corrugation

In the film, the fields are again given by Eqs. (2.33a) and (6.19), and in the metal, the fields are

$$H_y = C_{TM} A_3 [\exp[i(\omega t - \beta x) - \alpha_3 z]] . \quad (2.34a)$$

$$E_x = -\frac{i\alpha_3}{\omega\epsilon_0 n_3^3} C_{TM} A_3 [\exp[i(\omega t - \beta x) - \alpha_3 z]] .$$

$$E_z = -\frac{\beta}{\omega\epsilon_0 n_3^2} C_{TM} A_3 [\exp[i(\omega t - \beta x) - \alpha_3 z]] . \quad (6.39)$$

As before, the fields are evaluated in the local coordinate system of the corrugation via the transformation Eqs.(6.14) and with the corrugation now represented as

$$z = \delta_0 \cos(qx) . \quad (6.40)$$

The resulting fields are

$$\underline{\text{film:}} \quad E_{x',\text{film}} \Big|_{\ell} = \frac{C_{TM}}{\omega\epsilon_0 n_2^2} \exp[i(\omega t - \beta x)]$$

$$\times \left[A_- e^{-i\alpha_2 z} [\alpha_2 + \delta_0 \kappa \beta \sin(\kappa x)] - A_+ e^{i\alpha_2 z} [\alpha_2 - \delta_0 \kappa \beta \sin(\kappa x)] \right] \Big|_{z=\delta_0 \cos(\kappa x)}$$

$$H_{y',\text{film}} \Big|_{\ell} = C_{TM} \exp[i(\omega t - \beta x)] \left[A_+ e^{i\alpha_2 z} + A_- e^{-i\alpha_2 z} \right] \Big|_{z=\delta_0 \cos(\kappa x)}$$

$$\underline{\text{metal:}} \quad E_{x',\text{metal}} \Big|_{\ell} = -\frac{iC_{TM}}{\omega\epsilon_0 n_3^2} A_3 \exp[i(\omega t - \beta x)] [\alpha_3 + i\delta_0 \kappa \beta \sin(\kappa x)] e^{i\alpha_3 z} \Big|_{z=\delta_0 \cos(\kappa x)}$$

$$H_{y',\text{metal}} \Big|_{\ell} = C_{TM} \exp[i(\omega t - \beta x)] \left[A_+ e^{i\alpha_2 z} + A_- e^{-i\alpha_2 z} \right] \Big|_{z=\delta_0 \cos(\kappa x)} .$$

Following the same procedure as for the upper corrugation, the assumptions $\delta_0 \alpha_2 \ll 1$ and $\delta_0 \alpha_3 \ll 1$ allow a first-order expansion of the exponents evaluated at the corrugated interface, and terms in δ_0^2 are neglected. Then the sines and cosines are

absorbed into the propagator $\exp[i(\omega t - \beta x)]$ by the substitution $\beta' = \beta - \kappa$, and terms in $\exp(-i\kappa x)$ are dropped. The result is

film:

$$E_{x', \text{film}} \Big|_{\ell} = \frac{\alpha_2 C_{\text{TM}}}{\omega \epsilon_0 n_2^2} \exp[i(\omega t - \beta x)] [A_- - A_+] \\ + \frac{i \delta_0 C_{\text{TM}}}{2 \omega \epsilon_0 n_2^2} \exp[i(\omega t - \beta' x)] [A_+ + A_-] [\beta \beta' - n_2^2 k_0^2]$$

$$H_{y', \text{film}} \Big|_{\ell} = C_{\text{TM}} \exp[i(\omega t - \beta x)] [A_+ + A_-] \\ + \frac{i \alpha_2 \delta_0 C_{\text{TM}}}{2} \exp[i(\omega t - \beta' x)] [A_+ - A_-]$$

metal:

$$E_{x', \text{metal}} \Big|_{\ell} = -\frac{i \alpha_3 C_{\text{TM}}}{\omega \epsilon_0 n_3^2} A_3 \exp[i(\omega t - \beta x)] \\ + \frac{i \delta_0 C_{\text{TM}}}{2 \omega \epsilon_0 n_3^2} A_3 \exp[i(\omega t - \beta' x)] [\beta \beta' - n_3^2 k_0^2]$$

$$H_{y', \text{metal}} \Big|_{\ell} = A_3 C_{\text{TM}} \exp[i(\omega t - \beta x)] - \frac{\alpha_3 \delta_0 C_{\text{TM}}}{2} A_3 \exp[i(\omega t - \beta' x)] .$$

Again, the first term in each equation represents an unperturbed field which is continuous across the corrugated interface.

The discontinuities across the interface are

$$\Delta H_{y'} \Big|_{\ell} = H_{y', \text{metal}} \Big|_{\ell} - H_{y', \text{film}} \Big|_{\ell} = \Delta H_{\ell} \exp[i(\omega t - \beta' x)]$$

with

$$\Delta H_{\ell} = \frac{\alpha_3 \delta_0 C_{TM} A_3}{2} \left[\frac{n_2^2 - n_3^2}{n_3^2} \right]. \quad (6.41)$$

Similarly,

$$\Delta E_{x'} \Big|_{\ell} = E_{x',metal} \Big|_{\ell} - E_{x',film} \Big|_{\ell} = \Delta E_{\ell} \exp[i(\omega t - \beta' x)]$$

with

$$\Delta E_{\ell} = \frac{i \delta_0 \beta \beta' A_3 C_{TM}}{2 \omega \epsilon_0} \left[\frac{n_2^2 - n_3^2}{n_2^2 n_3^2} \right] \quad (6.42)$$

where

$$A_3 = \cos(\alpha_2 h) + \frac{\alpha_1 n_2^2}{\alpha_2 n_1^2} \sin(\alpha_2 h). \quad (2.37)$$

To determine the scattered field amplitudes, the same set of solution fields is postulated, and as before, the amplitude at the lower interface is set up to cancel the discontinuities ΔH_{ℓ} and ΔE_{ℓ} . At the upper interface, the fields are required to satisfy the flat surface boundary conditions to yield a first-order solution. The result is

$$H_{1,L} = \frac{A}{B} \quad (6.43a)$$

where

$$A = -i C_{TM} \frac{\delta_0 (n_2^2 - n_3^2) A_3}{2 n_3^2} \left[\frac{\beta \beta'}{n_2^2} + \frac{\alpha_3 \gamma_3}{n_3^2} \right] \quad (6.43b)$$

and

$$B = \frac{1}{2} \left[1 + \frac{\gamma_1 n_2^2}{\gamma_2 n_1^2} \right] \left[\frac{\gamma_2}{n_2^2} - i \frac{\gamma_3}{n_3^2} \right] - \frac{1}{2} \left[1 - \frac{\gamma_1 n_2^2}{\gamma_2 n_1^2} \right] \left[\frac{\gamma_2}{n_2^2} + i \frac{\gamma_3}{n_3^2} \right] \quad (6.43c)$$

Following the discussion preceding Eq.(6.38), the coupling length due to both interfaces is given by Eq.(6.38) with H_i replaced by the sum ($H_{1,U} + H_{1,L}$):

$$\frac{1}{L_c} = \frac{\gamma_1}{2n_1^2 k_0} \sqrt{\frac{\mu_0}{\epsilon_0}} (H_T H_T^*) \quad (6.44)$$

where
$$H_T = H_{1,U} + H_{1,L} . \quad (6.45)$$

Experimental Method

As discussed above, there are two separate sets of measurements which enable a determination of the parameters L_c and β_I . The first set is associated with the input coupler, where a dip in the reflected energy is observed as the incident beam is angle-tuned through the phase-match condition defined by Eq.(6.3). This is called the "coupling dip." The second set of measurements are made at the output coupler, where the decoupled beam is examined, yielding a second relationship between L_c and β_I .

In-coupling Measurements

The width of the coupling dip is determined by either the grating diameter, the divergence of the incident beam, or the surface plasmon attenuation; in this experiment the beam divergence was the limiting factor, resulting in an angular width of 1.26° (full width at the half-point of the dip). The angle at which the coupling is maximized will be denoted by θ_m , and is directly related to β_R by Eqs. (6.4) and (6.1). The existence of a dip indicates a transfer of energy from the incident beam to the surface plasmon. The remaining energy in the incident beam is reflected from the grating. Whereas the reflected beam is the only other channel for the incident beam, there are three energy-transfer processes that apply to the surface plasmon in the grating. The first is reradiation: as discussed in the theory section of this chapter, the coupling process is always accompanied by decoupling. Although

in practice this is a small amount of energy, it cannot be ignored and will be discussed below. The second process is the non-radiative absorption of the surface plasmon energy, which may be substantially greater in the presence of the grating than on a flat surface. The absorption also broadens the coupling dip, but in the present case the angular width of the beam is already so great that the effect is nearly unnoticeable.

At shorter wavelengths, the absorption term provides the only means of generating a coupling dip (Kretschmann and Raether, 1968) but in the far infrared there is fortunately a third channel for the surface plasmon, i.e. to escape the interaction region as a bound, surface-guided wave. This will be referred to as the transmitted portion, and the ultimate goal of the coupling process is to maximize the fraction of the incident beam which is transmitted as a surface-guided wave.

Thus the interaction of the incident beam with the grating results in four channels into which the radiation can be transferred: reflected, transmitted, absorbed, and reradiated. In practice it is possible to collect the reradiated beam along with the 0-order reflection. Although at θ_m the reradiated beam will be colinear with the 0-order beam, at other incident angles it is not. However, the reradiation is a second-order process with respect to in-coupling, and therefore it will in general be negligible except very near θ_m . If the collection optics have a field of view of even half the width of the coupling dip, they will adequately detect the reradiated beam. This argument only applies where the beam is placed near the end of the grating to favor the transmitted beam, for if the grating extends far beyond the incident beam, there may be a mismatch between the spatial profiles of the reradiated and the reflected beams. For the experiments discussed in this dissertation the reradiated

beam was completely collected by the detector monitoring the specular reflection, and unless specifically referred to, the reradiated beam is considered part of the 0-order reflection.

The detection of the reflected energy is complicated in the case of multiple reflected orders. The 0-order has been specifically referred to, but in general there will be other orders as well. If there are multiple orders, the energy in all the orders must be summed in order to measure the total reflected power. The period of the gratings used for this work was $154.2 \mu\text{m}$, for which $k_x^d = k_{\text{sp}}$ for the +1 diffracted order at an incident angle of -12.74° (measured from the normal) for the bare-metal surface plasmon. This configuration results in a total of two radiative diffracted orders (other than the surface plasmon), the 0-order (at $+12.74^\circ$) and the -1-order at -34.0° . Note that the angles quoted here apply to the case of a flat, bare metal surface, and change somewhat when an overlayer is applied.

At a fixed incident angle, it is a simple task to measure the power in the different radiative orders. Whereas the normal operation of the goniometer was to pivot the collection arm (lens and detector) in the normal $2\theta:\theta$ relationship with the angle of the incident beam (to follow the 0-order reflection from a grating), it was also possible to pivot the collection arm with the incident angle fixed. Furthermore, the collection arm could at any time be locked into the $2\theta:\theta$ mode, in precise alignment to the specular (0-order) reflection. The measurement procedure is as follows: With the collection arm locked to the 0-order reflection (the $2\theta:\theta$ mode), the incident beam was positioned on a grating and the incident angle adjusted until the minimum of the coupling dip was found. (The grating was previously aligned such that the grooves were parallel to the goniometer's rotation axis.) The horizontal

placement of the beam on the grating was also adjusted to minimize the 0-order reflection. Then the goniometer was locked in place, fixing the incident angle. The power in the 0-order was noted, and then the collection arm was swung around, independently, to measure the -1-order. This process was repeated at a different incident angle for which there was no coupling to the surface plasmon (usually about 5° greater than θ_m). At this second angle, the 0- and -1-orders sum to the incident intensity.

The presence of multiple reflected orders can also complicate the determination of the minimum in the coupling dip. In the vicinity of the coupling dip, the amount of energy in the 0-order is changing rapidly with incident angle. It cannot be assumed that the power in the -1-order will remain proportional to that of the 0-order, so the true minimum in the coupling dip cannot be determined until the power in the two orders (0 and -1) is summed at all angles near the coupling dip. This requires an angle scan of each order. Though the goniometer is designed to track the 0-order reflection as the incident angle was varied, the -1-order does not diffract from the grating with the same ($\theta_d = \theta_i$) angular dependence. Therefore it is inevitable that if the incident angle is scanned while the collection arm is fixed to the -1-order, the detector will become misaligned to the beam. Nevertheless it was possible to scan the -1-order, since over the 10° range of the scan, the field of view of the collection arm was sufficient to withstand the 1° - 2° misalignment that was incurred. (This is the same reason that allowed the reradiated beam to be included in the specularly reflected order).

The scans of the -1-order are typified by Figure 6.2, which shows the scans of the -1- and the 0-order for a grating on Sample 10. Consistently, the power in

the -1-order showed this dual-lobed behavior, crossing the "background" power level very close to the minimum of the dip in the 0-order. Similar results for the -1-order of a grating coupler can be found in the literature (Dakss, Kuhn, Heidrich and Scott, 1970). While the shape of this scan must cause the true θ_m to be different from the angular position of the minimum in the 0-order reflection, the amount of difference was in all cases smaller than the experimental error in the measurement of the position. More importantly, the measurement of the reflected power is negligibly affected by the shift.

To summarize, the total reflected power (P_{ref}) is measured by summing the power in the two radiative orders, at the angle of the minimum in the 0-order reflection, with the understanding that the reradiated term is included as a reflected beam. The coupling efficiency is given by the difference between the total reflected power at θ_m and the incident power, expressed as a percentage of the incident power. The dip in the reflected power can be predicted by the coupled-mode formalism, assuming knowledge of L_c , β_1 , the position of the beam on the grating, the grating length and periodicity, and of course the incident angle. However, this experiment alone does not provide enough information to uniquely specify L_c and β_1 . The needed information is provided in the following manner.

Out-coupling Measurements

Assuming that a surface plasmon has been generated in the experiment just discussed, we can gain the information needed to evaluate L_c and β_1 by experiments at the output coupler. The technique, described in the theory section of this chapter, results in a far simpler experimental and analytical procedure than that at the input coupler. The experiment to perform is to measure the rate of decay, as a function

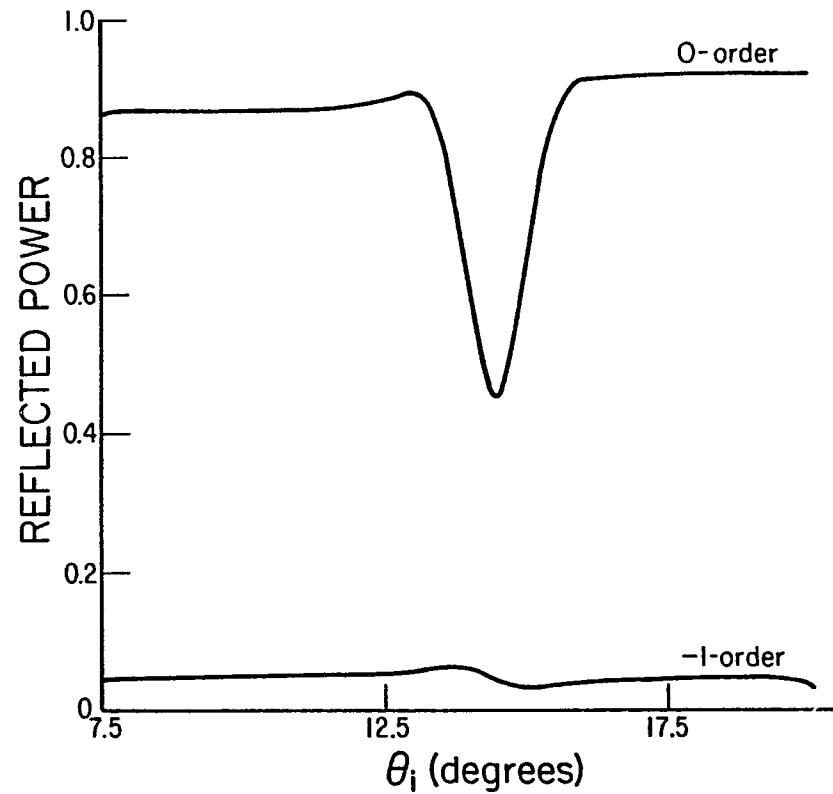


Figure 6.2. The 0-order and -1-order reflection from an input grating as a function of incident angle. The vertical axis is in arbitrary units. The scan range is from $\theta_i = 7.5^\circ$ to 20.0° . Note the shoulder in the 0-order at approximately 12° , caused by the +1-order passing off the grating. The drop in the -1-order at 20.0° is caused by the apparatus blocking the incident beam.

of position on the grating, of the power radiated from the output grating. It is not necessary to determine the absolute power level, only the rate of change. In practice the difficulty is to get both satisfactory signal-to-noise ratio and good spatial resolution. To perform this experiment, the collection arm of the system was modified. The sample was set up, as in all the experiments, to maximize the coupling efficiency at the input grating. (Actually a subtle difference between the minimum in the coupling dip and the maximum transmission resulted in a slightly different beam position, on the grating, than in the previous experiment.) No angular variation was needed, so the goniometer was fixed at θ_m . A "pinhole" aperture (2 mm x 2 mm) was the first element in the detector arm, positioned a few millimeters in front of the output grating. The size of the aperture is not critical; it can be shown that within a certain range it will not degrade the results. Care was taken to ensure that the aperture would not reflect the radiating beam back onto itself, as this would adversely affect the stability of the laser. The aperture was followed by a lens and then the detector, just as before. However in this case it was important that the detector see only that radiation which passed through the aperture. This was insured by imaging the aperture onto the detector, at a magnification that placed the edges of the mask around the aperture well beyond the detector's active area. Then the entire assembly was slowly scanned across the output grating, making sure that the distance between the aperture and the grating remained nearly constant. Figure 6.3 (top) is a diagram of the scan apparatus (a view from below the sample), with an example of the digitized results below it. The data was digitized as the natural logarithm of the output of the ratiometer. The log operation was performed to simplify the analysis; the expected exponential decay

would result in a straight line in the data file, which could then be directly analyzed using an appropriately weighted linear least-squares fit. The experimental error in the measurement of the exponential decay coefficient Γ was determined by repeating the experiment a number of times on several randomly chosen gratings; the resulting error was assumed to be applicable to all the measurements of Γ .

In order to completely determine the coupling parameters for each grating, each must be examined both as an input coupler and as an output coupler. Reversing the role of the input and output gratings merely required rotating the sample 180° around the normal to the surface. Although all ten gratings on each sample were very nearly identical, there was a significant variation in the film thickness over the face of each sample. Thus each grating ultimately was treated as if it had a separate film thickness. This is in contrast to the first experiment discussed in this dissertation, in which the measurements for a given sample were assigned the average film thickness for the entire sample.

The data from the two experiments were analyzed as follows: First the minimum in the coupling dip was measured by adding the energy in the 0-order at θ_m to that in the -1-order at the same angle. This sum was divided by the sum of the powers in each order at an angle well away from the coupling dip. The result is P_{ref} , the amount of power reflected from the grating at θ_m . The computer program based on the coupled-mode theory was designed to calculate the minimum P_{ref} based on inputs for L_c and β_1 . The inputs for L_c and β_1 were adjusted according to the formula Eq.(6.6) where Γ was determined from the measurements using the same grating as an output coupler. The correct combination of L_c and β_1 satisfied Eq.(6.6) and returned the measured value of P_{ref} . The errors in the measurements of L_c and

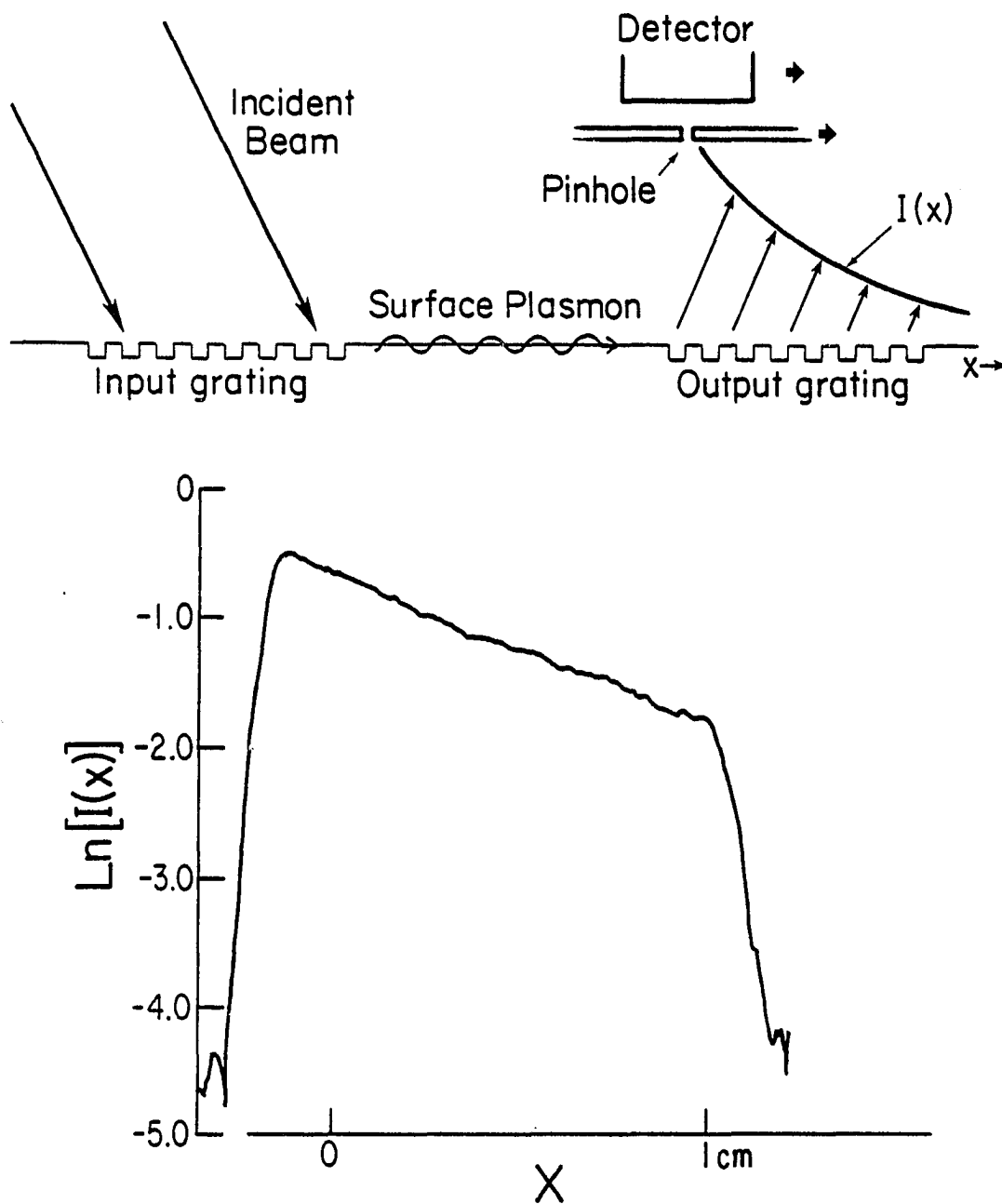


Figure 6.3. A diagram of the measurement of Γ at the output detector, with an example of digitized data at bottom. At top, the detector is scanned just above the output grating which is decoupling the surface plasmon. The result is an exponentially decaying signal. The data displayed below (from Sample 16) has been stored as a logarithm, showing the straight line that defines Γ .

β_I were determined by an error propagation analysis. (Assuming errors in L_c and β_I , error functions for P_{ref} and Γ were developed. The error functions were inverted to give the errors in L_c and β_I based on the measured errors in P_{ref} and Γ .)

Results

The experiments were performed with coating thicknesses ranging from $.1.8 \mu\text{m}$ to $5.1 \mu\text{m}$. The thicknesses were determined by averaging four measurements made on the corners of each grating. The two primary results are contained in Figures 6.4 and 6.5, which show the measured parameters L_c and β_I as a function of the overcoat thickness, accompanied by theoretical curves based on the preceding theory. Note that the coupling length data is expressed as L_c^{-1} , with the same units as the absorption term β_I . The theoretical curve in Figure 6.5 is the same as that in Fig. 5.2, except that it is displayed as an amplitude coefficient (since $\alpha=2\beta_I$), for direct comparison with the data. The single error bar in each figure is applicable to all data points in the figure.

From the measurement of L_c and β_I , the transmission of the grating coupler can be determined. Figure 6.6 shows the percentage of the incident beam power which is transmitted by the grating as a surface plasmon, plotted of course against the overcoat thickness. Primarily this shows that efficient generation of the surface plasmon has been achieved. No theoretical calculation of the transmission was included because it is not a fundamental property of the grating, i.e. it is a function of L_c , β_I , and the incident beam properties.

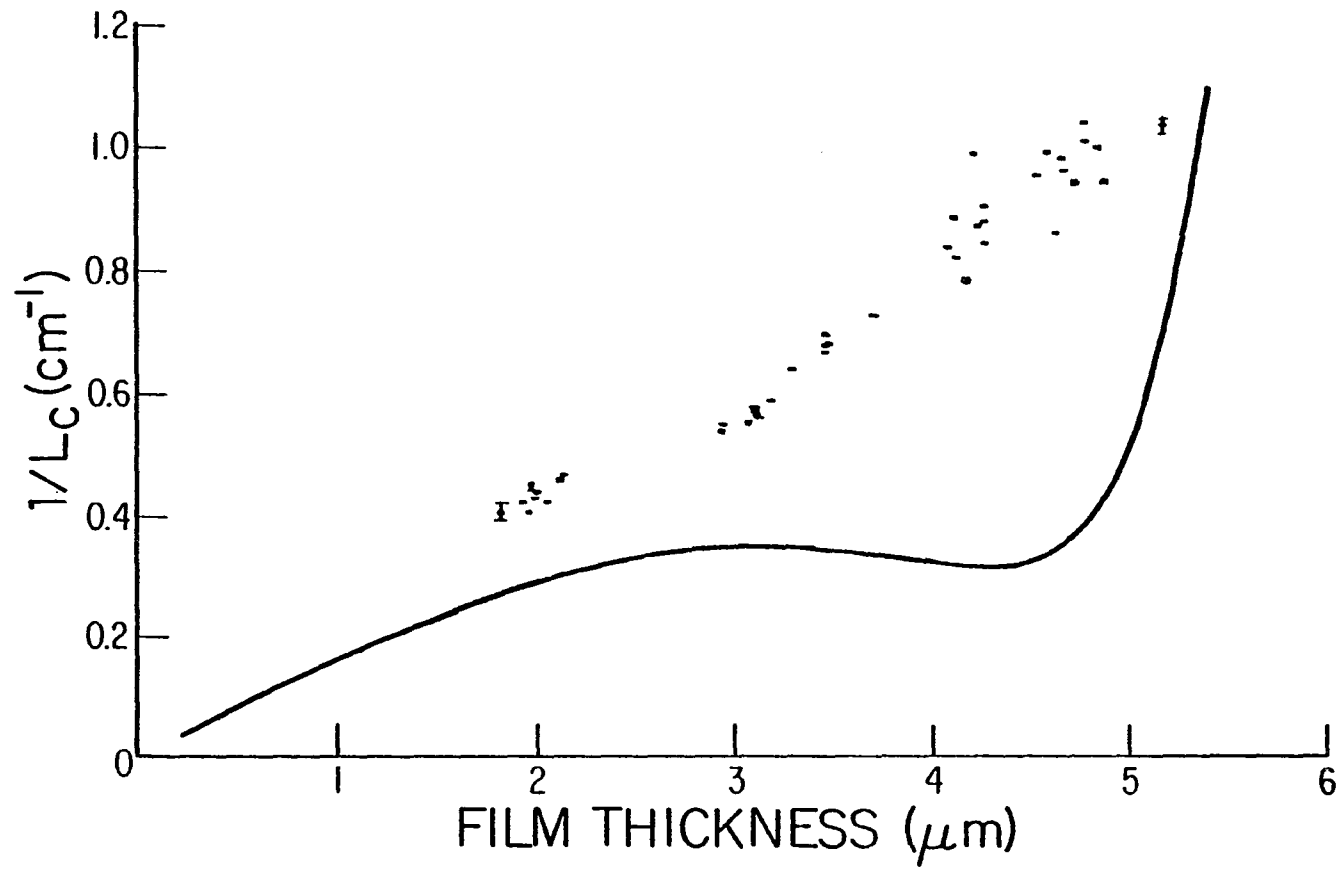


Figure 6.4. Data and theory (solid line) for measurements of L_c^{-1} versus overlayer thickness. The theoretical curve is a Total Fields calculation with an identical corrugation present at both film interfaces.

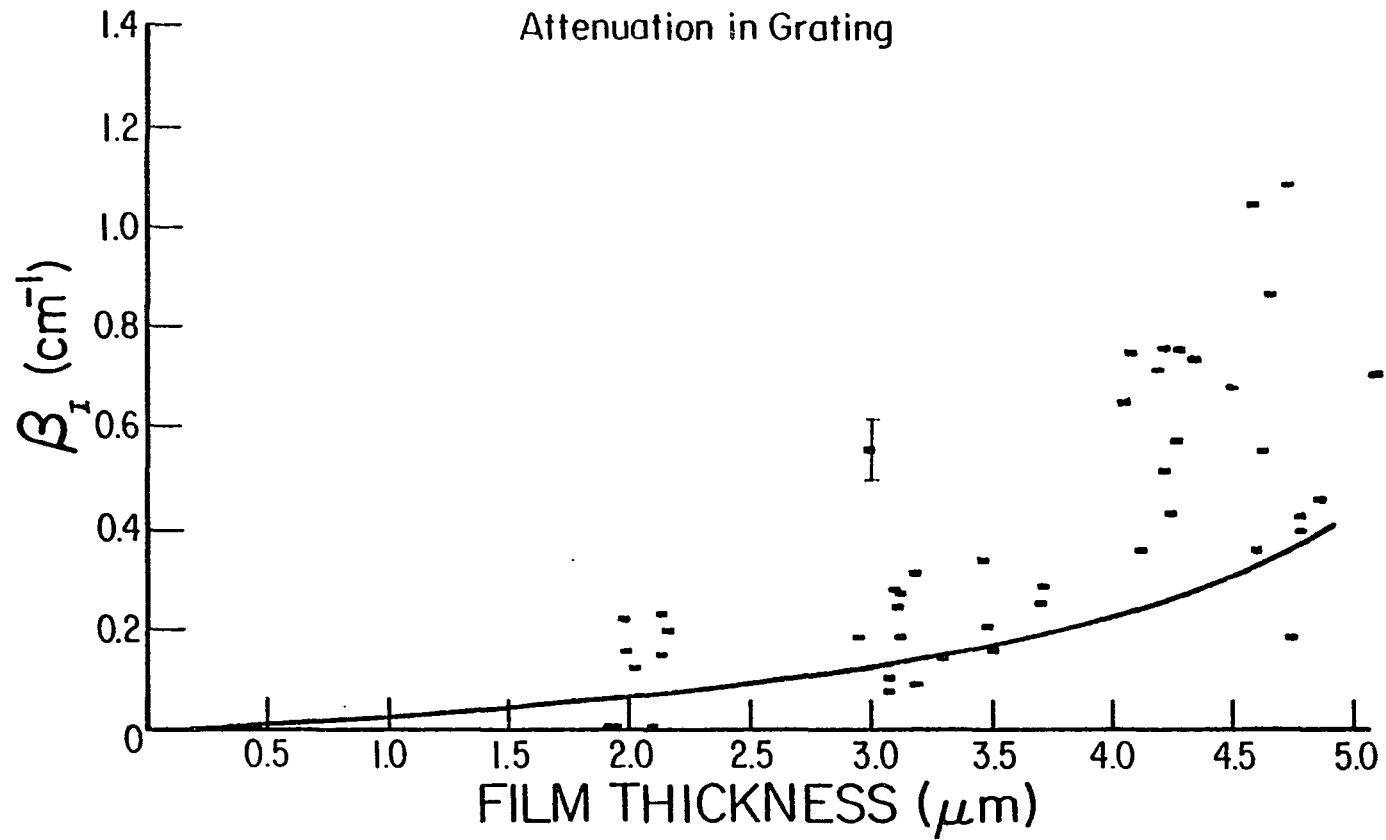


Figure 6.5. Amplitude absorption (β_I) of the overcoated surface plasmon mode in the grating region. The theory (solid line) is based on Eqs.(2.32-2.34), the overcoated mode equations. Despite the scatter in the data, the mean values indicate that the absorption is substantially higher in the grating region than in the uncorrugated region of the waveguide.

Discussion

Though the data in Figure 6.5 (β_1 vs. t) has a large scatter, the mean value of the data follows a curve that is qualitatively similar to the measurement of α in the flat-surface region. However, the attenuation in the grating region appears to be 1.5-2 times larger than in the flat-surface region. A higher absorption coefficient may be expected in the grating region due to the field enhancement at the corners and in the grooves of the grating. Nevertheless, this is an indication that there has been some change in the fundamental fields due to the presence of the corrugations, an effect first noticed in the previous coupling study (Seymour, Krupczak Jr. and Stegeman, 1984).

The most important measurement to be discussed is the coupling coefficient L_c^{-1} . Note that the range of coupling coefficients attained include the values considered optimal for the beam width (based on Figure 6.1). The transmission efficiency (Figure 6.6), however does not approach the theoretical maximum because of the presence of absorption (and to a lesser extent because the incident beam is not one-dimensional and it does not have a gaussian profile). Though the large absorption may be reduced (to increase the transmission) with a smaller grating amplitude, that would necessitate a thicker overlayer to recover the coupling length, which would counter the reduction in absorption. Therefore it appears that with these component materials and a 1 cm beam, the optimal coupling will occur with a grating depth of approximately 6 μm .

An extrapolation to zero film thickness in Figure 6.4 shows that in the absence of an overlayer the coupling lengths would be in the range of 3-5 cm. This would yield a coupling efficiency in the range 10-15%, a figure which is supported

by the depth of the coupling dip observed on the uncoated sample. Nevertheless, the coupling efficiency was still strongly enhanced by the overlayer, as evident in the increasing values of L_c^{-1} in Figure 6.4. (The transmission did not rise proportionally because of increasing attenuation.) The theoretical curve (solid line) in Figure 6.4 is the result of the total fields analysis, with both interfaces corrugated, and the agreement is poor; the coupling coefficients predicted are far smaller than those measured, consistent with the previous results on this subject (Seymour, Krupczak Jr. and Stegeman, 1984). Moreover, the shape of the theoretical curve is very different from the curve outlined by the data. (These calculations were made with the Drude parameter values measured by Johnson and Christy. Unlike the attenuation measurements of Chapter 5, the coupling lengths predicted by the total fields calculation are very weakly dependent on ω_p and τ .)

There are a number of possible explanations for the discrepancy between the theory and the data. At the outset of the grating theory section, it was noted that one of the key approximations of the first-order theory is violated at the metal-film interface, and this is a prime candidate for the failure of the first-order calculation. Another consideration is the effect of the trapezoidal grating profile; the perturbative grating theory has no capability of handling the shape factor. A third possibility will be considered first, that if β is close enough to the light line, the grating itself may induce changes in the modal fields.

The first-order grating theory assumes that the surface plasmon fields are the same in the presence of the grating as without. It was shown in Chapter 2 that both the penetration depth of the bare-metal surface plasmon field into the upper medium and the surface field magnitude are extremely sensitive to increases in β . Therefore

it seems plausible that for very thin overlayers or no overlayer, the first-order theory may be invalidated even by weak grating-induced perturbations of β_R . Once three or four microns of silicon has been deposited onto the metal, though, the mode has a β_R which is roughly 2% greater than k_0 . Perhaps this change in β_R would be sufficiently large that a grating-induced perturbation would not further affect the fields. Whether it is or not, if this effect caused the failure of the first-order theory, we should find that the agreement becomes better with increasing film thickness. However, Figure 6.4 shows that between 3 μm and 5 μm , in fact the agreement is getting worse (though it might be improving above 5 μm).

(Note that there is a steep rise in L_c^{-1} near a coating thickness of 6 μm , where the grating depth is approximately equal to the coating thickness. An extension of the theoretical curve beyond 5.5 μm would show that the coupling length rapidly approaches zero. Theoretical calculations performed with deeper and shallower gratings (12 and 3 μm) also exhibited the rapid rise in L_c^{-1} at 5-6 μm , demonstrating that it is coincidental that the coupling length rapidly approaches zero where the coating thickness equals the grating depth.)

To help examine the first possibility for the failure of the grating theory, in Figure 6.7 the contributions to the coupling length due to the corrugations at the upper and lower interfaces have been plotted separately from the results for both. (The substantial difference between the results for either single corrugation and those for both corrugations is attributable to destructive interference between the polarization fields of the two corrugations.) Although the wavelength is much greater than the depth of the gratings (the usual condition for applying a first-order grating theory), the corrugation is huge compared to the penetration depth of the

fields into the metal (approximately 500 \AA) This is a gross violation of the assumption that $\delta_0 \alpha_3 \ll 1$ (in fact, $\delta_0 \alpha_3 \cong 100$). The perturbative theory predicts discontinuities in the surface plasmon fields along the corrugated interface, which arise because the corrugation extends the position of the interface to a region of the z-axis, rather than the single value of z that represents a flat interface. The local-mode approach (Marcuse, 1974) used in the total fields analysis assumes that the surface plasmon fields in a given medium remain valid, but the extent of the medium (in the z-direction) changes with position along the grating (in the x-direction). In the present application, however, it is unreasonable to assume that the fields in the metal, which terminate in 500 \AA in the region $z > 0$, will extend upwards for $3 \mu\text{m}$ for half the cycle of the grating. The effect of the actual behavior the fields inside the metal is not obvious, but it may be that it would enhance the effect of the corrugation at the metal-film interface. Unfortunately, in Figure 6.7 the data does not appear to better fit the result for the lower corrugation than for the combination of both interfaces. However, the coherent sum of terms in the calculation for two equally corrugated interfaces may be in error because of an incorrect prediction of the magnitude of the lower-interface term. Nevertheless, considering the severity of the violation discussed above, the agreement of the theory with the experimental results is surprisingly good.

The last possibility for the failure of the first-order theory involves the shape factor. In the previous coupling study (Seymour, Krupczak Jr. and Stegeman, 1984), on bare gratings, the trapezoidal grating shape was discovered to provide at least fives times more efficient coupling than was obtained with a quasi-sinusoidal shape of the same amplitude. Since the first-order grating theory assumes a sinusoidal

corrugation, the discrepancy in Figure 6.4 may represent no more than the higher coupling efficiency that a trapezoidal shape provides. At this point it is premature to generalize from observations made on bare gratings; it has just been argued that bare-grating effects may diminish with overlayer thickness. However, the results of the following experiment will help to narrow the possibilities.

Measurement of β_R in Gratings

The comparison of the coupling measurements with theory may be further illuminated by a measurement of the parameter β_R in the grating region. This information is obtained by a careful measurement of the coupling angle θ_m . As in the case of β_I in the previous chapter, we can use β_R to imply properties of the surface plasmon. Once again, the presence of the grating introduces a new parameter which cannot necessarily be theoretically accounted for. The primary result, then, is to use the measurements of θ_m to compare with the coupling angles predicted by the field equations (2.32-2.34). Deviation from the predicted angles may provide some insight into the results of the coupling study.

Experimental Method

The difficulty in determining any absolute angle with a goniometer is to first accurately determine a reference. With a beam that has a 1.26° angular diameter, it is almost impossible to measure the zero-point with better than $1\text{-}2^\circ$ accuracy. (The HeNe beam was not aligned with the FIR beam well enough to use it to make a more accurate determination.) However, the symmetry of the grating equation (6.1) can be exploited to provide an accurate measurement, in the following manner (Y.J. Chen, private communication): The coupling will occur at precisely the same angle

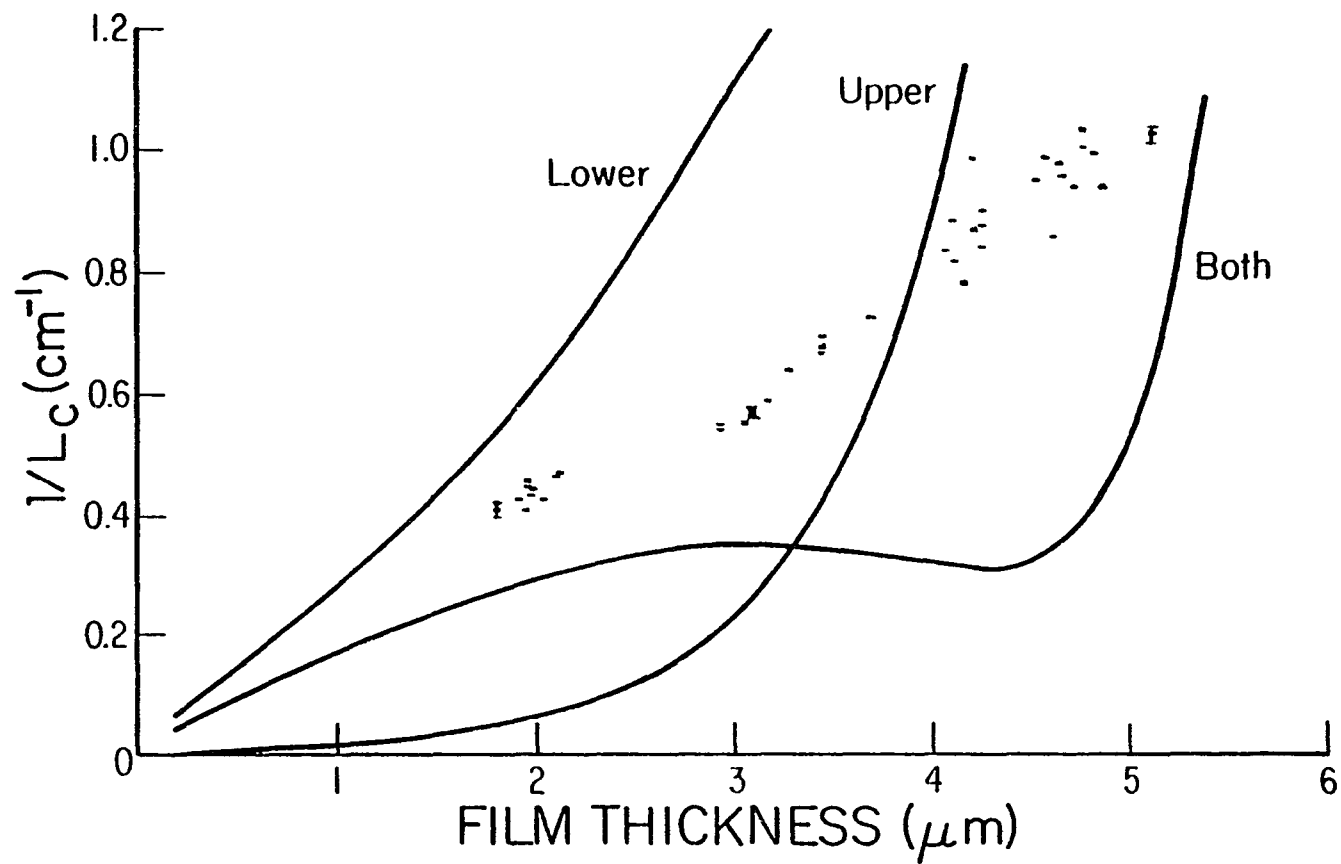


Figure 6.7. A repeat of Figure 6.5, with the addition of two theoretical curves. The contributions to the coupling length due to the corrugation at the upper (film-air) interface and the corrugation at the lower (film-metal) interface have been plotted separately. The original theoretical curve (labeled "both") signifies weaker coupling in some areas because of a destructive interference effect.

on each side of the normal to the sample surface. If scanned through a sufficiently large angle about the normal, both dips can be observed and the positions can be measured. The difference between the two angles, divided by two, is θ_m . The accuracy of this measurement is limited only by the error in the measurement of the minimum of each dip. In this case, the position of the minimum was measurable to an uncertainty no larger than 0.15° . The only change in the methods of the previous section was that the incident beam was placed in the center of the grating, to make the geometry as symmetrical as possible. As in the last section, the -1-order was not taken into account in the determination of θ_m , so the measurement relies solely on the dip in the 0-order.

Results

The data from 32 gratings is graphed in Figure 6.8, in the form of β_R versus film thickness. The small spread in the data points reflects the high accuracy of the method. Accompanying the measured points is the theoretical curve, which was determined by the overcoated surface plasmon dispersion equations (Eqs. (2.32-2.34)). Note that the measurements on a bare grating ($t=0$) fall below the theory curve. This represents the failure of the measurement technique on a bare metal surface. (Since β is unperturbed in this case, the coupling dip is accompanied by the disappearance of the +1 radiative order. The rapidly changing power in the +1-order as it passes off the grating, if not accounted for, shifts the minimum in the 0-order to smaller values of θ . Unfortunately, near this angle, the +1-order is widely scattered and cannot be collected. This is a manifestation of the "surface skimming mode" that was discussed in Chapter 1.)

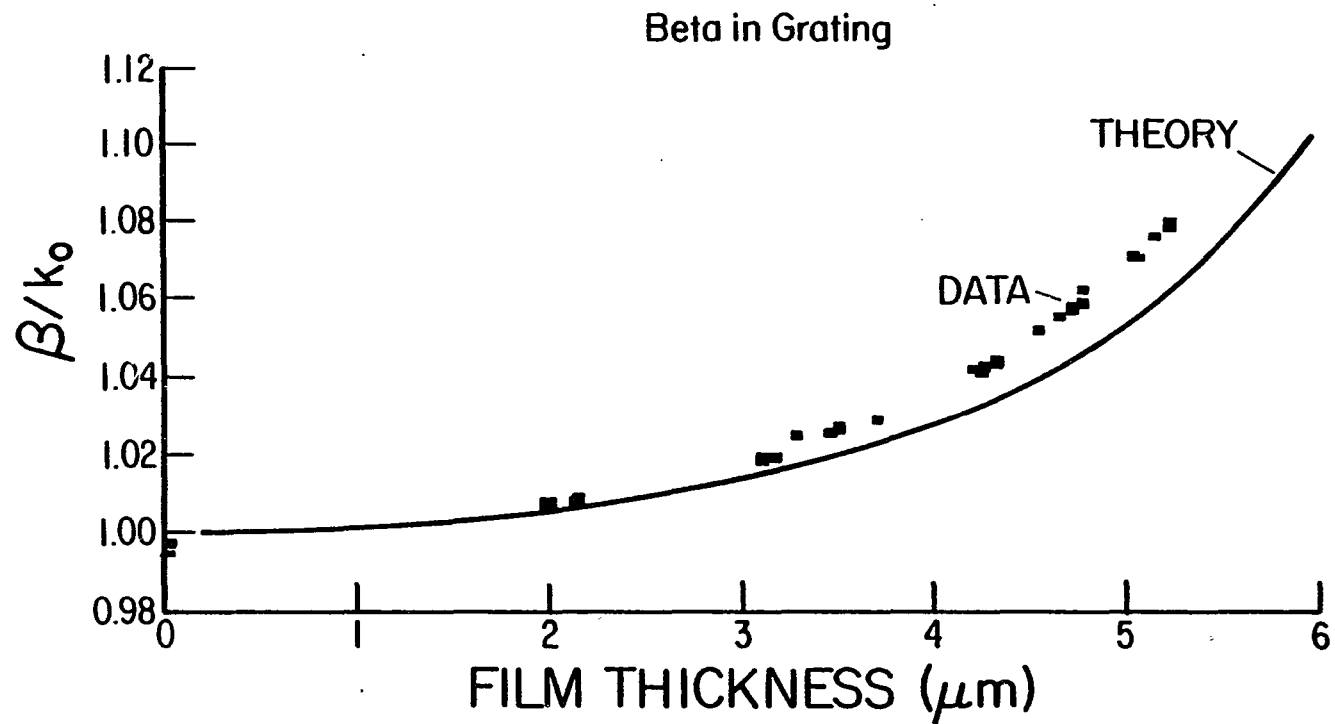


Figure 6.8. Results of measurements of β_R , versus overlayer thickness. The theoretical curve is based on Eqs.(2.32-2.34), the overcoated mode equations. The data indicates that the surface plasmon has a β that is perturbed to higher values by the corrugation. Data falling below the theoretical curve at $t=0$ represent the failure of the measurement technique for a bare metal surface.

Discussion

The theoretical curve, which falls significantly below the data points, has as its adjustable parameters the grating periodicity, the metal dielectric constant and the film dielectric constant. Though the dielectric constant of the metal was the dominant parameter in the measurement of β_I , in this case the metal parameters negligibly affect the curve of β_R versus t . The only parameter which strongly affects β_R is the real part of the index of refraction of the silicon overcoating. The results of fitting this parameter to the data is shown in Figure 6.9, for which it was necessary to raise the index of refraction from 3.42 to 4.00. This is unsatisfactory, since not only is that an unreasonable value for the index of silicon at $118.8 \mu\text{m}$, but the curve that results has lost the general shape of the data.

A constant difference $\Delta\beta$ between the theory and the data would be characteristic of a discrepancy between the actual grating periodicity and the κ used to make the calculation, which could be explained by a sample alignment error. However, the difference is not constant, and in fact increases with overlayer thickness. The curve traced by the data appears to have the same qualitative shape as the theoretical curve, but with a stronger curvature. It was found that adjusting the available parameters could not reproduce the data, leading to the conclusion that the observed behavior is outside of the scope of the theory upon which the curve is based. This appears to unveil a dichotomy between the results of Chapter 5 and these results. In Chapter 5, the three-layer dispersion relation was found to accurately predict β_I in the form of the absorption coefficient, but the results of this experiment demonstrate that the same theory does not accurately predict the real part of β . In this experiment, though, the effect of the grating on the mode cannot be accurately included.

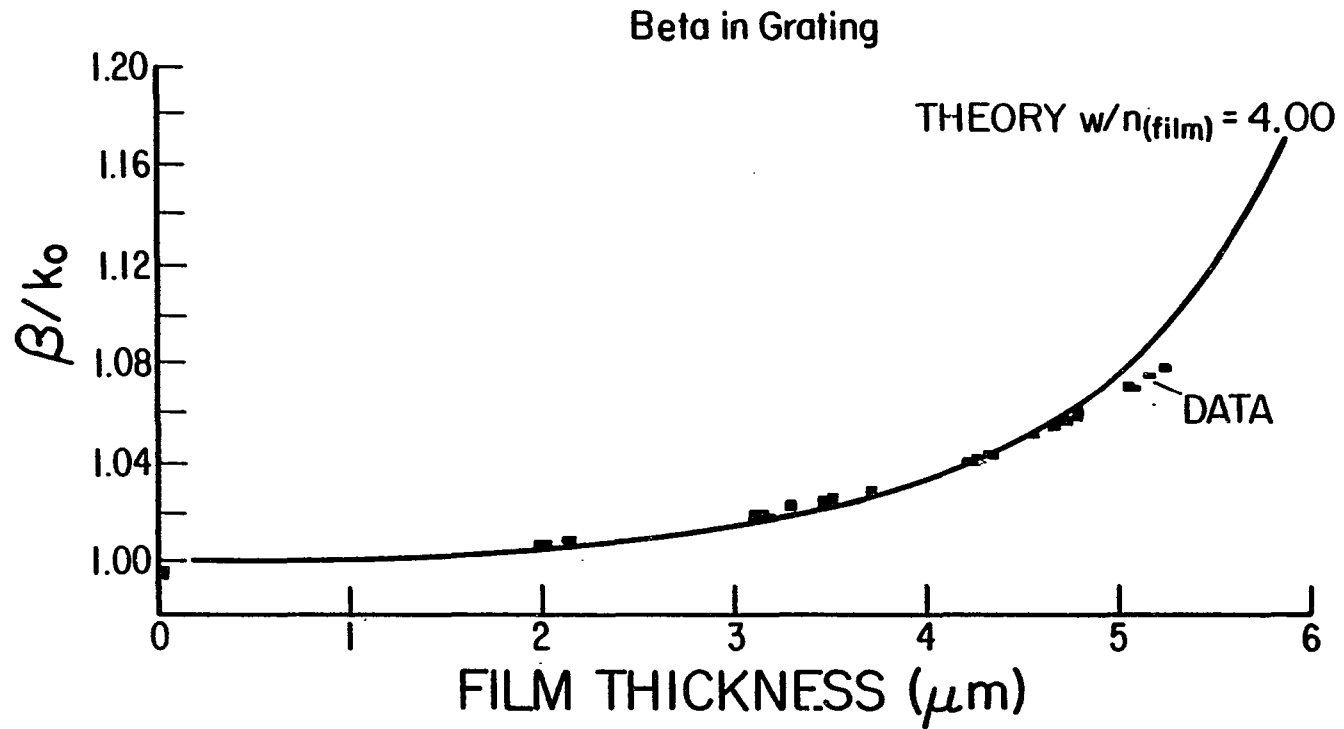


Figure 6.9. Results of fitting the measurements of β_R by varying the refractive index of the overlayer. This generates a theory curve which has lost the general shape of the data.

The conclusion is that the shape and/or depth of the grating corrugations is sufficient to alter the surface plasmon field distribution, again in agreement with previous the previous grating study on the overcoated mode (Seymour, Krupczak, Jr. and Stegeman, 1984). Thus the three-layer theory, which worked well for measurements pertaining to the flat region between the gratings, is insufficient for the prediction of β_R in the presence of the gratings.

The measurement of β_R vs. film thickness sheds light on the results of the measurement of L_c . The first argument (in the previous discussion section) used to explain the failure of the total fields calculation was aimed at small overlayer thicknesses, and it predicted that the agreement would improve with increasing thickness. However, Figure 6.8 shows that the deviation from the expected β_R progresses in precisely the opposite manner than the argument suggests: $\Delta\beta_R$ is largest for the thickest overlayers, and disappears as the thickness approaches zero. This is strong evidence that the perturbation due to the grating has not arisen because the overlayer is too thin; in fact the coating enhances the perturbation instead of eliminating it. This conclusion does not add evidence that the discrepancy in the prediction of coupling lengths is due to the approximation $\delta_0\alpha_3 \ll 1$ (in the total fields analysis). However, it does show that the grating causes a violation of another assumption of the first-order grating theory, that the incident fields inside the grating are described by the normal mode fields with no grating present. These measurements of β_R show definitively that the grating fields have a wavevector which is significantly shifted from the flat-surface fields.

In the previous section we saw that the measurements of the attenuation in the grating were also higher than the flat-surface theory predicts. This is consistent

with a greater-than-expected perturbation in β_R , as observed in this experiment. We can attempt a correction to the flat-surface theory, to see if β_R and β_I are correctly related to each other by the flat-surface theory, in the following manner: At a given overlayer thickness, we compare the value of the measured attenuation (β_I) to the value that is associated (by the flat-surface field equations) with the value of β_R that was measured at that overlayer thickness. In effect this bypasses the thickness of the film and directly correlates β_R with β_I . Unfortunately on comparison of the sets of results, the measured attenuation in the grating region is still higher than what would be expected for the β that was measured. However, it is legitimate to attribute at least part of the increased absorption to the additionally perturbed β_R , since the two parameters are fundamentally linked.

The same sort of first-order re-analysis can be applied to the measurements of L_c . In this case we associate a measured β_R with the thickness at which it would occur according to the flat-surface theory, and then examine the coupling length that the theory predicts at that film thickness. The physical rationale for this is that the degree of perturbation determines the field strength at the interfaces, which in turn factors into L_c^{-1} by way of the size of the discontinuities. If the first-order grating theory failed only because β_R was larger than expected, this re-analysis should yield good agreement. The result is to effectively shift the theoretical curve towards $t=0$, by an amount of approximately $1/2 \mu\text{m}$, which does not substantially improve the fit.

The results of this section suggest that the grating-induced perturbation of β is nonexistent in the absence of an overlayer. However, in previous studies on bare gratings, the trapezoidal grating shape was discovered to provide at least five times more efficient coupling than was obtained with a quasi-sinusoidal shape of the same

amplitude (Seymour, Krupczak Jr. and Stegeman, 1984). Combining these results, it must be concluded that the improved efficiency provided by the trapezoidal shape (compared to a sinusoidal shape) will itself be enhanced by an overlayer. Since the first-order grating theory assumes a sinusoidal corrugation, the data in Figure 6.4 support this interpretation. This suggests that perhaps the largest contributor to the failure of the first-order grating theory is the description of the corrugation as a sinusoid.

To conclude, the measurement of β_R versus t in the gratings clearly shows that the normal mode fields are altered by the surface corrugation, in violation of a basic assumption of the perturbative theory. The results indicate that the expected grating-induced perturbation of β_R appears roughly proportional to the perturbation due to the overlayer. If the grating-induced perturbation of β_R implies modal field changes that are similar to those caused by the overlayer (which perturbs β_R similarly), then the results of the measurements of L_c^{-1} , β_I and β_R are all consistent. The development of a theory to explain the numbers generated experimentally for these parameters will be left to future work. However, in generating those data I have demonstrated that high-efficiency coupling to far-infrared surface plasmons can be achieved, and have measured the fundamental coupling constants which characterize the process.

CHAPTER 7

CONCLUSION

The experiments performed in this dissertation have provided quantitative measurements on fundamental parameters of the overcoated surface plasmon mode in the far infrared. We have examined both the coupling and propagation of the mode, in the range of coating thickness that provides the optimum waveguide characteristics. The field equations of the overcoated mode were found to accurately describe the propagation length of the mode for the overlayer thicknesses investigated, even though the dielectric constant of the metal was predicted using the Drude model with parameters that were determined in the visible and ir spectral regions. The overcoated mode has been shown to have a wavevector that is sufficiently perturbed from the light line to decouple it from unbound modes, without overly penalizing the propagation length. In addition, efficient coupling has been demonstrated, with throughputs as high as 20% on a guide length of 3 centimeters. We conclude that the entire system fits the criteria of a far-infrared waveguide.

The study of the coupling properties using a grating coupler succeeded in demonstrating coupler transmission in excess of 40%. The coupling coefficients, however, were higher than those predicted by a first-order grating theory. The surface plasmon wavevector β was shown to be perturbed, beyond the effect of the overlayer, by the corrugation associated with the grating region. This additional perturbation represents a deviation from first-order behavior, in which the surface

plasmon mode is assumed to be unaffected by the corrugation. In the sense that any change in β can be expected to affect the coupling efficiency, the observed grating-induced perturbation is expected to result in, but does not fully explain, the enhanced coupling efficiencies. However, in light of the severe violation of an important approximation in the grating theory (i.e. $\delta_0\alpha_3 \ll 1$), it is surprising that the agreement is as good as it is.

The exact nature of the grating's influence on the surface plasmon fields is left to future research. The measurements of the grating-induced perturbation predict that the effect is extremely weak in the absence of the overlayer, but is enhanced by the presence of the overlayer. Relevant parameters requiring additional study include the depth and the shape of the gratings; these dependences were intentionally eliminated in these experiments. The inclusion of a result of a previous coupling study (Seymour et.al., 1984) points to the shape factor as being particularly important to the coupling data, and most likely, the grating-induced perturbation as well.

The investigation of the mode has successfully taken techniques and formalisms from the optical regime and re-employed them in the near-millimeter spectral region, a factor of one hundred lower in frequency. The attenuation measurements were well predicted using parameters determined in the infrared and optical spectrum. The exception to this success was the first-order grating theory. The overall failure of that theory, well within the limit which is commonly cited for the use of perturbation theory ($\delta_0k \ll 1$), suggests that a corollary parameter in the application of perturbative theories to metal gratings is the ratio of the corrugation amplitude to the skin depth. Utilizing a first-order theory known as "total fields"

analysis (Normandin et al., 1979), the requirement that the corrugation amplitude be small compared to the field variation in all directions is explicit. Using other perturbative grating theories, this would not have been so readily apparent (Marcuse, 1974; Yariv, 1973). It is likely that this violation was a major factor in the poor theoretical prediction of the coupling lengths and the perturbation of the fundamental fields in the grating region.

An immediate application for the overcoated mode would be a more rigorous study of the dielectric properties of metals. The overcoated mode has a far greater ability to sample the metal than a bare-metal surface plasmon, because of the field enhancement. The propagation length is so large on a bare metal surface that it is effectively unmeasurable, so the "penalty" exacted by the overcoating is in this case an advantage. Moreover, performing experiments at longer wavelengths should present no additional difficulties since strong sources are available, and the general effects of the overcoating will be the same.

There is no question however that this spectral regime is seriously hampered by the scarcity of suitable dielectric materials, a fact that is the primary hindrance to the development of submillimeter communications technology. A rash of work in the search for suitable far-infrared materials took place in the 1970's (see Simonis, 1982 for an excellent index), the results of which were unpromising. The situation remains largely the same now as it did then. With regard to the overcoated surface plasmon mode, there still remains further experimental work which must be performed before questions of its technological utility can be answered. However, in the spectral regime of the far infrared and near-millimeter waves where few low-loss dielectrics exist, the overcoated mode must be considered a leading technique for the guided propagation of electromagnetic energy.

Future Work

There are two general areas to be investigated in future experiments. First, the failure of the first-order grating theory must be addressed. The cause of that failure has been discussed, but experimental work that was performed was insufficient to pinpoint the cause. The second area of investigation involves experiments designed to explore the technological potential of the mode. Other geometries such as strip or channel waveguides must be fabricated which would be more compatible with the requirements of communications technology, and their characteristics must be measured.

An important improvement should be made in future sample preparation. In our experiments, the samples performed a dual role, being used for propagation measurements and for coupling measurements. This required compromises in the grating depth and the overlayer thicknesses which limited both of the experimental studies. It would be desirable to fabricate samples that are more specifically designed for a given type of experiment. For instance, by focusing on the coupling, a very wide range of coating thicknesses could be investigated. It is feasible to do this now that measurements have been made that can be used to predict the performance of new gratings and waveguides. In this dissertation, the overlayer thickness was limited by the propagation experiments, both on the low side and the high side. Another major experimental improvement would be shorten the grating periodicity so that the only radiative order would be the specular reflection. Not only would it greatly simplify the measurements, it would increase the coupling efficiency as well. The same grating fabrication technique could be used, as the period would still be large (slightly under $100\ \mu\text{m}$).

As for the nature of future coupling studies, from a practical point of view it is much easier to alter the samples than to apply a more rigorous grating theory. An important study to perform would be to vary the grating depth for a given film thickness to see at what point the perturbative theory becomes applicable. If possible, this should be performed with a smoother grating profile than the trapezoidal shape. A reasonable assumption is that the first-order theories will not be applicable as long as the grating is perturbing the fields as demonstrated by the measurement of β_r in Chapter 6. If the grating effects are shape dependent, it would be immediately apparent if a sinusoidal profile were used. The trapezoidal profile may cause grating effects over a wide range of grating depths.

Another approach to take would be to corrugate only one of the surfaces, eliminating the question of whether the failure of the theory is in the interaction of the two corrugations, or if it is limited to the effect of the lower corrugation. Perhaps the sample could be completely fabricated without etching the substrate, and then a grating could be created on the air-film interface. With the current fabrication technique, it is impossible to corrugate the metal-film boundary alone.

To further investigate the technological possibilities of this surface plasmon waveguide, a completely different set of experiments must be performed. This would involve the fabrication of strip and channel waveguides, to provide another degree of restriction to the propagation of the energy in the guide. It would be necessary to determine the losses incurred at in-plane and out-of-plane bends of a strip or channel guide, to predict the performance of an actual devices. These measurements could perhaps lead the way to more sophisticated elements such as refractive elements or mirrors, etc.

In summary, the mode can now be considered as a well-behaved waveguide mode, for which only the first round of investigations have been performed. The demonstrated effectiveness of optical and near-infrared techniques, along with the history of optical guided-wave research, is a clear indicator of the types of experiments that are appropriate for this mode in the future.

REFERENCES

- Begley, D.L., Alexander, R.W., Ward, C.A., Miller, R., Bell, R.J., "Propagation distances of surface electromagnetic waves in the far infrared," *Surface Science* 81, 245 (1979).
- Bell, R.J., Alexander Jr., R.J., Ward, C.A., Tyler, I.L., "Introductory theory for surface electromagnetic wave spectroscopy," *Surface Science* 48, 253 (1975).
- Bhasin, K., Bryan, D., Alexander, R.W., Bell, R.J., "Absorption in the infrared of surface electromagnetic waves by adsorbed molecules on a copper surface," *J. Chem. Phys.* 64, 5019 (1976).
- Bryan, D.A., Begley, D.L., Bhasin, K., Alexander, R.W., Bell, R.J., Gerson, R., "Propagation distance of surface electromagnetic waves on two metal-oxide-air systems," *Surface Science* 57, 53 (1976).
- Butler, K.J., ed., Infrared and Millimeter Waves, (Academic Press, New York, 1983).
- Chabal, Y.J., Sievers, A.J., "Surface electromagnetic wave launching at the edge of a metal film," *Appl. Phys. Lett.* 32, 90 (1978).
- Chantry, G.W., Fleming, J.W., Smith, P.M., Cudby, M., Willis, H.A., "Far infrared and millimeter wave absorption spectra of some low loss polymers," *Chem. Phys Lett.* 10, 473 (1971).
- Dakss, M.L., Kuhn, L., Heidrich, P.F., Scott, B.A., "Grating coupler for efficient excitation of optical guided waves in thin films," *Appl. Phys. Lett.* 16, 523 (1970).
- Drude, P., "Zur Elektronentheorie der Metalle," *Annalen der Physik* 1, 566 (1900); 3, 369 (1900).
- Foote, F.B., Hodges, D.T., Dyson, H.B., "Calibration of power and energy meters for the far infrared/near millimeter wave spectral region," *Int. J. Inf. Millim. Waves* 2, 773 (1981).
- Johnston, D.R., Burch, D.E., "Attenuation by Artificial Fogs in the Visible, Near Infrared and Far Infrared," *Appl. Opt.* 6, 1497 (1967).
- Johnson, P.B., Christy, R.W., "Optical Constants of the Noble Metals," *Physical Review* B6, 4370 (1972).
- Kapany, N.S., Burke, J.J., Optical Waveguides, (Academic Press, New York, 1972).

- Kogelnik, H., in Integrated Optics, T. Tamir ed., (Springer-Verlag, New York, 1975).
- Koteles, E.S., McNeill, W.H., "Far Infrared Surface Plasmon Propagation," International Journal of Infrared and Millimeter Waves 2, 361 (1981).
- Kretschmann, E., "Die Bestimmung der oberflächenrauigkeit dünner schichten durch messung der winkelabhängigkeit der streustrahlung von oberflächenplasmaschwingungen," Optics Communications 10, 353 (1974).
- Kretschmann, E., Raether, H., "Radiative Decay of Non Radiative Surface Plasmons Excited by Light," Z. Naturforsch. 23a, 2135 (1968).
- Kuwamura, Y., Yokota, Y., Fukui, M., Tada, O., "ATR Mode of Surface Polaritons," J. Physical Society of Japan 51, 2962 (1982).
- Loewenstein, E.V., Smith, D.R., Morgan, R.L., "Optical Constants of Far Infrared Materials. 2: Crystalline Solids," Applied Optics 12, 398 (1973).
- Lorrain, P., Corson, D.R., Electromagnetic Fields and Waves, (W.H. Freeman and Company, San Francisco, 1970).
- Marcuse, D., Theory of Dielectric Optical Waveguides, (Academic Press, New York, 1974).
- McMullen, J.D., "Propagation Lengths of Surface Polaritons at 10.6 microns on BeO and Metal Substrates," Solid State Communications 17, 331 (1975).
- Normandin, R., So, V.C-Y., Rowell, N., Stegeman, G.I., "Scattering of guided optical beams by surface acoustic waves in thin films," J. Opt. Soc. Am. 69, 1153 (1979).
- Ordal, M.A., Bell, Robert J., Alexander Jr., R.W., Long, L.L., Query, M.R., "Optical properties of fourteen metals in the infrared and far infrared: Al, Co, Cu, Au, Fe, Pb, Mo, Ni, Pd, Pt, Ag, Ti, and W," Applied Optics 24, 4493 (1985).
- Ordal, M.A., Long, L.L., Bell, R.J., Bell, S.E., Bell, R.R., Alexander Jr., R.W., Ward, C.A., "Optical properties of the metals Al, Co, Cu, Au, Fe, Pb, Ni, Pd, Pt, Ag, Ti and W in the infrared and far infrared," Applied Optics 22, 1099 (1983).
- Otto, A., "Excitation of nonradiative surface plasma waves in silver by the method of frustrated total reflection," Zeitschrift für Physik 216, 398 (1968).
- Otto, A., Sohler, W., "Modification of the total reflection modes in a dielectric film by one metal boundary," Optics Communications 3, 254 (1971).

- Passchier, W.F., Honijk, D.D., Mandel, M., Afsar, M.N., "A new method for the determination of complex refractive index spectra of transparent solids in the far-infrared spectral region: Results of pure silicon and crystal quartz," *J. Phys D: Appl. Phys.* **10**, 509 (1977).
- Polky, J.N., Mitchell, G.L., "Metal-clad planar dielectric waveguide for integrated optics," *Journal of the Optical Society of America* **64**, 274 (1974).
- Ritchie, R.H., Hamm, R.N., Williams, M.W., Arakawa, E.T., "Dispersion Relation of Elementary Excitations when Damping Is Present," *Phys. Stat. Sol.(b)* **84**, 367 (1977).
- Schlesinger, Z., Sievers, A.J., "Infrared surface wave interferometry," *Appl. Phys. Lett.* **36**, 409 (1980).
- Schlesinger, Z., Webb, B.C., Sievers, A.J., "Attenuation and coupling of far infrared surface plasmons," *Sol. St. Comm.* **39**, 1035 (1981).
- Schoenwald, J., Burstein, E., Elson, J.M., "Propagation of surface polaritons over macroscopic distances at optical frequencies," *Sol. St. Comm.* **12**, 185 (1973).
- Seymour, R.J., Koteles, E.S., Stegeman, G.I., "Far-infrared surface plasmon coupling with overgrated gratings," *Appl. Phys. Lett.* **41**, 1013 (1982).
- Seymour, R.J., Krupczak Jr., J.J., Stegeman, G.I., "High efficiency coupling to the overcoated surface plasmon mode in the far infrared," *Appl. Phys. Lett.* **44**, 373 (1984).
- Seymour, R.J., Stegeman, G.I., "Use of Overcoated Surface Plasmon Components in the Far Infrared," *Proc. SPIE Int. Soc. Opt. Eng.* **408**, 191 (1983).
- Simonis, George J., "Index to the literature dealing with the near-millimeter wave properties of materials," *Int. J. of Infrared and Millimeter Waves* **3**, 439 (1982).
- Stegeman, G.I., Sarid, D., Burke, J.J., Hall, D.G., "Scattering of guided waves by surface periodic gratings for arbitrary angles of incidence: perturbation field theory and implications to normal-mode analysis," *J. Opt. Soc. Am.* **71**, 1497 (1981).
- Stegeman, G.I., Seymour, R.J., "Surface Plasmon Attenuation by Thin Film Overlayers in the Far Infrared," *Sol. St. Comm.* **44**, 1357 (1982).
- Ulrich, R., "Theory of the Prism-film Coupler by Plane-Wave Analysis," *J. Opt. Soc. Am.* **60**, 1337 (1970).
- Ulrich, R., "Efficiency of optical-grating couplers," *J. Opt. Soc. Am.* **63**, 1419 (1973).

- Ward, C.A., Bell, R.J., Alexander, R.W., Kovener, G.S., Tyler, I., "Surface Electromagnetic Waves on Metals and Polar Insulators: Some Comments," *Applied Optics* 13, 2378 (1974).
- Ward, C.A., Bhasin, K., Bell, R.J., Alexander, R.W., Tyler, I., "Multimedia dispersion relation for surface electromagnetic waves," *J. Chem. Phys.* 62, 1674 (1975).
- Yariv, A., "Coupled-mode theory for guided-wave optics," *IEEE J. Quantum Elect.* QE-9, 919 (1973).
- Yariv, A., Quantum Electronics, (John Wiley and Sons, New York, 1975).
- Zhizhin, G.N., Moskaleva, M.A., Shomina, E.V., Yakovlev, V.A., "Selective absorption of a surface electromagnetic wave propagating on a metal in the presence of a thin dielectric film," *JETP Lett.* 24, 196 (1976).